ÉCOLE DE TECHNOLOGIE SUPÉRIEURE
UNIVERSITÉ DU QUÉBEC

THESIS SUBMITTED TO
ÉCOLE DE TECHNOLOGIE SUPÉRIEURE

IN PARTIAL FULFILLMENT OF THE REQUIREMENTS FOR THE DEGREE OF
MASTER OF SCIENCE IN AUTOMATED PRODUCTION ENGINEERING
M. Eng.

BY
EMIL GABRIEL CRISAN

VALIDATION OF A MATHEMATICAL MODEL FOR BELL 427 HELICOPTER USING PARAMETER ESTIMATION TECHNIQUES AND FLIGHT TEST DATA

MONTREAL, 7th of APRIL, 2005

THIS THESIS IS EVALUATED

BY A JURY COMPOSED OF:

Mme Ruxandra Botez, director of thesis
Department of Automated Production Engineering at École de technologie supérieure

M. Njuki Mureithi, co-director
Department of Mechanical Engineering at École Polytechnique de Montréal

M. Eric Granger, president of jury
Department of Automated Production Engineering at École de technologie supérieure

M. Joey Seto, external jury member
Aerodynamics and Handling Qualities Group, Bell Helicopter Textron Canada

THIS THESIS WAS PRESENTED IN FRONT OF

JURY

ON 7th of APRIL, 2005

AT ÉCOLE DE TECHNOLOGIE SUPÉRIEURE

VALIDATION OF A MATHEMATICAL MODEL FOR THE BELL 427 HELICOPTER USING PARAMETER ESTIMATION TECHNIQUES AND FLIGHT TEST DATA

Emil Gabriel Crisan

ABSTRACT

Certification requirements, optimization and minimum project costs, design of flight control laws and the implementation of flight simulators are among the principal applications of system identification in the aeronautical industry. This document examines the practical application of parameter estimation techniques to the problem of estimating helicopter stability and control derivatives from flight test data provided by Bell Helicopter Textron Canada.

The purpose of this work is twofold: a time-domain application of the Output Error method using the Gauss-Newton algorithm and a frequency-domain identification method to obtain the aerodynamic and control derivatives of a helicopter. The adopted model for this study is a fully coupled, 6 degree of freedom (DoF) state space model. The technique used for rotorcraft identification in time-domain was the Maximum Likelihood Estimation method, embodied in a modified version of NASA's Maximum Likelihood Estimator program (MMLE3) obtained from the National Research Council (NRC). The frequency-domain system identification procedure is incorporated in a comprehensive package of user-oriented programs referred to as CIFER®.

The coupled, 6 DoF model does not include the high frequency main rotor modes (flapping, lead-lag, twisting), yet it is capable of modeling rotorcraft dynamics fairly accurately as resulted from the model verification. The identification results demonstrate that MMLE3 is a powerful and effective tool for extracting reliable helicopter models from flight test data. The results obtained in frequency-domain approach demonstrated that CIFER® could achieve good results even on limited data.

VALIDATION D'UN MODÈLE MATHÉMATIQUE PAR DES TECHNIQUES D'ESTIMATION DES PARAMÈTRES POUR L'HÉLICOPTÈRE BELL 427 À PARTIR DES ESSAIS EN VOL

Emil Gabriel Crisan

SOMMAIRE

Les demandes de certification, d'optimisation et des coûts minimaux des projets, le design des lois de commande de vol et l'implantation des simulateurs de vol se trouvent parmi les applications principales de l'indentification des systèmes dans l'industrie aéronautique. Ce mémoire analyse l'application pratique des techniques d'estimation de paramètres aux problèmes d'estimation des dérivées de stabilité et contrôle à partir des données d'essais en vol fournies par Bell Helicopter Textron Canada.

Ce travail consiste en deux parties : l'application dans le domaine du temps de la méthode d'erreur de la sortie en utilisant l'algorithme de Gauss – Newton et la méthode d'identification dans le domaine de la fréquence pour l'obtention des dérivées aérodynamiques et de contrôle des hélicoptères. Le modèle utilisé dans l'étude est le modèle sous forme d'espace d'état en six degrés de liberté. La technique utilisée pour l'identification des hélicoptères dans le domaine du temps est la méthode d'estimation de probabilité maximale des paramètres (Maximum Likelihood Estimation method) et elle est incluse dans la version modifiée du programme d'estimation des paramètres de la NASA (Modified Maximum Likelihood Estimator program, MMLE3) obtenu de la part de National Research Council (NRC). La procédure d'identification des systèmes dans le domaine de fréquence est incorporée dans l'ensemble des programmes orientés vers l'utilisateur et appelés CIFER®.

Le modèle en 6 degrés de liberté n'inclut pas les modes du rotor principal aux très hautes fréquences, mais la dynamique de l'hélicoptère est modélisée aussi précisément que celle calculée par la validation du modèle. Les résultats d'identification montrent que MMLE3 est un outil puissant et efficace pour l'extraction des modèles d'hélicoptères à partir des données d'essais en vol. Les résultats obtenus par l'approche dans le domaine de fréquence montrent que CIFER® peut donner des bons résultats même sur des données d'essais en vol limitées.

VALIDATION D'UN MODÈLE MATHÉMATIQUE PAR DES TECHNIQUES D'ESTIMATION DES PARAMÈTRES POUR L'HÉLICOPTÈRE BELL 427 À PARTIR DES ESSAIS EN VOL

RÉSUMÉ

Introduction

Ce mémoire analyse l'application pratique des techniques d'estimation de paramètres aux problèmes d'estimation des dérivées de stabilité et contrôle à partir des données d'essais en vol fournies par Bell Helicopter Textron Canada. Le travail est concentré sur le calcul des dérivées de stabilité et contrôle de l'hélicoptère Bell 427 en utilisant un modèle sous forme d'espace d'état en 6 degrés en liberté. Ce modèle utilise des équations linéaires et couplées.

L'efficience des méthodes d'estimation des paramètres a été testée en comparant les données réelles des essais en vol avec les réponses prédites de l'hélicoptère. Deux approches ont été utilisées pour résoudre le problème d'identification : a) une application dans le domaine du temps de la méthode de l'erreur de la sortie en utilisant l'algorithme de minimisation de Gauss – Newton et b) une méthode d'identification dans le domaine de la fréquence.

La sélection de l'entrée optimale

L'entrée de commande pour l'essai en vol a toujours un impact majeur sur la qualité des données recueillies pour la modélisation de la dynamique de l'hélicoptère. Pour le programme d'estimation des paramètres du modèle Bell 427, le mouvement de l'hélicoptère est perturbé à partir de sa position d'équilibre en appliquant une séquence d'impulsions des contrôles dans le domaine de temps. Ces impulsions ont des signes et

longueurs différentes, et sont des entrées de contrôle de la forme 2311, où les chiffres expriment le nombre de périodes de temps unitaire (1 seconde) entre les inversions des signes des différents contrôles appliqués par le pilote.

Les avantages des entrées de contrôle 2311 sont :

a. Le contenu en hautes fréquences suffisant;
b. La facilité d'exciter tous les modes de mouvement de l'avion;
c. Une courte durée, facilement exécutable et répétable;
d. Pas d'excitation des modes du rotor de haute fréquence, qui ne sont pas inclus dans le modèle en six degrés de liberté.

Pendant l'essai en vol, une seule entrée du contrôle à la fois a été utilisée pour exciter la réponse sur chaque axe de l'hélicoptère et pour éviter la corrélation avec les autres contrôles. Des conditions de vol dans l'air calme, sans turbulences, ont été considérées.

L'instrumentation de l'hélicoptère pendant les essais

La précision des paramètres estimés est dépendante de la qualité des données des essais en vol mesurées. Des mesures de grande précision des entrées de contrôle et des variables de mouvement sont nécessaires pour l'application des méthodes d'identification des paramètres.

Les données d'essais en vol de Bell 427 sont obtenues à l'aide des sous-systèmes suivants :

a. Un gyroscope laser pour les mesures des vitesses de roulis (p), tangage (q) et lacet (r), et pour des angles de roulis (ϕ), de tangage (θ) et de lacet (ψ) ;
b. Accéléromètres linéaires installés proche du centre de gravité CG de l'avion pour les mesures des accélérations longitudinales, latérales et verticales (a_x, a_y, a_z);
c. Potentiomètres pour mesurer les entrées de contrôle ($\delta_{long}, \delta_{lat}, \delta_{ped}, \delta_{col}$);

d. Un dispositif pour les données de l'air équipé d'un capteur de pression et ailettes pour les mesures suivantes : vitesse totale de l'air (V), angle d'attaque (α) et angle de dérapage (β);
e. Un capteur de pression pour mesurer l'altitude et le taux de montée;
f. Un capteur de température pour mesurer la température extérieure (OAT);
g. Un ordinateur de données de vol qui calcule la position de l'hélicoptère en temps réel (à partir du système de positionnement global GPS) ainsi que le poids de l'hélicoptère et la position de son centre de gravité;

Toutes les données nécessaires pour l'estimation des paramètres ont été numérisées et enregistrées au bord de l'hélicoptère à un taux d'échantillonnage de 50 échantillons par seconde. Pendant les essais en vol, les signaux mesurés ont été envoyés par la télémétrie à la station au sol où la variation dans le temps des variables sélectionnées a été présentée sur des moniteurs et des chartes pour des vérifications rapides. Une réduction des données dans le temps réel a été réalisée pour isoler les inconsistances et les erreurs de transmission des données. En utilisant les vérifications des données en ligne, ensemble avec les commentaires de la part du pilote, il est relativement facile de : a) contrôler les essais; b) détecter les erreurs des données majeures (par ex. fonctionnement mauvais des capteurs, pertes du signal, etc.), imprécisions des données, perturbations (par ex. couplage large dans les contrôles, turbulence, etc.); c) décider si les données sont "bonnes" ou si c'est nécessaire de les répéter. Une partie des données du mouvement de l'hélicoptère ont été très bruyants, donc, un filtrage à basse bande s'imposait sur les mesures de ces données.

La structure du modèle

Le modèle adopté pour l'étude est un modèle sous forme d'espace d'état en six degrés de liberté. Tous les degrés de liberté associés au rotor, aux moteurs, à la transmission de puissance, au système de contrôle et à l'écoulement perturbé, ont été inclus d'une

manière quasi-stationnaire dans les équations de mouvement, et ont perdu leur dynamique individuelle et indépendance comme degrés de liberté dans le réduction du modèle.

Les équations linéarisées générales de la dynamique du système peuvent être écrites sous la forme suivante :

$$\dot{x}(t) = Ax(t) + Bu(t) + Fn(t) + b_x$$

$$z_i = Cx_i + Du_i + G\eta_i + b_z, \quad i = 1,2,... \tag{1}$$

$$x(t_0) = x_0$$

où $x = [u, w, q, \theta, v, p, \phi, r]$ est le vecteur d'état,

x_0 est le vecteur d'état initial,au temps t_0,

$u(t)$ est le vecteur d'entrée de commande $[\delta_{long}, \delta_{lat}, \delta_{ped}, \delta_{col}]$,

z_i est le vecteur des mesures discrètes au temps t_i, $[u_m, v_m, w_m, p_m, q_m, r_m, a_{xm}, a_{ym}, a_{zm}]$.

Les matrices *A, B, C* et *D* contiennent les paramètres inconnus représentant les dérivées de stabilité et de commande et b_z sont des termes qui tiennent compte des conditions initiales non – nulles, des termes relatifs à la gravité et à la rotation dans l'équation des forces et des erreurs systématiques possibles dans les mesures des variables de sortie et de commande.

La matrice F représente la racine carrée de la densité spectrale du bruit d'état et la matrice G représente la racine carrée de la matrice de covariance du bruit de mesures.

Le bruit d'état $n(t)$ est présumé d'avoir une distribution Gaussienne avec une moyenne de zéro et la densité spectrale égale à l'identité. Le vecteur de bruit de mesure, est présumé d'être une séquence de variables aléatoires Gaussiennes indépendantes avec la

moyenne égale à zéro et la covariance égale à l'identité. Il est ensuite assumé que le bruit du processus et le bruit de mesure sont indépendants.

L'identification dans le domaine temporel

La technique d'identification utilisée pour le modèle Bell 427 dans le domaine de temps est la méthode d'estimation de probabilité maximale (en anglais : Maximum Likelihood Estimation Method), incorporée dans une version modifiée par le CNR du programme MMLE3 développée par NASA. Cet algorithme peut manipuler ensemble le bruit du processus et le bruit de mesure, mais pour le programme d'estimation des paramètres de Bell 427, le bruit d'état est assumé nul en se basant sur le fait que les données ont été enregistrées en absence des turbulences (vol calme).

La méthode employée est la méthode de l'erreur à la sortie et l'objectif de cette méthode est l'ajustement des valeurs des paramètres inconnus dans le modèle pour l'obtention du meilleur rapprochement possible entre les données mesurées et la réponse du modèle calculé.

Pendant que tous les paramètres inconnus sont collectés dans un vecteur ξ, l'estimation par la méthode de probabilité maximale du ξ est obtenue en minimisant la fonction négative logarithmique d'estimation (en anglais : Log-Likelohood) donnée par l'équation suivante :

$$LLF(\xi) = \frac{1}{2}\sum_{i=1}^{N} \tilde{z}_i^T \left(GG^T\right)^{-1} \tilde{z}_i + \frac{N}{2}\log\left|GG^T\right| + \frac{Nm}{2}\log 2\pi \qquad (2)$$

où l'erreur $,\tilde{z}_i = z_i - \hat{z}_i$, est calculée par l'estimation $\hat{z}$, qui est produite par une simulation directe de la réponse du modèle, et le produit GG^T est la matrice de covariance du bruit de mesure.

L'estimation de probabilité maximale des paramètres (ML) est obtenue en choisissant la valeur de ξ qui minimise la fonction de coût J_{ML} :

$$J_{ML}(\xi) = \frac{1}{2}\sum_{i=1}^{N} \tilde{z}_i^T \left(GG^T\right)^{-1} \tilde{z}_i \qquad (3)$$

L'ensemble des valeurs des paramètres minimisant la fonction de coût peut se trouver par une méthode d'optimisation. La méthode la plus répandue pour minimiser la fonction de coût dans l'équation (3) est l'algorithme de Newton-Raphson.

Les résultats d'identification générés par le programme MMLE3 sont traités en utilisant Matlab et sont donnés sous forme de graphiques de variation des données mesurées et des réponses du modèle en fonction du temps.

La dernière étape dans la procédure d'identification est la vérification du modèle. Pour cette étape, le modèle d'espace d'état est identifié avec des données de vol non utilisées dans le processus d'identification, pour vérifier la capacité de prédiction du modèle. Les équations sous forme d'espace d'état sont intégrées avec les paramètres de contrôle et de stabilité du modèle gardés constants à leurs valeurs identifiées. Pour valider le modèle, les données d'essais en vol mesurées et la réponse du modèle sont tracées. Les graphiques tracés dans le temps reflètent la capacité de prédiction du modèle identifié.

L'identification dans le domaine de fréquence

Le point de départ dans l'identification dans le domaine de fréquence est la conversion des données basées dans le domaine de temps en données en fréquence.

Le concept général est de : a) extraire un ensemble de réponses en fréquence entrée-sortie non – paramétriques qui caractérisent la dynamique couplée de l'hélicoptère, et b)

conduire une recherche non-linéaire pour un modèle d'espace d'état qui correspond à l'ensemble des données de la réponse en fréquence.

Dans l'approche courante de la réponse en fréquence, l'identification des dérivées de stabilité et contrôle est réalisée directement par un processus itératif d'ajustement de plusieurs entrées et plusieurs sorties des réponses en fréquence identifiées conditionnées avec celles du modèle linéaire suivant :

$$M_m \dot{x} = F_m x + G_m u \tag{4}$$

$$y = H_m x + j_m u \tag{5}$$

Les éléments de M_m, F_m, G_m, H_m et j_m sont les dérivées de stabilité et de contrôle inconnues. En considérant la transformée de Laplace des équations (4) et (5) on obtient la fonction de transfert du modèle sous forme d'espace d'état suivante :

$$T_m(s) = H_m(s)\left[sI - M_m^{-1}F_m\right]^{-1} M_m^{-1} G_m \tau_m(s) \tag{6}$$

Les paramètres inconnus (ξ) du modèle sous forme d'espace d'état sont calculés en minimisant la fonction coût J, une fonction pondérée de l'erreur ε entre les réponses en fréquence $H(\omega)$ du système identifié MISO (plusieurs entrées et une sortie) et les réponses du modèle $T_m(\omega)$ sur une marge sélectionnée des fréquences :

$$J(\xi) = \sum_{n=1}^{n_\omega} \varepsilon^T(\omega_n, \xi)\, W \varepsilon(\omega_n, \xi) \tag{7}$$

Les intervalles de fréquence pour le critère d'identification sont sélectionnés individuellement pour chaque entrée et sortie en fonction de leurs marges individuelles de bonne cohérence. De cette manière, seules les données valides sont utilisées dans le processus d'optimisation. La matrice de pondération W est basée sur les valeurs de la cohérence pour chaque point de fréquence pour mettre l'emphase sur les plus précises données. Un algorithme de recherche non – linéaire itératif est utilisé pour optimiser les

dérivées de stabilité et contrôle et les délais de temps dans le modèle jusqu'au moment que la convergence sur un critère minimum de l'équation (7) est achevée.

L'analyse de plusieurs entrées des contrôles de l'hélicoptère Bell 427 a montré la présence d'un très grand couplage entre les différents axes de commande. L'activité de contrôle en hors de l'axe principale de commande est apparue suite au couplage et la nécessité de rester proche de la condition d'équilibre. La présence des entrées secondaires corrélées fausse la réponse identifiée pour chaque entrée de contrôle.

La conclusion était que les réponses individuelles pour chaque axe de contrôle sont acceptables et cela est faisable pour déterminer un modèle latéral et / ou longitudinal mais il est impossible d'obtenir un modèle en couplage plein.
La vérification du modèle est faite en comparant la réponse du modèle simplifié identifié avec les données d'essais en vol pas utilisées pour générer le modèle. Les paramètres sont fixés aux valeurs identifiées et le modèle est conduit avec les entrées mesurées de contrôle pour calculer la réponse du modèle. Afin de comparer, la sortie du modèle et les données d'essais en vol mesurés sont tracés.

Conclusions

Le modèle en six degrés de liberté en couplage n'inclut pas les modes du rotor principal aux hautes fréquences. Il est cependant capable de modéliser la dynamique des hélicoptères assez précis. Même si les variables d'état du rotor ont été omises explicitement, la dynamique du rotor peut être modélisée comme des délais dans le temps entre les entrées de contrôle du rotor et la réponse aérodynamique. Même si ce délai peut être petit, celui-ci peut encore affecter le comportement des modes rigides plus rapides. Ce délai dans le temps pour chacun des quatre contrôles a été introduit dans la formulation du modèle comme compromis.

Le processus d'identification dans le domaine du temps a été un succès dans l'analyse de toutes les conditions de vols testées et des très petites différences ont été obtenues entre les réponses mesurées et prédites impliquant la bonne qualité du modèle. Les dérivées ont été utilisées pour l'obtention et l'identification des modes naturels de l'hélicoptère.

La fonction de réponse en fréquence est un outil d'analyse robuste, même si plus d'effort de calcul que dans le domaine de temps est requis. Pour les données de réponse en fréquence il est plus difficile et il faut plus du temps pour les obtenir lors d'essais en vol.

Tous les deux logiciels MMLE3 et CIFER contiennent des algorithmes sophistiqués de recherche pour trouver un ensemble des valeurs des paramètres qui fournissent les meilleurs résultats en concordance à la fonction de coût adoptée. Le choix des méthodes dépends de l'application, la formulation de la fonction de coût, la familiarité de l'utilisateur avec les méthodologies respectives, et finalement la disponibilité des outils de calcul.

Recommandations

Pour l'analyse dans le domaine de temps, une version non-linéaire de l'estimateur de probabilité maximale va étendre la capacité de la technique d'identification.

La réponse en fréquence montre que les caractéristiques du rotor d'hélicoptère aux hautes fréquences ne peuvent pas être décrites par le modèle rigide seulement, mais un modèle avec 9 degrés de liberté en combinant la dynamique des modes rigides avec la dynamique du rotor est nécessaire.

Les données des essais en vol doivent fournir autant information que possible sur la dynamique de l'hélicoptère dans la marge des fréquences d'intérêt. Les manœuvres d'essais en vol ont eu une durée d'approximativement 20 secondes et ne pouvaient pas donner d'informations suffisantes sur les fréquences basses.

Le signal d'entrée de type 2311 est plus convenable pour les techniques d'identification dans le domaine de temps alors qu'une entrée de type balayage en fréquence est préférable pour l'approche dans le domaine de fréquence.

Les manœuvres d'essais en vol doivent être répétées pour la redondance. En plus des essais conçus pour l'identification, des essais en vol avec d'autres signaux à l'entrée (par exemple des doublets) doivent être utilisés pour la vérification des modèles identifiés.

ACKNOWLEDGEMENTS

The work reported here was financed by Bell Helicopter Textron Canada and the Consortium for Research and Innovation in Aerospace in Quebec (CRIAQ) and was carried out in collaboration with the National Research Council Canada and École Polytechnique de Montréal. I wish to offer thanks to all those who made this project highly enjoyable and challenging and who have answered any questions I had during its course. Without them, I would not have been able to accomplish this milestone.

I would like to express my deeply gratitude to the supervisor of this thesis, professor Ruxandra Botez, and the co-supervisor, professor Njuki Mureithi for their supervision and guidance. They have provided me with knowledge and all the necessary resources to reach my goals, thus making it possible to proceed with the progress.

I gratefully acknowledge the support provided by the Handling Qualities team at BHTCL: M. Edward Lambert, M. Joey Seto and M. Daniel Gratton, for their invaluable suggestions and generous support throughout the course of this research. Also acknowledged is the support provided by the Bell 427 joint flight test team of BHTCL, for providing the data which were analyzed in this thesis and also for many useful technical discussions and advice.

I would like to express my appreciation to my friend Bogdan Mijatovic for providing a pleasant friendly and supportive environment during the pursuit of my research.

I highly appreciate the scholarship award offered to me by the Training Deanship from École de Technologie Supérieure.

I owe much thanks to M. Adrian Hiliuta, post-doc researcher, for his informed advice that were very useful to me.

Last, not least, the moral support and the acceptance of divided attention by my family is recognized with warm appreciation.

TABLE OF CONTENTS

Page

LIST OF TABLES

Page

LIST OF FIGURES

Page

NOTATIONS

a_x	Acceleration component along the longitudinal body axis
a_y	Acceleration component along the lateral body axis
a_z	Acceleration component along the normal body axis
b	Bias
bw	Bandwidth
GM	Gain Margin (of open loop response)
L	Component of the resultant aerodynamic moment about the longitudinal body axis. *In derivatives*: Derivative of $\widetilde{L}$
$\widetilde{L}$	Component of the specific resultant aerodynamic moment about the longitudinal body axis
L_p	Roll damping derivative
M	Component of the resultant aerodynamic moment about the lateral body axis. *In derivatives*: Derivative of $\widetilde{M}$
$\widetilde{M}$	Component of the specific resultant aerodynamic moment about the lateral body axis
N	Component of the resultant aerodynamic moment about the normal body axis. *In derivatives*: Derivative of $\widetilde{N}$
$\widetilde{N}$	Component of the specific resultant aerodynamic moment about the normal body axis
p	Roll rate
s	Laplace variable
T	Period length
u	Component of the air velocity along the longitudinal body axis
v	Component of the air velocity along the lateral body axis
w	Component of the air velocity along the normal body axis

X Component of the resultant aerodynamic force along the longitudinal body axis. *In derivatives*: Derivative of $\widetilde{X}$

$\widetilde{X}$ Component of the specific resultant aerodynamic force along the longitudinal body axis

Y Component of the resultant aerodynamic force along the lateral body axis. *In derivatives*: Derivative of $\widetilde{Y}$

$\widetilde{Y}$ Component of the specific resultant aerodynamic force along the lateral body axis

Z Component of the resultant aerodynamic force along the normal body axis. *In derivatives*: Derivative of $\widetilde{Z}$

$\widetilde{Z}$ Component of the specific resultant aerodynamic force along the normal body axis

α Angle of attack

β Angle of sideslip

γ Coherence function

δ Control deflection

Δ Finite variation

δ_{lat} Lateral control input

ζ Damping ratio

θ Pitch angle

λ Eigenvalue

τ Time delay

ϕ Roll angle

ψ Yaw angle

ω Angular frequency = 2π f

∇ Hamilton symbol for a differential operator, e.g. gradient of a scalar field

ABBREVIATIONS

A/C	Aircraft
AIAA	American Institute of Aeronautics and Astronautics
CIFER	Comprehensive Identification from FrEquency Response
CG	Center of Gravity
CZT	Chirp-Z transform
DFVLR	German Aerospace Center
DoF	Degrees of Freedom
FADEC	Full Authority Digital Engine Control
FFT	Fast Fourier Transform
GPS	Global Positioning System
HQ	Handling Qualities
IC	Instrumentation Center
LTI	Linear Time Invariant
MAP	Maximum a Posteriori
MIMO	Multiple-Input/Multiple-Output
MISO	Multiple-Input/Single-Output
ML	Maximum Likelihood
MMLE	Modified Maximum Likelihood Estimation
MTE	Mission-Task-Element
NASA	National American Space Agency
NRC	National Research Council
OAT	Outside Air Temperature
PIO	Pilot-Induced Oscillations
RPM	Revolutions Per Minute
SI	International Unit System
SISO	Single-Input/Single-Output

INTRODUCTION

A model is a representation of the essential aspects of an existing system (or a system to be constructed) which presents knowledge of that system in a usable form [1].

System identification is an iterative model building process used to obtain an accurate mathematical description from measured system responses [2]. When applied to an aircraft, system identification is a procedure by which a mathematical description of vehicle dynamic behavior is extracted from flight test data (measured aircraft motion).

The field of aircraft stability and control exemplifies a successful application of system identification technology. By identifying stability and control derivatives from flight test data, accurate linear models can be used for control law design or in the estimation of handling qualities parameters. In cases where wind-tunnel data are unavailable or where flight safety into untested regions is of concern, flight-calculated derivatives are extrapolated to predict aircraft behavior prior to flight into these regions. High-fidelity simulators require stability and control data giving an accurate representation of the actual flight vehicle.

Unlike the flight dynamics of most fixed wing aircraft, the dynamics of rotary wing aircraft are characteristically those of a high order system. The large number of degrees of freedom associated with the coupled rotor-body dynamics leads to a large number of unknown parameters to be estimated. Based on previous experience in rotorcraft parameter estimation, it has been agreed that at least a 6 DoF model formulation is necessary to describe helicopter flight dynamics. The coupled, 6 DoF model does not include the high frequency main rotor modes (flapping, lead-lag, twisting), yet it is capable of modeling rotorcraft dynamics fairly accurately [3].

The coordinated approach to rotorcraft system identification is divided into three major parts [2]: a) instrumentation and filters, which covers the entire flight data acquisition process including adequate instrumentation and airborne or ground-based digital recording equipment; b) flight test techniques, which are related to the selected helicopter maneuvering procedures. The input signals have to be optimized in their spectral composition to excite all response modes from which parameters are to be estimated; c) analysis of flight data, which includes the mathematical model of the helicopter and an estimation criterion devising a suitable computational algorithm to adjust starting values or a priori estimates of the unknown parameters until a set of best parameter estimates that minimizes the response error is obtained.

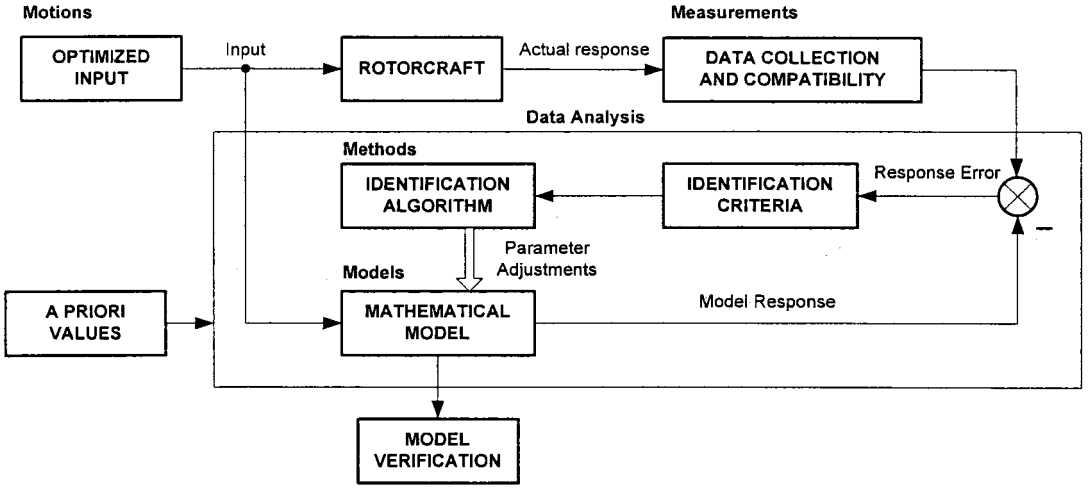

Figure 1 The basic concept of helicopter system identification

Corresponding to these strongly interdependent topics, four important aspects of system identification have to be carefully treated [2] (Figure 1):

a. optimal maneuver design in order to excite all modes of the helicopter dynamics;

b. accurate data gathering of system inputs and outputs involving measurement techniques;
c. mathematical models and the corresponding simulation describing the phenomenon being investigated;
d. estimation methods to extract unknown parameters including model structure determination.

CHAPTER 1

BASICS OF SYSTEM IDENTIFICATION

1.1 General description of Bell 427

The Bell 427 is designed as a multiple purpose light helicopter. It is ideally suited for a wide variety of applications including executive and commuter transport, and cargo missions. The Bell 427 has a normal gross weight of 6350 lb and a maximum cruising speed of up to 135 knots. A three view drawing of the Bell 427 is given in Figure 2.

The pilot control inputs are augmented by hydraulic servo actuators. Movement of the cyclic stick is transmitted through the servo actuators to the swash plate, which actuates the rotating controls to the main rotor. A mechanical linkage through the collective servo actuator to the swash plate collective lever transmits movement of the collective control stick. The pedals provide the ability to control the tail rotor thrust in order to compensate for engine torque and to control the directional heading of the helicopter. The hydraulic servo actuator reduces the force required to move the pedals.

Prior to being transmitted to the rotor system, all cyclic and collective movements are transmitted through the mixing bell crank, which is located at the bottom of the control column. The mixing bell crank coordinates control movement so that when blade pitch is changed by moving the collective stick, the cyclic servo actuators and linkage also move in order to keep the swash plate in its relative plane.

The Bell 427 main rotor system uses a soft-in-plane flex beam type hub with composite main rotor blades. It consists of a single composite yoke, elastomeric dampers and lead-lag/pitch change bearings, metallic pitch horns, grips, and mast and blade attachment components.

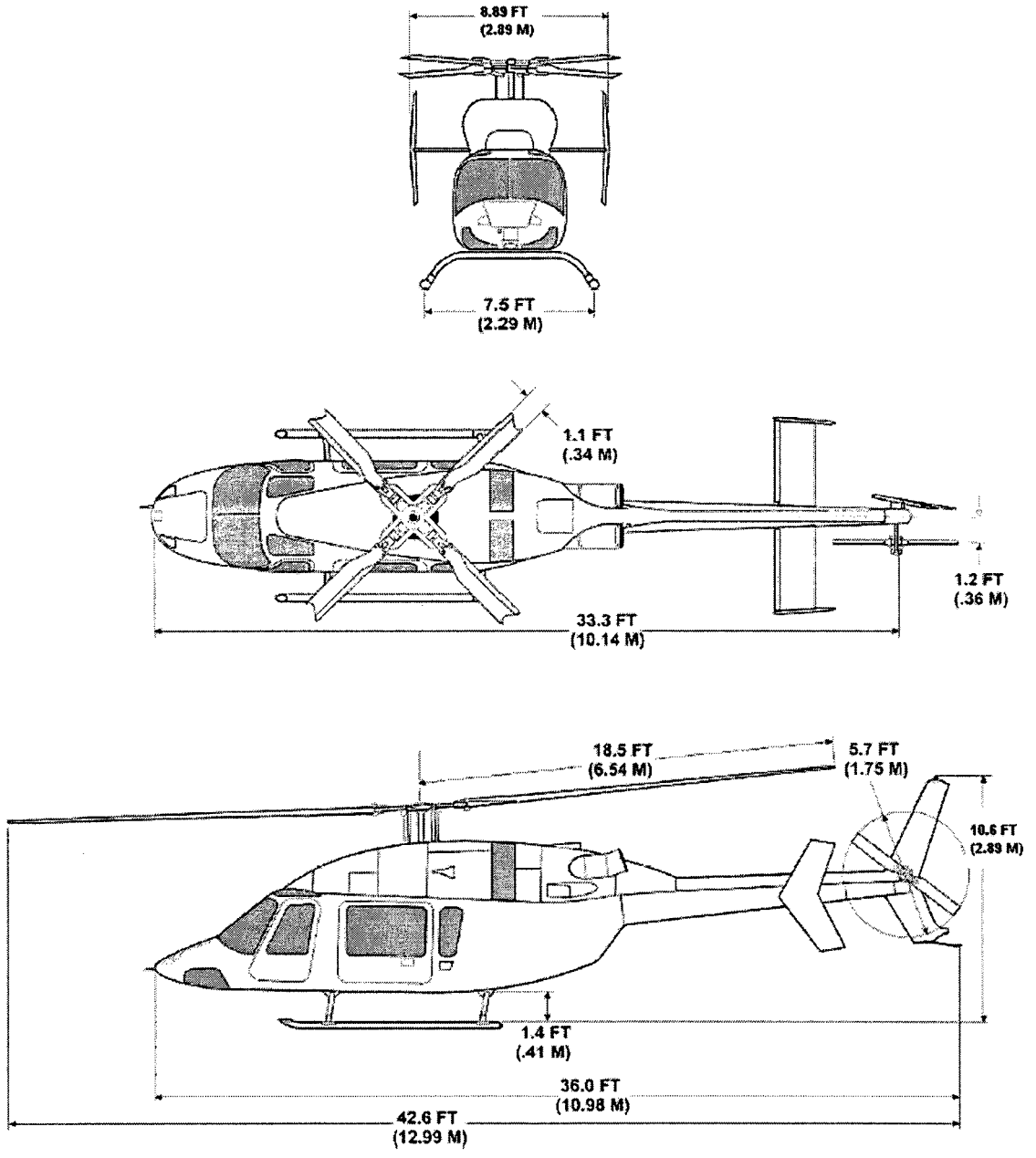

Figure 2 A three view drawing of Bell 427

The four individually replaceable main rotor blades are constructed of composite materials. Each blade assembly consists of a fiberglass spar, Nomex honeycomb core, fiberglass skins and trailing edge strips, and a leading-edge stainless steel abrasion strip. The design RPM is 395 rot/min with a tip speed of 765 ft/sec (233 m/s). Airfoil sections of the blade vary along the span.

The tail rotor is a two bladed teetering pusher type with composite blades, a metallic yoke, and elastomeric flapping bearing. The two tail rotor blades are constructed with fiberglass fabric skins, a unidirectional fiberglass/epoxy spar, and a nomex honeycomb core for corrosion avoidance. The design RPM is 2375 rot/min with a tip speed of 705 ft/sec (215 m/sec).

The Bell 427 helicopter is powered by two Pratt & Whitney PW207D turbo shaft engines. The engine fuel control system is a single channel Full Authority Digital Electronic Control (FADEC) with hydro mechanical backup. Each Pratt & Whitney PW207D turbo shaft engine is rated at 710 shp (529 kW) for takeoff (5 minutes), and 625 shp (466 kW) for maximum continuous power.

1.2 Optimal input design

Accuracy and reliability of parameter estimations depend on the amount of information available in the aircraft response. A good testing design accounts for practical constraints considered during the flight tests, while minimizing the flight test time [4]. The overall goal is the design of an experiment producing data from which model parameters can be accurately estimated. In this way, the system modes are excited so that the sensitivities of the model outputs to the parameters are high and correlations between parameters are low.

The design of an optimal input for accurate model parameter estimation requires high excitation of the system, which is opposite to practical constraints considered in flight-testing. One such practical constraint is the requirement that the output amplitude (e.g., in angle of attack or sideslip angle) variations about the flight test trim condition are limited to ensure the validation of the presumed model structure. Input amplitudes should be constrained for the same reasons, and in addition, to avoid non-linearities such as mechanical stops and rate limiting when the model is linear.

The inputs should excite all the modes of the analyzed model and should minimally excite the un-modeled modes. The system modes are best excited by frequencies near the system natural frequencies. Input frequencies much higher than the system natural frequencies give negligible responses, or excitation of higher frequency un-modeled modes. Very low input frequencies may result in static data.

The first form of multi-step test input signal that is traditionally used for the identification of fixed-wing aircraft is the doublet input. This input excites the short period mode in the longitudinal motion and the Dutch roll in the lateral mode. For a helicopter, although doublet inputs are of limited value, they are capable of exciting the modes in each axis. The doublet inputs are used together with other types of inputs, as they are not ideal for the highly coupled helicopter model.

The second form of multi-step test input signal which is used widely for rotorcraft and aircraft system identification is the "3-2-l-1" band-optimized signal. Figure 3 shows the Power Spectral Density (PSD) of four types of inputs: step, doublet, 3211 signal and a 3211 improved signal, as function of the normalized frequency [2]. Note that the multi-step input signal 3211 was developed by Koehler at Deutsche Forschungs und Versuchsanstalt für Luft und Raumfahrt (DFVLR).

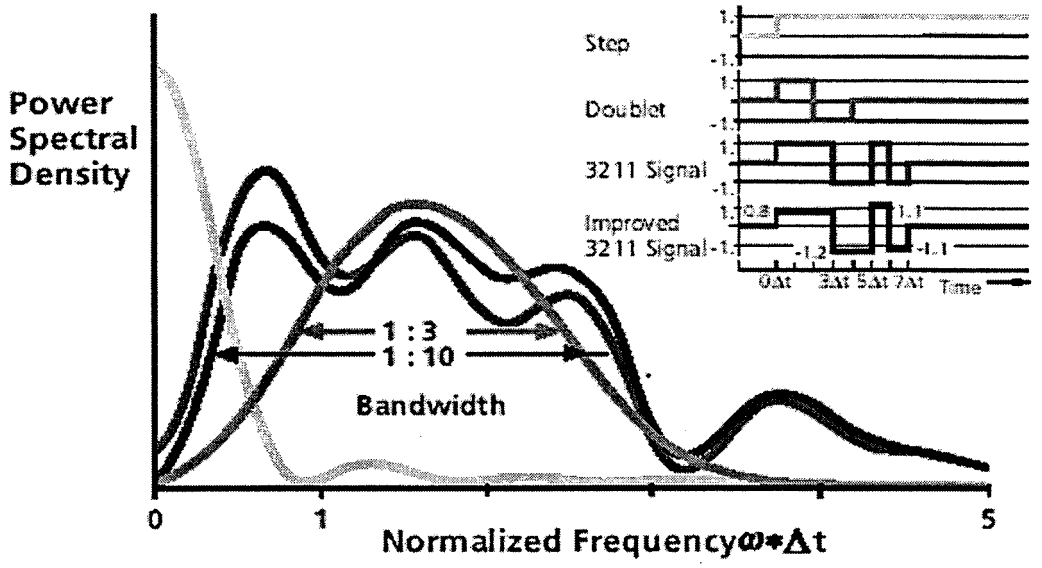

Figure 3 Frequency spectra of typical inputs

For the Bell 427 Parameter Estimation Program, the aircraft motion is perturbed from trim position by applying a sequence of time-domain control pulses of varying lengths and alternating signs, referred to as 2311 control inputs, where the digits refer to the number of unit time intervals between control reversals (Figure 4). This input is similar to the DFVLR 3211 multi-step input except that in the Bell 427 case the first step is 2 s long and the second step is 3 s long. The length of the unit pulse should be a quarter period of the main response mode [5]. The multistep control input was used for separate excitation of pitch, heave, roll and yaw. Following to 2311 input, the controls are returned to their nominal trim positions.

The common feature to all acceptable inputs is the presence of step variations represented in Figure 4 in the form of rapid and distinct changes in slopes. Results indicate that as long as these steps are present, relatively simple inputs are very efficient to obtain good estimates of the stability and control derivatives.

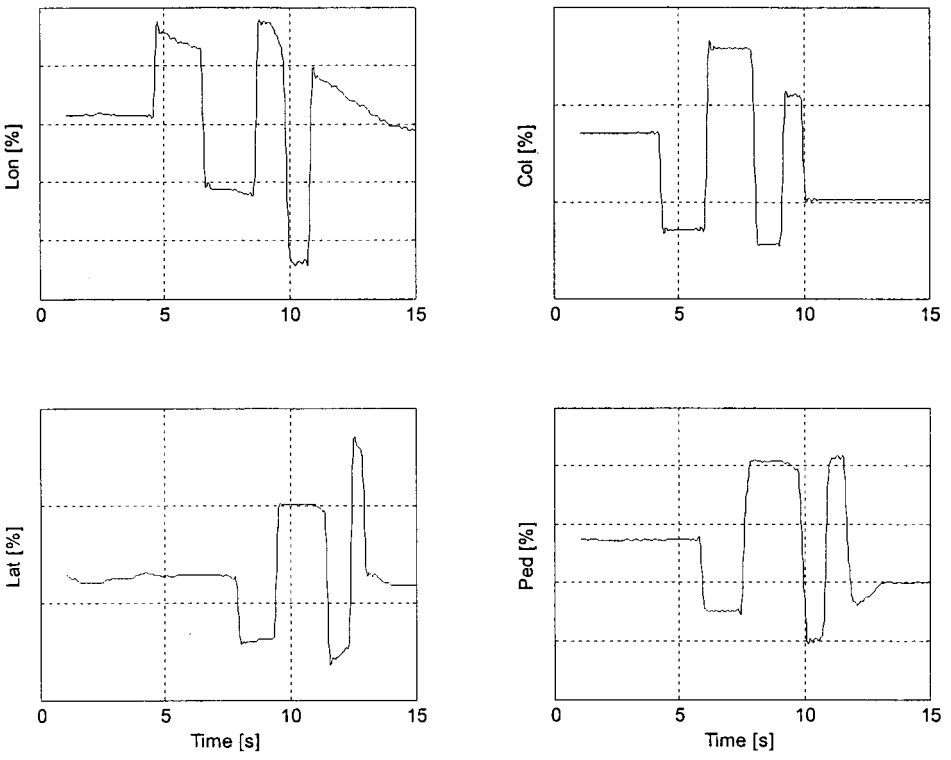

Figure 4 Independent 2311 four-axes control inputs for Bell 427

The advantages of the 2311 control input are:

a. sufficiently high frequency content, provided by the alternating input strokes, in order to improve control derivative estimation;
b. ability to excite all the natural aircraft modes;
c. short time duration, easy to execute and to repeat;
d. no excitation of the higher frequency rotor modes, which are not included in the 6 DoF model.

Small maneuvers are suited to locally linearized aerodynamic models. Large maneuvers exceed the range of validity of locally linearized models and thus necessitate the use of nonlinear aerodynamic models. By use of small and large maneuvers models, the lower and upper bounds of the acceptable maneuver amplitudes are calculated. For most

aircraft, the range between the lower and upper bounds is large, thus the best maneuver amplitudes are those located near the middle of their acceptable maneuver range [6].

The frequency sweep test techniques are recently used in the field of rotorcraft system identification, by Tischler et al. [7]. The frequency bandwidth of interest depends on the test objectives. For helicopter flying qualities studies, the typical frequency range of interest is between 0,5 Hz and 2 Hz. In cases where the test objectives include rotor modes identification, the maximum frequency range of interest may be as high as 6 Hz [8]. In the frequency sweep tests, the pilot produces a sinusoidal input about a reference trim condition, beginning at very low frequency and progressively increasing the inputs frequency. Thus, the frequency sweep test should contain at least 3 s of static trim data at the beginning and the end of the record. The total record length should be three to four times the maximum period of interest, i.e. a 60-90 s record length [7]. Figure 5 depicts a typical lateral frequency sweep.

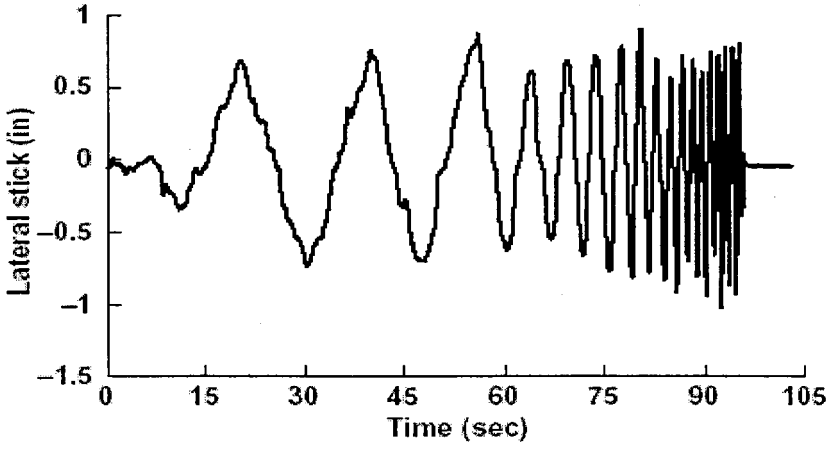

Figure 5 Typical lateral frequency sweep

1.3 Flight test instrumentation

The accuracy of the parameter estimates is directly dependent on the quality of the flight test measured data, and hence, high accuracy measurements of the control inputs and of the motion variables are a prerequisite for the successful application of the methods of flight vehicle system identification.

The Bell 427 flight test data for system identification purposes were mainly obtained from the following subsystems:

a. a laser gyro package for the roll, pitch and yaw rates (p, q, r), for the roll and pitch attitude (φ, θ) and for the heading angle (ψ) measurements;
b. linear accelerometers installed near the aircraft center of gravity (CG) for the longitudinal, lateral and vertical accelerations measurements (a_x, a_y, a_z);
c. potentiometers to measure the pilot control inputs (δ_{long}, δ_{lat}, δ_{ped}, δ_{col});
d. a swivel-head air data boom equipped with pressure sensors and vanes for the following measurements: total air speed, angle of attack α and sideslip angle β; the nose boom is mounted in front of the helicopter to avoid main rotor wake interactions;
e. a pressure transducer for altitude, rate of climb and airspeed measurements;
f. an Outside Air Temperature (OAT) probe for temperature measurements;
g. a flight test computer for the real time helicopter positioning (from Global Positioning System data, GPS) and weight and balance calculations.

In order to avoid larger changes in the helicopter mass and the CG location during the flight, the helicopter was refueled after one hour of flying time. The tests were performed in level flight, moderate and fast climb, moderate descent and fast descent, over a speed range of 30 knots to 110 knots at intervals of 20 knots.

Within one test run, only one control at a time was used to excite the on-axis response of the helicopter and to avoid correlation with other controls. Figure 6 shows some typical responses of the helicopter to on-axis input signals.

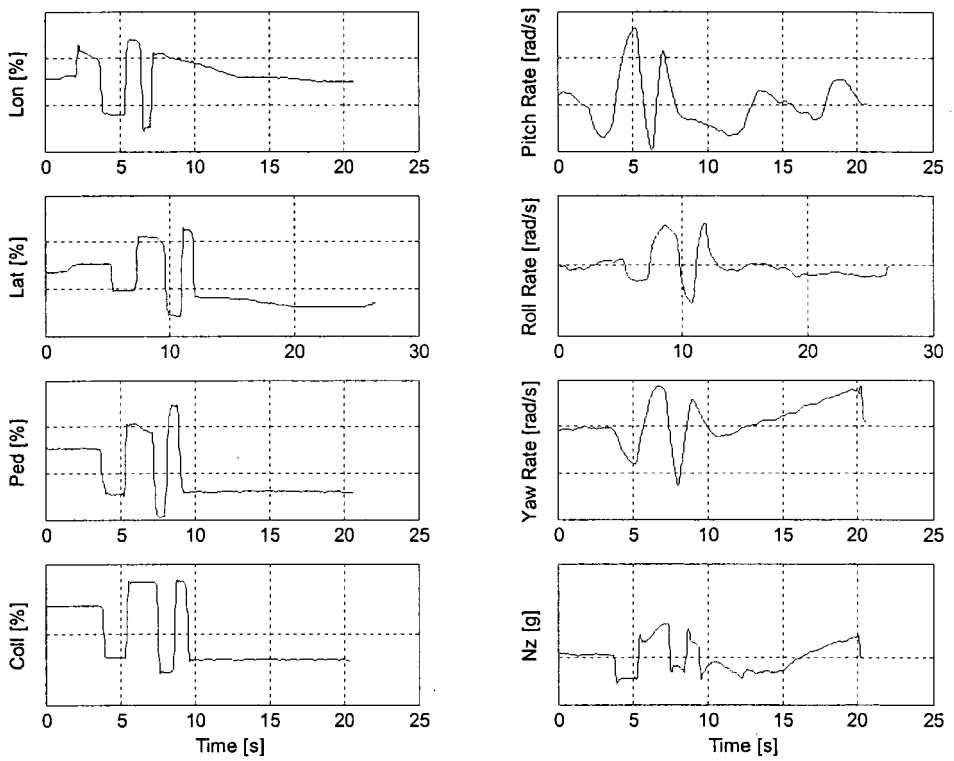

Figure 6 Characteristic helicopter responses to different inputs

All data needed for the parameter estimation were digitized and recorded on board of the helicopter at a sample rate of 50 samples/sec. During the flight tests, the measured signals were sent by telemetry to the ground station where the time-histories of selected variables were presented on both monitors and strip charts for quick on-line verification.

Real-time data reduction was conducted to isolate data inconsistencies and data transmission errors. By use of these on-line data checks together with pilot's comments it was relatively easy to: a) control the tests; b) detect major data errors (e.g. sensor

malfunction, spikes, etc.), data inaccuracies, disturbances (e.g. drifts, large coupling in controls, turbulence, etc.); c) decide if the data point was a "good" one or if it needed to be repeated.

The off-line data processing for system identification purposes included:

a. conversion to the same system of units;
b. detection and removal of data dropouts;
c. low-pass filtering;
d. corrections for the center of gravity;
e. calculation of additional variables, such as the speed components u, v, w.

Table I and Table II show the sign conventions for the control positions and for the measured response variables.

Table I

Sign conventions used for control positions

Control position	**Positive sign convention**	**Neutral (zero) convention**
Longitudinal stick position	Cyclic stick moves forward	Full aft stick
Lateral stick position	Cyclic stick moves to the right	Full left stick
Directional pedal position	Right pedal moves forward	Full left pedal
Collective stick position	Blade angle increases	Stick is in position of smallest blade angle

Table II

Positive sign conventions for response variables

Data set	Response variable	Positive sign convention
Air data	Angle of attack α	A/C nose moves up
	Sideslip angle β	A/C nose moves to the left
	True airspeed V	Forward
	Longitudinal airspeed u	Forward
	Lateral airspeed v	Right
	Vertical airspeed w	Upward
Linear accelerations	Longitudinal acceleration a_x	Forward
	Lateral acceleration a_y	To the right
	Vertical acceleration a_z	Downward
Attitude angles	Bank angle (roll angle) ϕ	Helicopter turns clockwise about roll axis as seen from rear
	Pitch angle θ	A/C nose moves up
	Yaw angle ψ	Helicopter turns clockwise about yaw axis as seen from above
Angular rates	Roll rate p	Helicopter turns clockwise about roll axis as seen from rear
	Pitch rate q	A/C nose moves up
	Yaw rate r	Helicopter turns clockwise about yaw axis as seen from above

Some of the helicopter motion measurements were very noisy, thus, a low-pass filtering was applied on these data measurements. Analog filters reduce the high frequency amplitudes and influence the phase characteristics of the measured signal. For example, in the case of high order filters, the phase shifts may be significant at frequencies far below the filter cut-off frequency. The identification is based on the amplitude and phase relationship between the individual measurements, and for this reason, filters may deteriorate identification results. Zero-phase shift digital filters were applied in order to eliminate the unwanted higher frequency effects and noise and to reduce the sampling rate.

Most of the quantities of interest (displacements, speeds and accelerations) are referred to helicopter body axes, as shown in Figure 7. The origin of the body-axes system is at the CG. The entire axis system moves and rotates with the helicopter. The x-axis is always parallel to the fuselage reference line and in case where the CG is in the plane of symmetry, both the x and z-axes are in the aircraft's symmetrical plane. The y-axis is normal to the plane of symmetry.

In Figure 7, X, Y, Z are the forces, L, M, N are the moments, u, v, w are the linear speeds, and p, q, r are the angular rates. The aircraft attitude with respect to the inertial system is defined by the three Euler angles ψ (heading angle), θ (pitch attitude), and ϕ (roll attitude). The body-axis helicopter angular rates (p, q, r) are defined as projections of the angular velocity vector (with respect to the inertial system of coordinates) on the body axes [9].

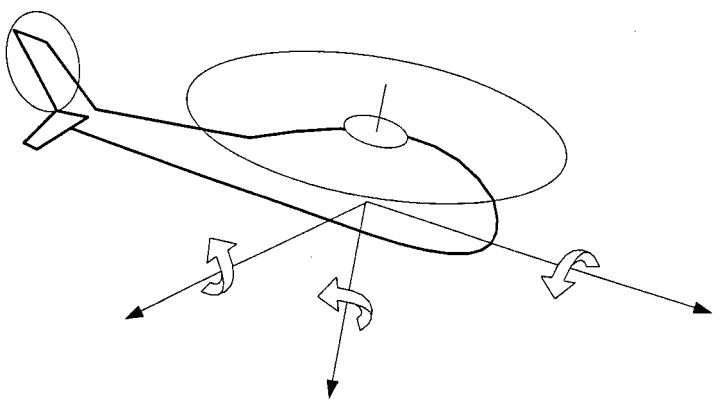

Figure 7 The orthogonal axes system for helicopter flight dynamics

The roll rate p, pitch rate q, and yaw rate r are the components of the angular velocity in the body-axis system of coordinates, $\dot{\phi}$, $\dot{\theta}$, and $\dot{\psi}$:

$$\begin{aligned} p &= \dot{\phi} - \dot{\psi}\sin\theta \\ q &= \dot{\theta}\cos\phi + \dot{\psi}\cos\theta\sin\phi \\ r &= \dot{\psi}\cos\theta\cos\phi - \dot{\theta}\sin\phi \end{aligned} \tag{1.1}$$

The angle of attack (α) and angle of sideslip (β) vanes measure the local flow direction. The effects of flow components resulting from angular velocities and flight path curvature introduce errors in the measured flow angles with respect to the true angle of attack or the sideslip angle [10].

In order to use the angle of attack α in the true airspeed measurement point, it has to be changed from the CG point to the instrumentation centre (IC) of true airspeed:

$$\alpha_{IC} = \alpha_{CG} - \frac{x_\alpha}{V^2}\left(a_{zCG} - g\cos\theta\cos\phi\right) - \frac{x_\alpha}{V}q \tag{1.2}$$

where x_α is the distance (along the x axis direction) between the α vane and the aircraft CG, V is the true airspeed, a_{zCG} is the normal acceleration at the CG and q is the pitch rate.

In order to correct the sideslip angle measured at IC with respect to CG, by taking into consideration the yaw rate r and roll rate p effects, the expression of the sideslip angle is written as follows:

$$\beta_{IC} = \beta_{CG} + \frac{x_\beta}{V}r - \frac{z_\beta}{V}p \tag{1.3}$$

where x_β is the distance (along the x axis direction) and z_β is the distance (along the z axis direction) between the β vane and the aircraft CG and p and r are the roll rate and the yaw rate, respectively.

The sideslip vane measures the flank angle of attack, α_f, as defined by Figure 8:

$$\alpha_f = \tan^{-1}\frac{v}{u} \tag{1.4}$$

The real sideslip angle, β_{IC}, at the IC is further expressed from Figure 8 as follows:

$$\beta_{IC} = \tan^{-1}\left(\tan\alpha_f \cdot \cos\alpha\right) \tag{1.5}$$

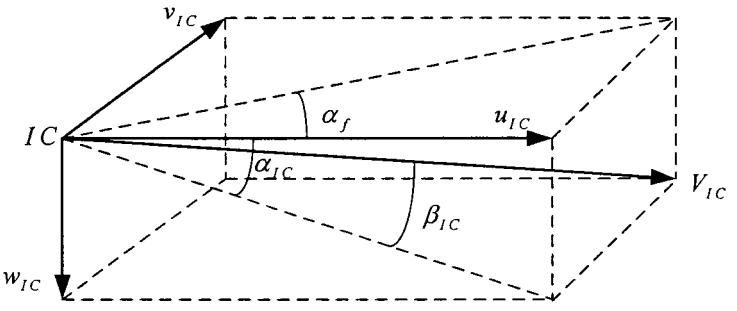

Figure 8 The correction of sideslip angle β

The longitudinal, lateral and normal speed components at the sensor position (IC) are calculated as functions of the true airspeed, angle of attack and angle of sideslip at the IC:

$$\begin{aligned} u_{IC} &= V\cos\alpha_{IC}\cos\beta_{IC} \\ v_{IC} &= V\sin\beta_{IC} \\ w_{IC} &= V\sin\alpha_{IC}\cos\beta_{IC} \end{aligned} \tag{1.6}$$

The true airspeed at IC is written as a function of the V at CG:

$$\overline{V}_{IC} = \overline{V}_{CG} + \overline{\omega}\times\overline{r} \tag{1.7}$$

Using Equation (1.7) the true airspeed at CG is expressed as:

$$\overline{V}_{CG} = \overline{V}_{IC} - \overline{\omega}\times\overline{r} \tag{1.8}$$

The vector product between angular velocity, $\bar{\omega}$, and the position vector, $\bar{r}$, is written as follows:

$$\bar{\omega}\times\bar{r}=\begin{vmatrix}\bar{i} & \bar{j} & \bar{k}\\ p & q & r\\ x & y & z\end{vmatrix}=\bar{i}(qz-ry)+\bar{j}(rx-pz)+\bar{k}(py-qx) \tag{1.9}$$

The speed components at the CG are obtained by replacing Equation (1.9) in Equation (1.8), as follows:

$$\begin{aligned} u_{CG} &= u_{IC}-qz+ry\\ v_{CG} &= v_{IC}-rx+pz\\ w_{CG} &= w_{IC}-py+qx \end{aligned} \tag{1.10}$$

The true airspeed at the CG, V_{CG}, results from the following equation:

$$V_{CG}=\sqrt{u_{CG}^2+v_{CG}^2+w_{CG}^2} \tag{1.11}$$

where u_{CG}, v_{CG}, w_{CG}, are given by Equation (1.10).

The distance between the sensor position and the helicopter CG affects the measurements of linear accelerations because the measured signals will contain acceleration components due to the helicopter angular motion.

The accelerations can be obtained by differentiation of the speed given by Equation (1.8):

$$\dot{\bar{a}}_{CG}=\dot{\bar{V}}_{CG}=\dot{\bar{V}}_{IC}-\dot{\bar{\omega}}\times\bar{r}-\bar{\omega}\times\dot{\bar{r}}=\dot{\bar{a}}_{IC}-\dot{\bar{\omega}}\times\bar{r}-\bar{\omega}\times\dot{\bar{r}} \tag{1.12}$$

But, since

$$\dot{\bar{r}}=\bar{\omega}\times\bar{r} \tag{1.13}$$

Equation (1.12) can be written in the following form:

$$\bar{a}_{CG}=\bar{a}_{IC}-\dot{\bar{\omega}}\times\bar{r}-\bar{\omega}\times(\bar{\omega}\times\bar{r}) \tag{1.14}$$

The airframe is considered rigid thus, $\dot{y}=\dot{x}=\dot{z}=0$; using this, the linear accelerations at the CG ($a_{xCG}, a_{yCG}, a_{zCG}$) are written in fully expanded form as follows:

$$
\begin{aligned}
a_{xCG} &= a_{xIC} + x\left(q^2 + r^2\right) - y\left(pq - \dot{r}\right) - z\left(pr + \dot{q}\right) \\
a_{yCG} &= a_{yIC} + y\left(r^2 + p^2\right) - z\left(qr - \dot{p}\right) - x\left(qp + \dot{r}\right) \\
a_{zCG} &= a_{zIC} + z\left(p^2 + q^2\right) - x\left(rp - \dot{q}\right) - y\left(rq + \dot{p}\right)
\end{aligned}
\tag{1.15}
$$

Equations (1.15) show that the rotational accelerations ($\dot{p}, \dot{q}, \dot{r}$) are needed to correct the linear acceleration measurements at the CG. Because no measurements were available, the differentiated rates were used.

1.4 Model structure

The choice of a model structure is a critical step in system identification, which might affect both the degree of difficulty in extracting the unknown parameters, and the utility of the identified model in its intended application. Simple decoupled models characterizing the helicopter dynamics over a limited frequency range are suitable for handling qualities applications, while coupled 6 DoF models covering a broader frequency range are needed for simulator applications. In the case of advanced high bandwidth rotorcraft flight control system design, these models should consider the coupled fuselage/rotor/air mass dynamics. The best choice is the simplest model structure that serves the intended application [3].

Model structures can be broadly divided into two groups: nonparametric and parametric [11]. A nonparametric model is one in which no model order or form of the differential equations of motion is assumed. Nonparametric models are expressed as frequency responses between key input/output variable pairs (e.g. pitch-rate response to longitudinal stick) which are calculated using Fast Fourier Transform techniques. Nonparametric models are presented in Bode plot format of Log-magnitude and phase of the input-to-output transfer function versus frequency. Typical applications of nonparametric identification results are handling-qualities analyses based on bandwidth and phase delay and simulation model validation.

The parametric model requires the assumption of both system order and the structure of the system's dynamical equations. The simplest parametric model structure is a transfer function, which is a pole-zero representation of the input-to-output relationship; these parametric models have relatively few unknown parameters. A more complex parametric model is a full 6 DoF (or higher) set of coupled linear differential multi-input/multi-output (MIMO) state-space equations, derived from Newton's laws applied to the helicopter model. Common applications of parametric models include control system design, wind-tunnel model validation, and mathematical model derivation and validation.

The adopted model for this study was a fully coupled, 6 DoF state space model [12]. All higher degrees of freedom, associated with the rotor, power plant/transmission, control system and the disturbed airflow, were embodied in a quasi-steady manner in the equations of motion, and have lost their own individual dynamics and independence as degrees of freedom in the model reduction.

The basic flight dynamics equations are the linear momentum and angular momentum equations:

$$\overline{F} = \frac{d}{dt}\left(m\overline{V}\right) \tag{1.16}$$

$$\overline{M} = \frac{d}{dt}\left(\overline{H}\right) \tag{1.17}$$

where $\overline{F}$ is the external applied force, $\overline{M}$ is the external applied moment about the center of gravity, $\overline{V}$ is the true airspeed vector, and $\overline{H}$ is the angular momentum vector about the center of gravity. Equations (1.16) and (1.17) need to be referred to the rotating aircraft body-system.

If $\overline{\omega}$ is the angular velocity vector of the body axis system with respect to the inertial coordinates system, the rules for transforming vector derivatives into the rotating aircraft body system give the following equations:

$$\overline{F} = \frac{d}{dt}\left(m\overline{V}\right) + \overline{\omega} \times \left(m\overline{V}\right) \tag{1.18}$$

$$\overline{M} = \frac{d}{dt}\left(\overline{H}\right) + \overline{\omega} \times \overline{H} \tag{1.19}$$

The angular momentum is further given by:

$$\overline{H} = \begin{bmatrix} I_x & -I_{xy} & -I_{xz} \\ -I_{xy} & I_y & -I_{yz} \\ -I_{xz} & -I_{yz} & I_z \end{bmatrix} \overline{\omega} \tag{1.20}$$

The matrix in Equation (1.20) is the inertia tensor expressed in the body fixed system of coordinates. The components of ω in the body axis system of coordinates are p, q and r. The components of V in the body axis system of coordinates are u, v and w. The indices from the CG components of velocity u_{CG}, v_{CG} and w_{CG} are dropped, for brevity.

For aircraft stability and control applications the time derivatives of the mass and of the inertia tensor are neglected. To avoid larger changes in mass and CG location the helicopter was refueled after a total flying time of about one hour.

Equations (1.18) and (1.19) can further be written in the following scalar form:

- Forces equations:

$$\begin{aligned} F_x &= m\left(\dot{u} - rv + qw\right) \\ F_y &= m\left(\dot{v} + ru - pw\right) \\ F_z &= m\left(\dot{w} + pv - qu\right) \end{aligned} \tag{1.21}$$

- Moments equations:

$$\begin{aligned} L &= \dot{p}I_x - \dot{q}I_{xy} - \dot{r}I_{xz} + qr(I_z - I_y) + (r^2 - q^2)I_{yz} - pqI_{xz} + rpI_{xy} \\ M &= -\dot{p}I_{xy} + \dot{q}I_y - \dot{r}I_{yz} + rp(I_x - I_z) + (p^2 - r^2)I_{xz} - qrI_{xy} + pqI_{yz} \\ N &= -\dot{p}I_{xz} - \dot{q}I_{yz} + \dot{r}I_z + pq(I_y - I_x) + (q^2 - p^2)I_{xy} - rpI_{yz} + qrI_{xz} \end{aligned} \tag{1.22}$$

where F_x, F_y and F_z are the components of the external applied forces, and L, M and N are the components of the external applied moments.

The aircraft mass distribution is considered symmetrical relative to the xz-body plane of symmetry. Hence, the moments of inertia $I_{xy} = 0$ and $I_{yz} = 0$ and the general moments of inertia expressions given by Equations (1.22) become:

$$\begin{aligned} I_x\dot{p} &= (I_y - I_z)qr + I_{zx}(\dot{r} + pq) + L \\ I_y\dot{q} &= (I_z - I_x)rp + I_{zx}(r^2 - p^2) + M \\ I_z\dot{r} &= (I_x - I_y)pq + I_{zx}(\dot{p} - qr) + N \end{aligned} \tag{1.23}$$

Expressing F_x, F_y and F_z as functions of the aerodynamic forces X, Y and Z, and the gravity force, as follows:

$$\begin{aligned} F_x &= X - mg\sin\theta \\ F_y &= Y + mg\cos\theta\sin\varphi \\ F_z &= Z + mg\cos\theta\cos\varphi \end{aligned} \tag{1.24}$$

and introducing the forces given by Equations (1.21) into Equations (1.24) gives:

$$\begin{aligned} m\dot{u} &= m(vr - wq) + X - mg\sin\theta \\ m\dot{v} &= m(wp - ur) + Y + mg\cos\theta\sin\phi \\ m\dot{w} &= m(uq - vp) + Z + mg\cos\theta\cos\phi \end{aligned} \tag{1.25}$$

The kinematic equations for Euler rates are obtained from Equation (1.1) as follows:

$$\begin{aligned} \dot{\phi} &= p + q\sin\phi\tan\theta + r\cos\phi\tan\theta \\ \dot{\theta} &= q\cos\phi - r\sin\phi \\ \dot{\psi} &= q\frac{\sin\phi}{\cos\theta} + r\frac{\cos\phi}{\cos\theta} \end{aligned} \tag{1.26}$$

Equations (1.23), (1.25) and (1.26) are nonlinear because of the gravitational and rotation related terms in the force Equations (1.25) and the appearance of products of angular rates in the moment Equations (1.23).

Using small perturbation theory, the products of angular rates are assumed to be small and therefore, can be neglected in the moment Equations (1.23). Hence, a simplified set of equations results:

$$\begin{aligned} L &= I_x \dot{p} - I_{zx} \dot{r} \\ M &= I_y \dot{q} \\ N &= I_z \dot{r} - I_{zx} \dot{p} \end{aligned} \tag{1.27}$$

Furthermore, by dividing the force Equations (1.25) by the mass, m, and multiplying the simplified moment Equations (1.27) by the inverse inertia matrix, forces and moments are presented as "specific" quantities:

- Specific forces:

$$\begin{aligned} \widetilde{X} &= X / m \\ \widetilde{Y} &= Y / m \\ \widetilde{Z} &= Z / m \end{aligned} \tag{1.28}$$

- Specific moments:

$$\begin{bmatrix} \widetilde{L} \\ \widetilde{M} \\ \widetilde{N} \end{bmatrix} = \begin{bmatrix} I_x & 0 & -I_{zx} \\ 0 & I_y & 0 \\ -I_{zx} & 0 & I_z \end{bmatrix}^{-1} \begin{bmatrix} L \\ M \\ N \end{bmatrix} \tag{1.29}$$

Then, using the specific forces (1.28) into Equations (1.25) and the specific moments (1.29) into Equations (1.23) the following two sets of equations are obtained:

- the linear accelerations:

$$\begin{aligned} \dot{u} &= \widetilde{X} + vr - wq - g\sin\theta \\ \dot{v} &= \widetilde{Y} + wp - ur + g\cos\theta\sin\phi \\ \dot{w} &= \widetilde{Z} + uq - vp + g\cos\theta\cos\phi \end{aligned} \tag{1.30}$$

- the angular accelerations:

$$\dot{p} = \widetilde{L}$$
$$\dot{q} = \widetilde{M} \tag{1.31}$$
$$\dot{r} = \widetilde{N}$$

In 6 DoF form, the motion states are usually arranged in the state vector as longitudinal (u, w, q, θ) and lateral (v, p, ϕ, r, ψ) motion subsets, as follows:

$$x = [u, w, q, \theta, v, p, \phi, r, \psi]^T \tag{1.32}$$

where u, v and w are the translational velocities, p, q and r are the angular velocities along the body-axes and ϕ, θ and ψ are the Euler angles, defining the orientation of the body axes relative to the earth.

The control vector has four components: longitudinal cyclic, δ_{lon}, lateral cyclic, δ_{lat}, tail rotor collective (pedals), δ_{ped}, and main rotor collective, δ_{col}:

$$\mathrm{u} = [\delta_{lon}, \delta_{lat}, \delta_{ped}, \delta_{col}]^T \tag{1.33}$$

In the small perturbation theory, the helicopter's behavior can be described as a perturbation ΔX from its trim position X_e, and is written under the following form:

$$X = X_e + \Delta X \tag{1.34}$$

Taylor's theorem for analytic functions implies that if the force and moment functions and all their derivatives are known at the trim point, then the behavior of that function anywhere in its analytic range can be estimated from an expansion of the function in a series about the trim point.

The forces and moments arise from aerodynamic, gravitational and control effects. The series of Taylor expansion for the aerodynamic force on x-axis, X, provides [12]:

$$X = X_e + \frac{\partial X}{\partial u}\cdot\Delta u + \frac{\partial^2 X}{\partial u^2}\frac{\Delta u^2}{2!} + \ldots + \frac{\partial X}{\partial v}\cdot\Delta v + \frac{\partial^2 X}{\partial v^2}\frac{\Delta v^2}{2!} + \ldots + \frac{\partial X}{\partial w}\cdot\Delta w + \frac{\partial^2 X}{\partial w^2}\frac{\Delta w^2}{2!} + \ldots +$$
$$+ \frac{\partial X}{\partial p}\cdot\Delta p + \frac{\partial^2 X}{\partial p^2}\frac{\Delta p^2}{2!} + \ldots + \frac{\partial X}{\partial q}\cdot\Delta q + \frac{\partial^2 X}{\partial q^2}\frac{\Delta q^2}{2!} + \ldots + \frac{\partial X}{\partial r}\cdot\Delta r + \frac{\partial^2 X}{\partial r^2}\frac{\Delta r^2}{2!} + \ldots \tag{1.35}$$

If the perturbation notation, Δ, is dropped, hence referring to the perturbed variables by their regular characters *u, v, w*, instead of Δu, Δv, Δw, etc., and if second and higher order terms in each Taylor series are assumed to be negligible then one can write:

$$X = X_e + \frac{\partial X}{\partial u}\cdot u + \frac{\partial X}{\partial v}\cdot v + \frac{\partial X}{\partial w}\cdot w + \frac{\partial X}{\partial p}\cdot p + \frac{\partial X}{\partial q}\cdot q + \frac{\partial X}{\partial r}\cdot r +$$
$$+ \frac{\partial X}{\partial \delta_{lon}}\delta_{lon} + \frac{\partial X}{\partial \delta_{lat}}\delta_{lat} + \frac{\partial X}{\partial \delta_{ped}}\delta_{ped} + \frac{\partial X}{\partial \delta_{col}}\delta_{col} \tag{1.36}$$

where the last four derivatives account for the controls effects (see vector (1.33)).

The standard stability and control derivatives notation is further introduced:

$$X_u = \frac{\partial X}{\partial u};\quad X_v = \frac{\partial X}{\partial v};\quad X_w = \frac{\partial X}{\partial w};\ \ldots \tag{1.37}$$

and replacing Equations (1.37) into Equations (1.36) yields:

$$X = X_e + X_u u + X_v v + X_w w + X_p p + X_q q + X_r r + X_{lon}\delta_{lon} +$$
$$+ X_{lat}\delta_{lat} + X_{ped}\delta_{ped} + X_{col}\delta_{col} \tag{1.38}$$

Applying the same analysis to the other forces and moments acting on a helicopter yields the following set of stability derivatives:

$$\begin{bmatrix} X_u & X_v & X_w & X_p & X_q & X_r \\ Y_u & Y_v & Y_w & Y_p & Y_q & Y_r \\ Z_u & Z_v & Z_w & Z_p & Z_q & Z_r \\ L_u & L_v & L_w & L_p & L_q & L_r \\ M_u & M_v & M_w & M_p & M_q & M_r \\ N_u & N_v & N_w & N_p & N_q & N_r \end{bmatrix} \tag{1.39}$$

Based on the control vector components shown in (1.33) a second set of control derivatives is further obtained:

$$\begin{bmatrix} X_{lon} & X_{lat} & X_{ped} & X_{col} \\ Y_{lon} & Y_{lat} & Y_{ped} & Y_{col} \\ Z_{lon} & Z_{lat} & Z_{ped} & Z_{col} \\ L_{lon} & L_{lat} & L_{ped} & L_{col} \\ M_{lon} & M_{lat} & M_{ped} & M_{col} \\ N_{lon} & N_{lat} & N_{ped} & N_{col} \end{bmatrix} \tag{1.40}$$

The linearized specific aerodynamic forces and moments are written:

$$\begin{pmatrix} \tilde{X} \\ \tilde{Y} \\ \tilde{Z} \\ \tilde{L} \\ \tilde{M} \\ \tilde{N} \end{pmatrix} = \begin{pmatrix} \tilde{X}_e \\ \tilde{Y}_e \\ \tilde{Z}_e \\ \tilde{L}_e \\ \tilde{M}_e \\ \tilde{N}_e \end{pmatrix} + \begin{pmatrix} \Delta\tilde{X} \\ \Delta\tilde{Y} \\ \Delta\tilde{Z} \\ \Delta\tilde{L} \\ \Delta\tilde{M} \\ \Delta\tilde{N} \end{pmatrix} \tag{1.41}$$

where the subscript "*e*" means the initial conditions, and:

$$\begin{pmatrix} \Delta\tilde{X} \\ \Delta\tilde{Y} \\ \Delta\tilde{Z} \\ \Delta\tilde{L} \\ \Delta\tilde{M} \\ \Delta\tilde{N} \end{pmatrix} = \begin{pmatrix} \tilde{X}_u & \tilde{X}_v & \tilde{X}_w & \tilde{X}_p & \tilde{X}_q & \tilde{X}_r \\ \tilde{Y}_u & \tilde{Y}_v & \tilde{Y}_w & \tilde{Y}_p & \tilde{Y}_q & \tilde{Y}_r \\ \tilde{Z}_u & \tilde{Z}_v & \tilde{Z}_w & \tilde{Z}_p & \tilde{Z}_q & \tilde{Z}_r \\ \tilde{L}_u & \tilde{L}_v & \tilde{L}_w & \tilde{L}_p & \tilde{L}_q & \tilde{L}_r \\ \tilde{M}_u & \tilde{M}_v & \tilde{M}_w & \tilde{M}_p & \tilde{M}_q & \tilde{M}_r \\ \tilde{N}_u & \tilde{N}_v & \tilde{N}_w & \tilde{N}_p & \tilde{N}_q & \tilde{N}_r \end{pmatrix} \begin{pmatrix} u \\ v \\ w \\ p \\ q \\ r \end{pmatrix} + \begin{pmatrix} \tilde{X}_{lon} & \tilde{X}_{lat} & \tilde{X}_{ped} & \tilde{X}_{col} \\ \tilde{Y}_{lon} & \tilde{Y}_{lat} & \tilde{Y}_{ped} & \tilde{Y}_{col} \\ \tilde{Z}_{lon} & \tilde{Z}_{lat} & \tilde{Z}_{ped} & \tilde{Z}_{col} \\ \tilde{L}_{lon} & \tilde{L}_{lat} & \tilde{L}_{ped} & \tilde{L}_{col} \\ \tilde{M}_{lon} & \tilde{M}_{lat} & \tilde{M}_{ped} & \tilde{M}_{col} \\ \tilde{N}_{lon} & \tilde{N}_{lat} & \tilde{N}_{ped} & \tilde{N}_{col} \end{pmatrix} \begin{pmatrix} \delta_{lon} \\ \delta_{lat} \\ \delta_{ped} \\ \delta_{col} \end{pmatrix} \tag{1.42}$$

As the aerodynamic forces are the only external forces in Equation (1.41), it is their effect that will be measured by the accelerometers. Therefore, the following is valid:

$$\begin{pmatrix} \tilde{X} \\ \tilde{Y} \\ \tilde{Z} \end{pmatrix} = \begin{pmatrix} a_x \\ a_y \\ a_z \end{pmatrix} \tag{1.43}$$

According to (1.41) the matrix Equation (1.43) can be decomposed to give:

$$\begin{pmatrix} \widetilde{X} \\ \widetilde{Y} \\ \widetilde{Z} \end{pmatrix} = \begin{pmatrix} \widetilde{X}_e \\ \widetilde{Y}_e \\ \widetilde{Z}_e \end{pmatrix} + \begin{pmatrix} \Delta\widetilde{X} \\ \Delta\widetilde{Y} \\ \Delta\widetilde{Z} \end{pmatrix} = \begin{pmatrix} a_{xe} \\ a_{ye} \\ a_{ze} \end{pmatrix} + \begin{pmatrix} \Delta a_x \\ \Delta a_y \\ \Delta a_z \end{pmatrix} \tag{1.44}$$

The remaining non-linear terms in Equation (1.44) can be approximated assuming:

- Small values of the angular speeds (p, q, and r),
- Small variations of the Euler angles ϕ and θ,
- Small variations of the translational speeds (u, v and w).

This leads to the linearized equations of the translational accelerations:

$$\begin{pmatrix} \dot{u} \\ \dot{v} \\ \dot{w} \end{pmatrix} = \begin{pmatrix} a_{xe} \\ a_{ye} \\ a_{ze} \end{pmatrix} + \begin{pmatrix} \Delta a_x \\ \Delta a_y \\ \Delta a_z \end{pmatrix} + g \begin{pmatrix} -\sin\theta_e - \Delta\theta\cos\theta_e \\ \Delta\phi\cos\theta_e \\ \cos\theta_e - \Delta\theta\sin\theta_e \end{pmatrix} + \begin{pmatrix} -w_e q + v_e r \\ -u_e r + w_e p \\ -v_e p + u_e q \end{pmatrix} \tag{1.45}$$

The linearized equations of motion for the full 6 DoF, describing the perturbed motion about a general trim condition can be written as:

$$\dot{x}(t) = Ax(t) + Bu(t) \tag{1.46}$$

In fully expanded form [13], the stability and control matrices can be written as shown in matrix Equations (1.47) and (1.48). The stability matrix A is written as follows:

$$A = \begin{bmatrix} A_{11} & A_{12} \\ A_{21} & A_{22} \end{bmatrix} \tag{1.47}$$

where the diagonal submatrix A_{11} gives the elements of the longitudinal equations of motion:

$$A_{11} = \begin{bmatrix} \widetilde{X}_u & \widetilde{X}_w - q_e & \widetilde{X}_q - w_e & -g\cos\theta_e \\ \widetilde{Z}_u + q_e & \widetilde{Z}_w & \widetilde{Z}_q + u_e & -g\cos\phi_e\sin\theta_e \\ \widetilde{M}_u & \widetilde{M}_w & \widetilde{M}_q & 0 \\ 0 & 0 & \cos\phi_e & 0 \end{bmatrix} \tag{1.47.a}$$

while the elements of the lateral/directional equations of motion form the diagonal submatrix A_{22}:

$$A_{22}=\begin{bmatrix} \tilde{Y}_v & \tilde{Y}_p+w_e & g\cos\phi_e\cos\theta_e & \tilde{Y}_r-u_e \\ \tilde{L}_v & \tilde{L}_p+k_1q_e & 0 & \tilde{L}_r-k_2q_e \\ 0 & 1 & 0 & \cos\phi_e\tan\theta_e \\ \tilde{N}_v & \tilde{N}_p-k_3q_e & 0 & \tilde{N}_r-k_1q_e \end{bmatrix} \tag{1.47.b}$$

The other two submatrices, A_{12} and A_{21} represent the longitudinal/lateral coupling between the primary diagonal submatrices A_{11} and A_{22}:

$$A_{12}=\begin{bmatrix} \tilde{X}_v+r_e & \tilde{X}_p & 0 & \tilde{X}_r+v_e \\ \tilde{Z}_v-p_e & \tilde{Z}_p-v_e & -g\sin\phi_e\cos\theta_e & \tilde{Z}_r \\ \tilde{M}_v & \tilde{M}_p-2p_ek_4-r_ek_5 & 0 & \tilde{M}_r+2r_ek_4-p_ek_5 \\ 0 & 0 & 0 & -\sin\phi_e \end{bmatrix} \tag{1.47.c}$$

and

$$A_{21}=\begin{bmatrix} \tilde{Y}_u-r_e & \tilde{Y}_w+p_e & \tilde{Y}_q & -g\sin\phi_e\sin\theta_e \\ \tilde{L}_u & \tilde{L}_w & \tilde{L}_q+k_1p_e-k_2r_e & 0 \\ 0 & 0 & \sin\phi_e\tan\theta_e & 0 \\ \tilde{N}_u & \tilde{N}_w & \tilde{N}_q-k_1r_e-k_3p_e & 0 \end{bmatrix} \tag{1.47.d}$$

The control matrix is written as follows:

$$B=\begin{bmatrix} \tilde{X}_{lon} & \tilde{X}_{lat} & \tilde{X}_{ped} & \tilde{X}_{col} \\ \tilde{Z}_{lon} & \tilde{Z}_{lat} & \tilde{Z}_{ped} & \tilde{Z}_{col} \\ \tilde{M}_{lon} & \tilde{M}_{lat} & \tilde{M}_{ped} & \tilde{M}_{col} \\ 0 & 0 & 0 & 0 \\ \tilde{Y}_{lon} & \tilde{Y}_{lat} & \tilde{Y}_{ped} & \tilde{Y}_{col} \\ \tilde{L}_{lon} & \tilde{L}_{lat} & \tilde{L}_{ped} & \tilde{L}_{col} \\ 0 & 0 & 0 & 0 \\ \tilde{N}_{lon} & \tilde{N}_{lat} & \tilde{N}_{ped} & \tilde{N}_{col} \end{bmatrix} \tag{1.48}$$

Using Equations (1.28) and (1.29), the derivatives are written in the following semi-normalized form [14]:

$$\tilde{X}_{\_}=\frac{X_{\_}}{m}\ ;\quad \tilde{Y}_{\_}=\frac{Y_{\_}}{m}\ ;\quad \tilde{Z}_{\_}=\frac{Z_{\_}}{m}; \tag{1.49}$$

and: $$\tilde{L}_{\_}=\frac{I_z}{I_zI_x-I_{zx}^2}L_{\_}+\frac{I_{zx}}{I_zI_x-I_{zx}^2}N_{\_} \tag{1.50.a}$$

$$\tilde{M}_{\_} = \frac{M_{\_}}{I_y} \tag{1.50.b}$$

$$\tilde{N}_{\_} = \frac{I_{zx}}{I_z I_x - I_{zx}^2} L_{\_} + \frac{I_x}{I_z I_x - I_{zx}^2} N_{\_} \tag{1.50.c}$$

where the underscore "_" could be any of the indexes *u, v, w, p, q, r* .

The constants k_1 to k_5 in the stability matrix (1.47) are given by the following expressions involving the moment of inertia terms:

$$k_1 = \frac{I_{zx}\left(I_z + I_x - I_y\right)}{I_x I_z - I_{zx}^2} \; ; \; k_2 = \frac{I_z\left(I_z - I_y\right) + I_{zx}^2}{I_x I_z - I_{zx}^2} \; ; \; k_3 = \frac{I_x\left(I_y - I_x\right) - I_{zx}^2}{I_x I_z - I_{zx}^2} \; ;$$

$$k_4 = \frac{I_{zx}}{I_y} ; \; k_5 = \frac{I_x - I_z}{I_y} \tag{1.51}$$

In addition to the linearized aerodynamic forces and moments, the matrix Equation (1.47) contains perturbation inertial, gravitational and kinematic effects linearized about the trim condition defined by $u_e, v_e, w_e, p_e, q_e, r_e, \phi_e, \theta_e$. In the matrix Equation (1.47), the heading angle ψ has been omitted, as the direction of flight in the horizontal plane has no effect on the aerodynamic forces *X*, *Y* and *Z* and moments *L*, *M* and *N*.

In matrix form, the model for the observation equations can be written as follows:

$$z(t_i) = C\,x(t_i) + D\,u(t_i) + b_z \tag{1.53}$$

where:

z = the measurement vector, $\left[u_m, v_m, w_m, p_m, q_m, r_m, a_{xm}, a_{ym}, a_{zm}\right]^T$, at time t_i .

b_z = the matrix of biases.

The observation equation is in time discrete form, representing the sampled nature of the tests and contains the matrices *C* and *D* which relate the observed variables to the state and control variables. In an expanded form, the *C* and *D* matrix are written as in (1.54).

$$C=\begin{bmatrix} 1 & 0 & 0 & 0 & 0 & 0 & 0 & 0 \\ 0 & 0 & 0 & 0 & 1 & 0 & 0 & 0 \\ 0 & 1 & 0 & 0 & 0 & 0 & 0 & 0 \\ 0 & 0 & 0 & 0 & 0 & 1 & 0 & 0 \\ 0 & 0 & 1 & 0 & 0 & 0 & 0 & 0 \\ 0 & 0 & 0 & 0 & 0 & 0 & 0 & 1 \\ \tilde{X}_u & \tilde{X}_w & \tilde{X}_q & 0 & \tilde{X}_v & \tilde{X}_p & 0 & \tilde{X}_r \\ \tilde{Y}_u & \tilde{Y}_w & \tilde{Y}_q & 0 & \tilde{Y}_v & \tilde{Y}_p & 0 & \tilde{Y}_r \\ \tilde{Z}_u & \tilde{Z}_w & \tilde{Z}_q & 0 & \tilde{Z}_v & \tilde{Z}_p & 0 & \tilde{Z}_r \end{bmatrix}; D=\begin{bmatrix} 0 & 0 & 0 & 0 \\ 0 & 0 & 0 & 0 \\ 0 & 0 & 0 & 0 \\ 0 & 0 & 0 & 0 \\ 0 & 0 & 0 & 0 \\ 0 & 0 & 0 & 0 \\ \tilde{X}_{lon} & \tilde{X}_{lat} & \tilde{X}_{ped} & \tilde{X}_{col} \\ \tilde{Y}_{lon} & \tilde{Y}_{lat} & \tilde{Y}_{ped} & \tilde{Y}_{col} \\ \tilde{Z}_{lon} & \tilde{Z}_{lat} & \tilde{Z}_{ped} & \tilde{Z}_{col} \end{bmatrix} \quad (1.54)$$

Most of the stability and control derivatives have acquired a physical descriptor based on their effect on the stability and control characteristics of a typical helicopter, as presented in Table III [15].

Table III

The most commonly used stability and control derivatives

Derivative	Descriptor	Derivative	Descriptor
X_u	Drag damping	L_p	Roll damping
Y_v	Side force	M_q	Pitch damping
Z_w	Heave damping	N_r	Yaw damping
L_v	Lateral static stability	L_{lat}	Roll control power
M_u	Speed stability	M_{lon}	Pitch control power
M_w	Angle of attack stability	N_{ped}	Yaw control power
N_v	Directional static stability	Z_{col}	Heave control power
L_{ped}	Tail rotor roll	Y_{ped}	Tail rotor drift
M_{col}	Pitch change with power	N_{col}	Torque reaction

CHAPTER 2

METHODS OF DATA ANALYSIS

2.1 General state and observation equations

It is assumed that the aircraft is modeled by a set of dynamic equations in state-space form, containing unknown parameters. The general linearized dynamic equations governing the system, with continuous time t as the independent variable together with measurements at N discrete time points t_i, can be written in continuous-discrete form as follows [16]:

$$\begin{aligned} \dot{x}(t) &= Ax(t) + Bu(t) + Fn(t) + b_x \\ z_i &= Cx_i + Du_i + G\eta_i + b_z, \quad i = 1,2,... \\ x(t_0) &= x_0 \end{aligned} \tag{2.1}$$

where

x = the state vector, $[u, w, q, \theta, v, p, \phi, r]^T$,

x_0 = the initial state vector, at $t = 0$,

u = the control input vector, $[\delta_{lon}, \delta_{lat}, \delta_{ped}, \delta_{col}]^T$,

z = the measurement vector, $[u_m, v_m, w_m, p_m, q_m, r_m, a_{xm}, a_{ym}, a_{zm}]^T$, at time t_i.

The matrices A, B, C and D contain the unknown parameters representing the stability and control derivatives and b_x and b_z are the bias terms accounting for nonzero initial conditions, the gravity and rotation related terms in the force equation and possible systematic errors in the measurements of the output and control variables. The F matrix represents the square root of the state noise spectral density and the G matrix represents the square root of the measurement noise covariance matrix.

The state noise $n(t)$ is assumed to be zero-mean Gaussian noise with an identity spectral density. The measurement noise vector η_i, is also assumed to be a sequence of independent Gaussian random variables with zero mean and identity covariance. It is further assumed that the process noise and the measurement noise are independent.

The nature of the noise is assumed to be Gaussian and white. While the "Gaussian" property describes the probability distribution function of the noise intensity at various time points in a given sequence of data, the "white" nature of the noise describes the correlation of the noise across the time points. White noise characterizes a random process whose autocorrelation with time is zero except when the time difference is zero, thus a truly white noise is unpredictable or truly random.

2.2 Time-domain identification methods

The various parameter estimation methods can be broadly classified into three categories: a) Equation Error; b) Output Error; and c) Filter Error methods [11]. Choice of a particular method is generally dictated by the model formulation and assumptions made regarding the measurement and process noise, both of which are unavoidable in practical cases.

In the Equation Error method, the measurements are considered error free and the present state noise is assumed to be random with simple statistical properties. If the state noise is present, but measurement noise is neglected, then the standard analysis results in the regression algorithm [6].

The Output Error method does not account for any process noise and is based on the assumption that the noise in the observation equation consists of a zero-mean sequence of independent random variables with a Gaussian distribution and identity covariance.

The Filter Error method is the most general stochastic approach to aircraft parameter estimation, which accounts for both process and measurement noise [17].

There are numerous codes available to implement these methods. The NRC MMLE3 program uses the Maximum Likelihood (ML) technique for parameter identification.

The original MMLE3 program developed by NASA and destined for fixed-wing aircraft applications, was modified by NRC engineers to allow the extraction of rotorcraft stability and control derivatives [18]. Original versions of MMLE3 program use a 3 DoF model with two decoupled matrices (longitudinal and lateral-directional sets) to represent the aircraft dynamic model. The equations used in the fixed-wing MMLE3 program were derived from the nonlinear aircraft equations of motion. To divide the equations into longitudinal and lateral-directional sets, symmetry about the xz-plane has been assumed and small angle approximations have been used for the sideslip angle β.

The NRC MMLE3 program used for the extraction of the Bell 427 stability and control derivatives differs from the fixed-wing MMLE3 in certain details. Its major difference is that it uses a 6 DoF linear coupled mathematical model instead of the two decoupled nonlinear equation set destined for fixed-wing use. No small angle approximations are used in any of the equations of motion. Also, because of the special characteristics of helicopter flight dynamics, all cross-coupling terms are included within the coupled 6 DoF state equations of motion. However, no rotor dynamics are included.

The MMLE3 algorithm can handle both measurement and process noise but, for the Bell 427 Parameter Estimation program, state noise is assumed to be zero based on the fact that data was recorded during calm air flight conditions. The analysis results in the Output Error method and its objective is to adjust the values for the unknown parameters in the model, to obtain the best possible fit between the measured data and the calculated model response [19]. While all unknown parameters are collected in a vector ξ, the

Maximum Likelihood estimate of ξ is obtained by minimizing the negative Log-Likelihood Function given by the following equation (see Appendix 2 for MMLE theory) [20]:

$$LLF(\xi) = \frac{1}{2}\sum_{i=1}^{N} \tilde{z}_i^T \left(GG^T\right)^{-1} \tilde{z}_i + \frac{N}{2}\log\left|GG^T\right| + \frac{Nm}{2}\log 2\pi \tag{2.2}$$

where the error , $\tilde{z}_i = z_i - \hat{z}_i$, is computed from the estimate $\hat{z}$, which is produced by a direct simulation of the model response, and the product GG^T is the measurement noise covariance matrix $GG^T = E\left\{\tilde{z}_i \tilde{z}_i^T\right\}$ (see Appendix 1 for the definitions of Covariance and Expectation).

The ML parameter estimate is obtained by choosing the value of ξ which minimizes the Maximum Likelihood cost function:

$$J_{ML}(\xi) = \frac{1}{2}\sum_{i=1}^{N} \tilde{z}_i^T \left(GG^T\right)^{-1} \tilde{z}_i \tag{2.3}$$

The set of parameter values that minimizes the Maximum Likelihood cost function has to be found by a search method. The most widespread method to minimize the cost function in Equation (2.3) is the Newton-Raphson algorithm (see Appendix 3) [21].

The Maximum Likelihood estimator also provides a measure of the reliability of each estimate. The Newton-Raphson algorithm yields the Hessian matrix. Three key metrics of parameter accuracy and correlation are calculated from the Hessian matrix [22]:

a. Parameter insensitivity– a direct measure of the insensitivity of the cost function to changes in individual parameters, taking into account the correlation with the remaining parameters.
b. Cramer-Rao bound– an estimate of the minimum achievable standard deviation in the parameter estimates and a reflector of high parameter insensitivity and/or parameter correlation.

c. Confidence ellipsoid– a multi-variable measure of parameter correlation (the conventional two-dimensional correlation matrix is not reliable when multiple correlations exist).

The model structure is reduced to a minimum set of parameters by sequentially dropping the most insignificant parameters and reconverging the remaining model parameters to minimize the fit error. This process continues until the overall cost function increases significantly with the elimination of the next parameter. The choice of which parameter to drop is based on calculations of parameter insensitivities, Cramer-Rao bounds, and confidence ellipsoid each time the model is reconverged. Using these three metrics, the parameters that are determined to be insignificant or highly correlated to other parameters may be systematically deleted (or fixed at a priori values), resulting in a final model structure which consists of a smaller number of significant parameters.

Insensitive parameters are removed first until a minimum number of parameters with insensitivity values exceeding a target value of 10% of their parameter values remain. Excessively correlated parameters are then removed until a minimum number of parameters with Cramer-Rao bounds greater than 20% of their parameter values remain. This approach accurately and reliably minimizes the model structure.

The ML technique is an iterative procedure. The main steps in the procedure are:

a. choose of suitable initial values for the elements of ξ,
b. determination of the measurement noise covariance matrix,
c. calculation of the cost function value,
d. update the values of the unknown parameters,
e. calculation of the time history response of the updated model,
f. iterate on step b) and check for convergence.

This procedure is repeated until the change in the cost function is smaller than a prescribed value. The change in the cost function also indicates convergence of the estimation.

To start the technique, a first guess for the unknowns, the apriori values, is needed. They should be as close as possible to the "true" values to improve the convergence and to avoid that the estimation ends up in a local minimum. A set of validated stability and control derivatives from a different source or even from a different helicopter model could be selected and used to initiate the MMLE3 iteration process.

2.2.1 Time-domain identification results

There are 36 stability derivatives and 24 control derivatives in the standard 6 DoF model (Matrices (1.47) and (1.48)). With the MMLE3 program it was possible to evaluate simultaneously four test runs, one for each control input, i.e. longitudinal, lateral, pedal and collective control. The concatenated runs should have the same initial flight test conditions; therefore, the initial conditions were fixed at the mean value of the first data points (1 second). Offsets in the controls and measurements were taken into account by estimating bias terms for each individual maneuver. These biases were used for the force and moment state equations as well as for the speed and linear acceleration measurement equation.

The helicopter's real response is delayed as a result of high order dynamics (e.g. the rotor and the hydraulic actuators). Additional high order dynamics are further introduced into the data as a result of instrumentation system response and filters. An accurate estimate of these effective time delays is important for obtaining physically reasonable values for primary angular damping derivatives [3].

To approximate these effects, equivalent time delays for the controls were used. These time delays were determined by a direct observation of the time histories between each input and the on-axis response (accelerations and rates) and by using a cross-correlation technique. Thus, time delays were added to the control inputs until a maximum correlation coefficient was found between inputs and corresponding rates/accelerations. The equivalent time delays values were used to time shift the measured control variables before the identification was started.

Among 179 runs for parameter identification purposes, only a limited number of flight maneuvers (4 cases) will be presented. Table IV depicts the chosen tests.

Table IV

List of considered runs for Bell 427 helicopter

Test (CG position)	Control input	Initial displacement	Record length [s]	Airspeed/ Flight condition	Altitude
LHA37 (heavy aft)	Longitudinal	Forward	20	70 kt Level flight	3000 ft
	Lateral	Left	25		
	Pedals	Left	20		
	Collective	Down	20		
C10LF69 (light fwd)	Longitudinal	Aft	17	90 kt Climb at 1000 ft/min	6000 ft
	Lateral	Right	17		
	Pedals	Right	21		
	Collective	Down	20		
D10LA310 (light aft)	Longitudinal	Forward	14	100 kt Descent at 1000 ft/min	3000 ft
	Lateral	Right	12		
	Pedals	Right	15		
	Collective	Down	14		
AHF68 (heavy fwd)	Longitudinal	Forward	15	80 kt Autorotation test	6000 ft
	Lateral	Right	14		
	Pedals	Right	14		
	Collective	Up	14		

The identification results generated with the MMLE3 program were processed using Matlab and are given in the format of time-histories of the measured data and the model's response and also as tables of time constants, damping ratios and undamped natural frequencies derived from the calculated eigenvalues.

Figures 9 to 12 present the time history plots of the measured data (blue lines) and the calculated response of the identified model (red dotted lines). The parameter values were intentionally omitted for confidentiality reasons.

Table V presents the mean value and the standard deviation of the differences (residuals) between the measured data and outputs of the identified model. The magnitude of this difference indicates how well the model describes the practical system.

The verification of time histories and of the statistics tables shows that:

a. the agreement of the measured data and the response of the identified model is good; the longitudinal motion is more accurately represented than the lateral-directional motion;
b. for the force equations, the fit in the linear accelerations is very good; the vertical acceleration fit is less accurate than the lateral and longitudinal acceleration fit, probably because of the low signal-to-noise ratio in some flight conditions;
c. the time history fits of the rates demonstrate that the on-axis response of the model (q/δ_{lon}, p/δ_{lat}, r/δ_{ped}) follow the flight test data closer than the off-axis response; the yaw rate fit is less accurate than the roll or pitch rate fit;
d. the differences in the speed components (especially the vertical speed, w) reflect some inaccuracies in measurement of the true airspeed, angle of attack and angle of sideslip, possibly caused by the rotor downwash and fuselage interference at the boom.

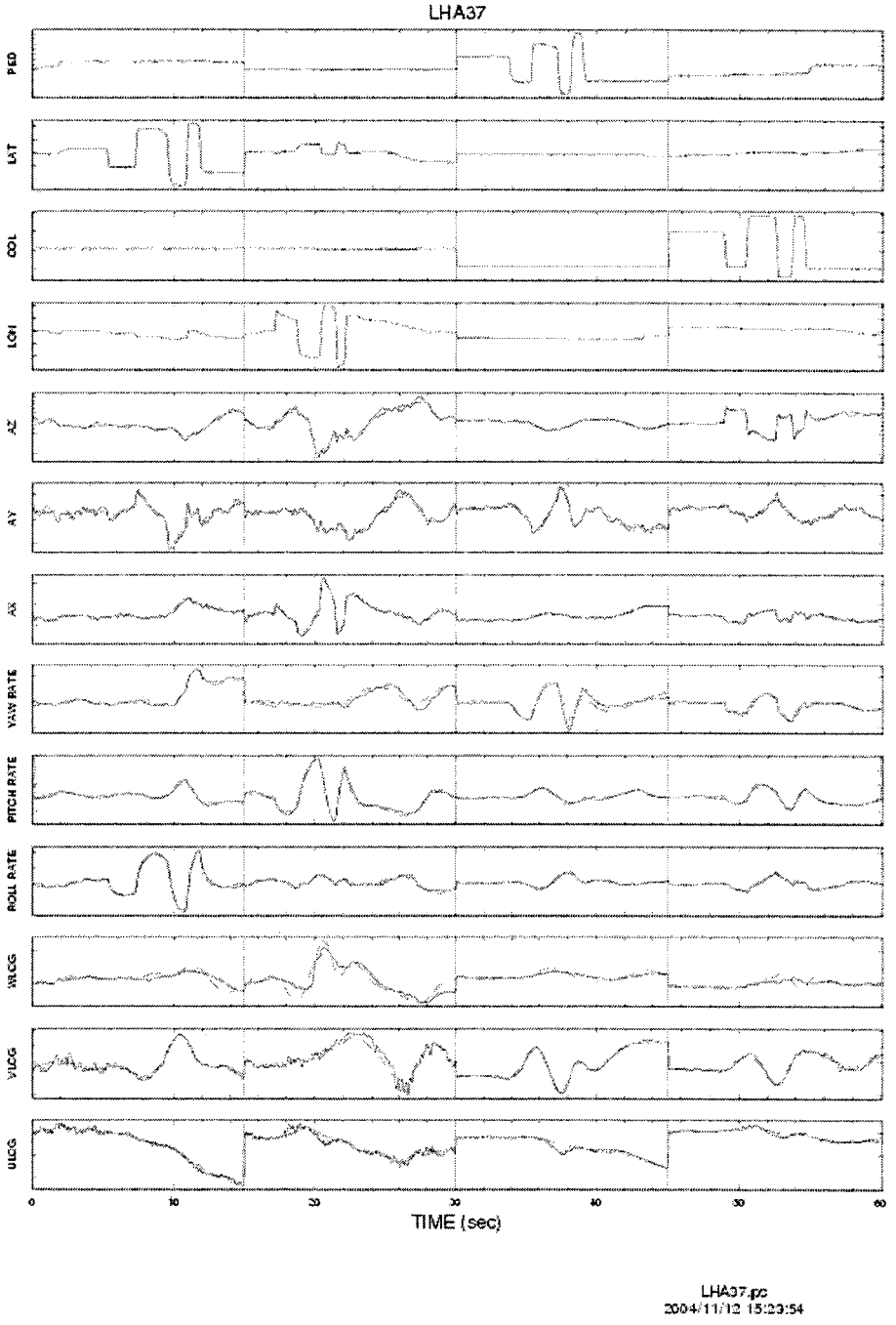

Figure 9 Time history comparison of measured data and the response of the identified model for LHA37 case

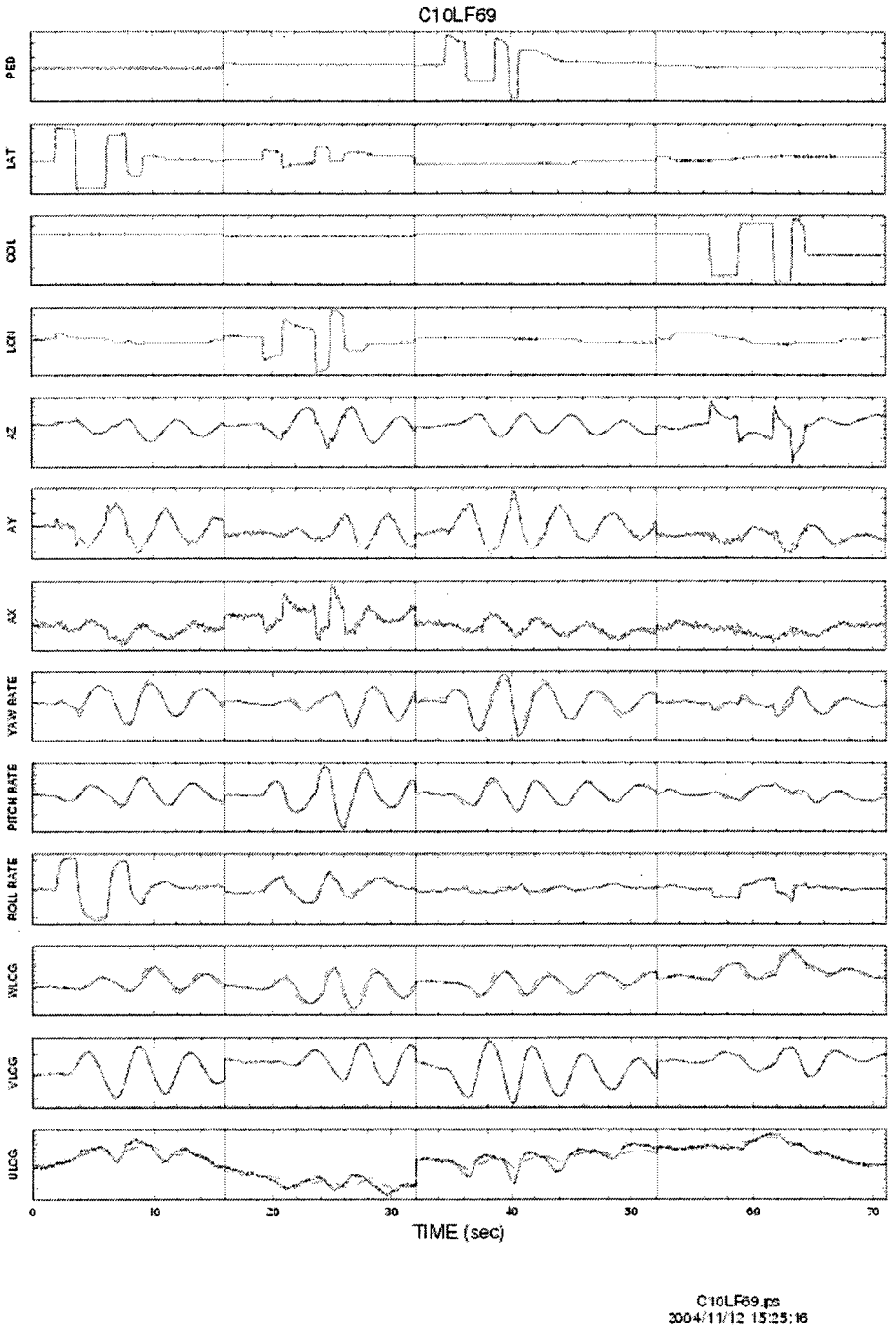

Figure 10 Time history comparison of measured data and the response of the identified model for C10LF69 case

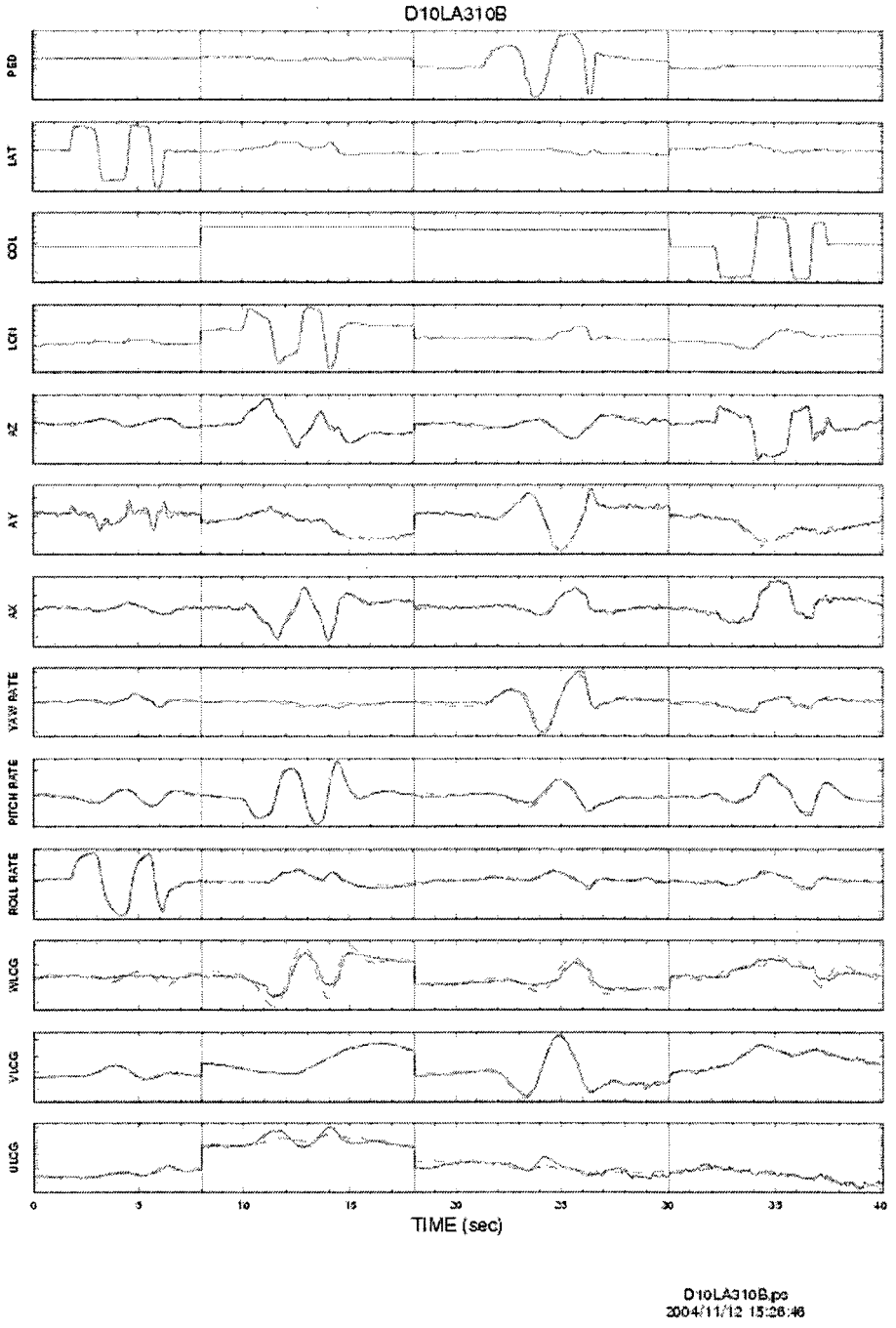

Figure 11 Time history comparison of measured data and the response of the identified model for D10LA310 case

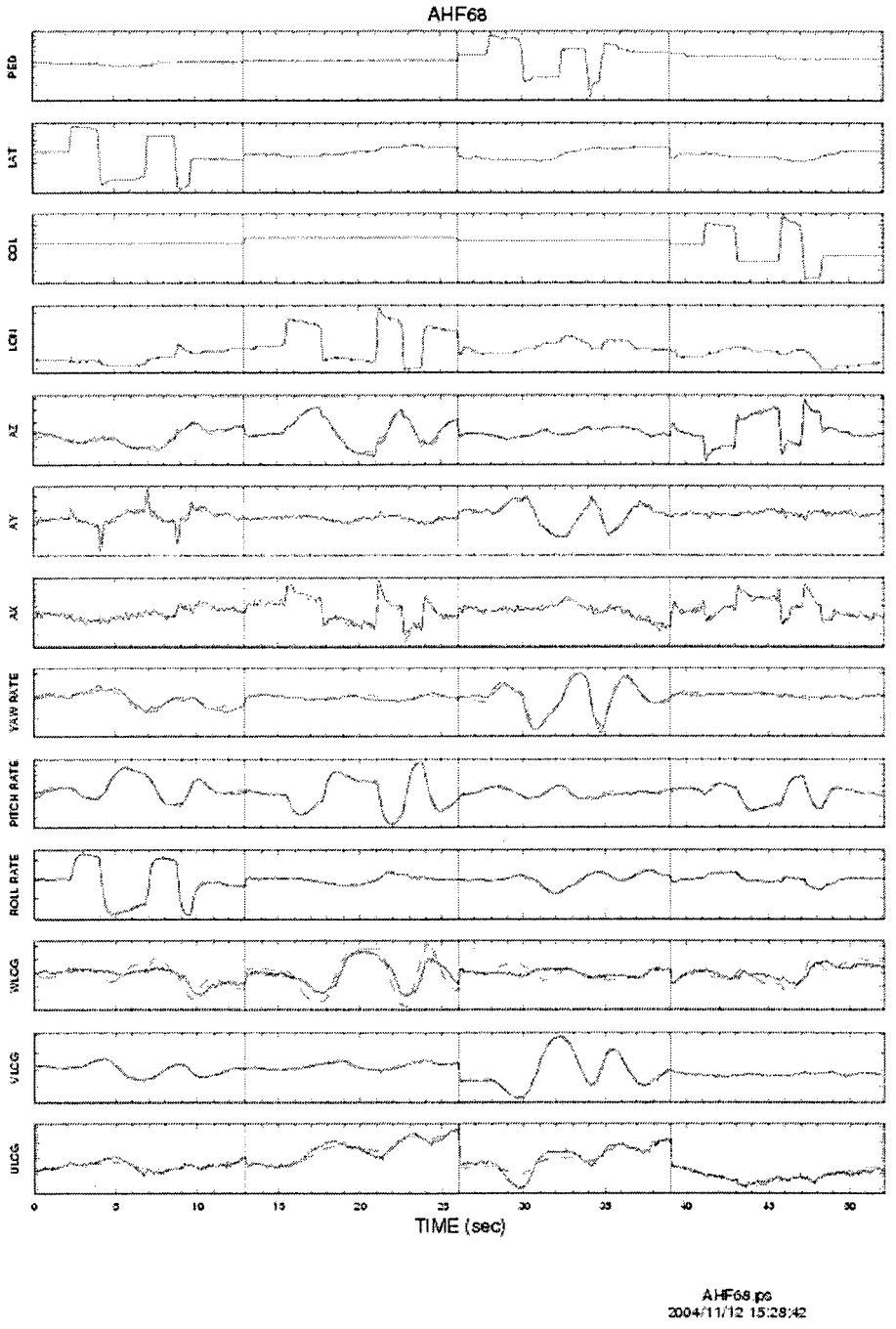

Figure12 Time history comparison of measured data and the response of the identified model for AHF68 case

Table V

The statistics of parameter residuals for each channel input

Input		Lon		Lat		Ped		Col	
Test	Residual	Mean	St. dev.	Mean	St. dev.	Mean	St. dev.	Mean	St. dev.
LHA37	ε_u	-0,0038	0,9845	+0,0079	1,6035	-0,0004	1,0577	+0,0009	0,6933
	ε_v	-0,0038	0,8711	-0,0031	1,5787	+0,0002	0,4560	-0,0004	0,5967
	ε_w	-0,0006	0,9452	-0,0005	1,9481	+0,0006	0,6458	-0,0011	0,9456
	ε_p	+0,0002	0,0114	-0,0001	0,0106	+0,0000	0,0060	+0,0000	0,0064
	ε_q	-0,0002	0,0052	+0,0002	0,0075	-0,0000	0,0039	-0,0001	0,0049
	ε_r	-0,0007	0,0072	+0,0004	0,0146	-0,0004	0,0139	+0,0000	0,0074
	ε_{ax}	+0,0009	0,0578	-0,0001	0,1092	+0,0006	0,0367	-0,0002	0,0517
	ε_{ay}	+0,0006	0,1393	-0,0007	0,1216	-0,0007	0,0832	-0,0003	0,0858
	ε_{az}	+0,0005	0,3891	-0,0001	0,7263	+0,0003	0,1425	+0,0023	0,3966
C10LF69	ε_u	-0,0016	0,8530	+0,0034	1,1243	-0,0008	1,2144	+0,0023	0,5605
	ε_v	-0,0000	0,5988	-0,0008	0,5831	-0,0003	0,6110	-0,0017	0,4758
	ε_w	+0,0001	0,5998	+0,0013	1,0267	+0,0009	0,7834	-0,0006	0,7847
	ε_p	+0,0001	0,0051	+0,0000	0,0065	+0,0000	0,0056	+0,0000	0,0058
	ε_q	+0,0001	0,0032	-0,0000	0,0048	-0,0001	0,0042	-0,0001	0,0043
	ε_r	+0,0004	0,0088	-0,0002	0,0104	-0,0005	0,0165	-0,0002	0,0103
	ε_{ax}	-0,0001	0,0432	-0,0001	0,0548	-0,0000	0,0416	+0,0001	0,0487
	ε_{ay}	-0,0006	0,1463	+0,0002	0,1235	+0,0006	0,1318	+0,0002	0,1418
	ε_{az}	-0,0021	0,1778	+0,0004	0,2104	-0,0000	0,1015	+0,0006	0,4224

Table V (cont.)

The statistics of parameter residuals for each channel input.

Input		Lon		Lat		Ped		Col	
Test	Residual	Mean	St. dev.	Mean	St. dev.	Mean	St. dev.	Mean	St. dev.
D10LA310	ε_u	+0,0018	0,5480	-0,0039	1,4137	-0,0080	1,3612	-0,0036	0,8703
	ε_v	+0,0025	0,5424	-0,0010	0,3559	-0,0050	1,2133	+0,0006	0,8807
	ε_w	+0,0036	0,8965	-0,0036	1,6392	+0,0003	0,9656	+0,0004	1,1552
	ε_p	-0,0001	0,0119	+0,0000	0,0097	+0,0001	0,0075	-0,0000	0,0086
	ε_q	+0,0001	0,0047	+0,0001	0,0039	-0,0000	0,0067	+0,0001	0,0049
	ε_r	-0,0000	0,0099	+0,0001	0,0099	+0,0004	0,0187	+0,0006	0,0128
	ε_{ax}	+0,0001	0,0411	+0,0001	0,0693	+0,0003	0,0717	+0,0004	0,1092
	ε_{ay}	-0,0017	0,3595	+0,0000	0,1322	+0,0005	0,1754	-0,0016	0,1878
	ε_{az}	-0,0042	0,2807	-0,0016	0,3387	+0,0005	0,4902	+0,0015	0,7354
AHF68	ε_u	+0,0004	0,8229	-0,0019	0,9905	+0,0042	1,7436	-0,0008	0,7772
	ε_v	-0,0017	0,5874	-0,0024	0,5861	-0,0013	0,8163	-0,0006	0,3958
	ε_w	-0,0003	0,9130	-0,0034	1,3128	-0,0006	0,7675	-0,0004	0,8183
	ε_p	+0,0001	0,0074	+0,0000	0,0051	-0,0000	0,0040	+0,0000	0,0054
	ε_q	-0,0002	0,0031	+0,0000	0,0023	-0,0001	0,0025	+0,0001	0,0026
	ε_r	-0,0003	0,0129	-0,0001	0,0072	+0,0010	0,0149	-0,0005	0,0067
	ε_{ax}	+0,0008	0,0517	-0,0002	0,0500	+0,0003	0,0446	-0,0002	0,0496
	ε_{ay}	+0,0015	0,2272	+0,0001	0,0831	-0,0006	0,1240	+0,0000	0,1153
	ε_{az}	+0,0040	0,3744	+0,0012	0,3389	+0,0016	0,1809	-0,0001	0,3966

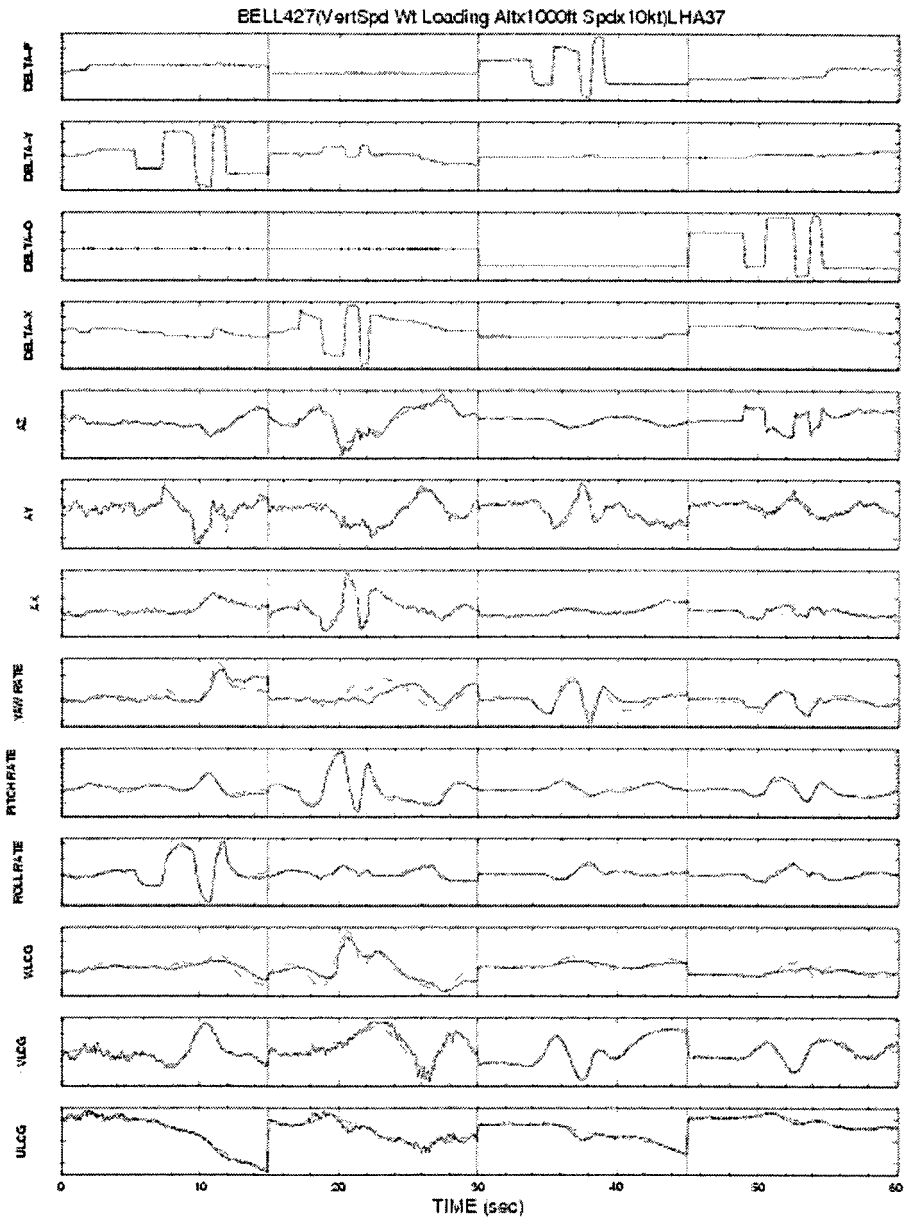

Figure 13 Verification of the identified model

2.2.2 Time-domain verification of identified models

The last step in the identification procedure is model verification. For this step, the identified state-space model is driven with flight data not used in the identification process, in order to check the model's predictive capability. The state space equations are integrated with the model stability and control parameters held constant at their identified values. For comparison, both, the model output and the measured flight test data are plotted. The agreement shown in Figure 13 of both time history plots reflects the good predicting capability of the identified model.

2.2.3 Stability analysis

Having obtained the mathematical model, it is possible now to discuss the maneuver stability of the helicopter. Stability is concerned with the behavior of the aircraft following a disturbance from trim. While static stability is determined by the initial tendency in the helicopter's motion following a perturbation, the dynamic stability is concerned with the aircraft's long-term response to such a disturbance. An aircraft is dynamically stable if, following the end of a disturbing force, it returns to its equilibrium position. Control response, on the other hand, is concerned with the response of the aircraft to a control input made by the pilot. This section examines the dynamic stability and control response of the helicopter in forward flight.

In order to analyze the dynamic stability characteristics of the helicopter it is necessary to consider the equations governing its motion. The helicopter's free motion is a linear combination of natural modes, each with an exponential character in time defined by the eigenvalues, and a distribution among the states, defined by the eigenvectors [12]. The eigenvalues are given as the solutions of the characteristic equation:

$$\det(\lambda I - A) = 0 \tag{2.4}$$

where A is the stability matrix (1.47). The matrix has been arranged so that the longitudinal equations form a submatrix in the upper-left-hand corner while the lateral-directional equations are in the lower right. The other two corners represent the coupling between the primary submatrices.

The stability of the helicopter can be discussed in terms of the stability of the individual modes, which is entirely determined by the signs of the real parts of the eigenvalues. A negative real part indicates stability, while a positive real part denotes that the helicopter is unstable.

The coefficients of the characteristic equation are nonlinear functions of the stability derivatives. Many of the coupled longitudinal/lateral derivatives are quite strong and are likely to have a major influence on the response characteristics. As far as stability is concerned however, an approximation is made such that the eigenvalues reduce into two sets: longitudinal and lateral.

The partitioning works only when there is a natural separation of the modes in the complex plane. In fact, approximations to the eigenvalues of slow modes can be estimated by assuming that in the longer term, the faster modes have reached their steady state values and can be represented by quasi-steady effects. Likewise, approximations to the fast modes can be derived by assuming that, in the short term, the slower modes do not develop enough to affect the overall motion. A second condition requires that the coupling effects between the contributing motions are small [13].

Before analyzing the dynamic modes, it is worthwhile to recall some of the most important derivatives which influence the motion of the helicopter and to present an example of their variation with speed in a level flight at 3000 ft altitude. A "best fit" polynomial of third order is used for plotting. For confidentiality reasons, the derivatives have been normalized.

2.2.3.1. The longitudinal derivatives

In the longitudinal plane, the variation of *X*-force, *Z*-force and pitching moment, *M*, with respect to forward (u) and vertical (w) velocities, pitch rate (p), longitudinal (δ_{lon}) and collective (δ_{col}) cyclic control movements are considered.

In high-speed flight the coupling derivatives are fairly insignificant and the drag damping X_u is practically linear with speed and reflects the drag on the rotor-fuselage combination. The variation with speed of the drag damping derivative, X_u is presented in Figure 14.

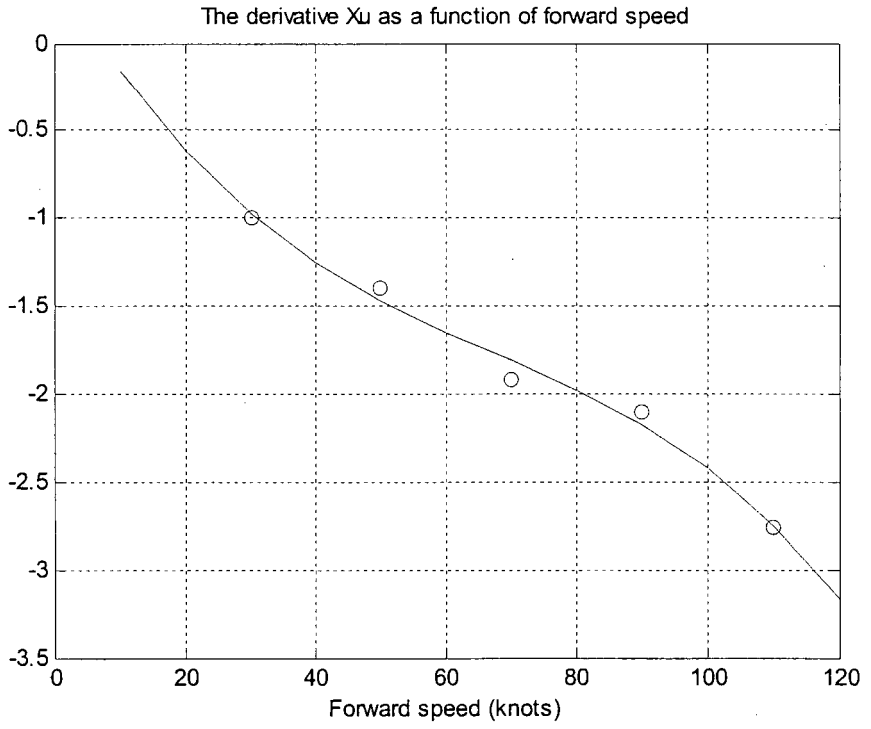

Figure 14 Variation of forward force/velocity derivative X_u with forward speed

There are stabilizing contributions to X_u from the increasing speed effects. The relative speed increases on the advancing blade with increasing speed, while the relative speed decreases on the retreating blade. Assuming that the flapping response is approximately 90° out of phase, this causes the rotor disk to flap further back, which in turn causes the thrust vector to tilt rearwards resulting in a decreased X-force. The fuselage drag increases with speed. The flap back also results in an increase of the rotor thrust and of the in-plane force. The overall effect of all these contributions is to return the aircraft to its equilibrium position.

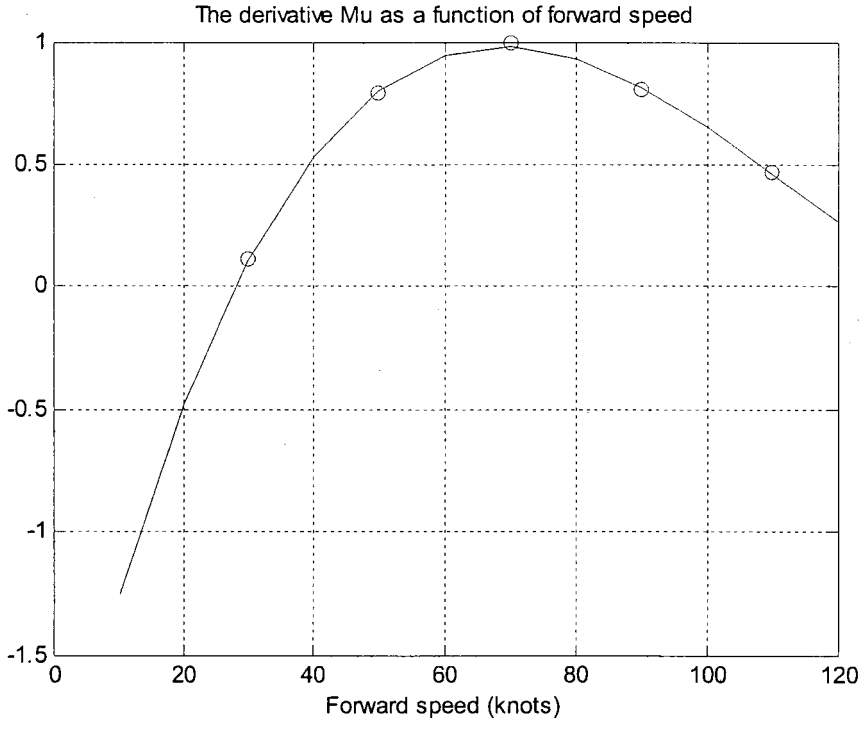

Figure 15 Variation of speed stability derivative M_u with forward speed

The speed stability derivative M_u, presented in Figure 15, has a major effect on the dynamic motion of the helicopter. An increase in forward speed causes the disk to flap back and hence tilts the trust vector rearwards causing a nose-up pitching moment and a

tendency to reduce speed, which gives a stabilizing contribution to M_u. A horizontal stabilizer also contributes significantly to the overall value of M_u with its setting angle and the downwash variations resulting from speed changes. The fuselage contribution to M_u is nearly always destabilizing; typically the aerodynamic centre of the fuselage is forward of the centre of mass. Although a positive value of M_u is necessary for static stability with respect to forward speed changes, if excessive, it will cause dynamic instability [15].

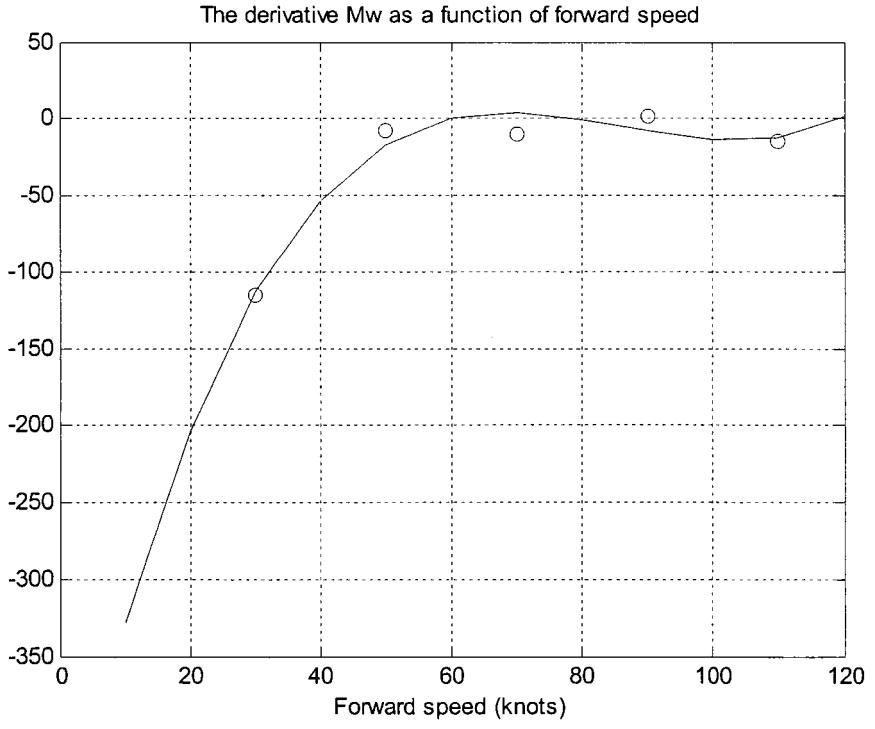

Figure 16 Variation of angle of attack stability derivative M_w with forward speed

The angle of attack stability derivative, M_w, represents the change in pitching moment about the aircraft's CG when the helicopter is subjected to a perturbation in normal velocity *w*, or effectively, incidence. When the rotor is subjected to a positive incidence change in forward flight, the advancing blade experiences a greater lift increment than

the retreating blade. The 90° phase shift in response means that the rotor flaps back and cones up and hence applies a positive pitching moment to the helicopter. Consequently, the rotor contribution to M_w is positive and destabilizing. Its value increases approximately linearly with speed. The contributions from the fuselage (destabilizing) and horizontal stabilizer (stabilizing) will also increase with airspeed but tend to cancel each other leaving the rotor as the primary contribution [13]. Figure 16 illustrates the variation of this derivative with speed.

Figure 17 Variation of heave damping derivative Z_w with forward speed

The heave damping derivative, Z_w, represents the initial acceleration following an abrupt vertical gust and is inversely proportional to rotor blade loading (defined as the aircraft mass divided by the blade area, m/A_b). An increase in the vertical speed w means that the helicopter is moving vertically downwards, and this causes an increase in

the blade angle of attack. This in turn produces an increase in blade lift as the inflow through the rotor decreases. The consequent increase in rotor thrust tends to nullify the increase in w, and Z_w is therefore always stabilizing (negative). The variation of the heave damping with speed is presented in Figure 17.

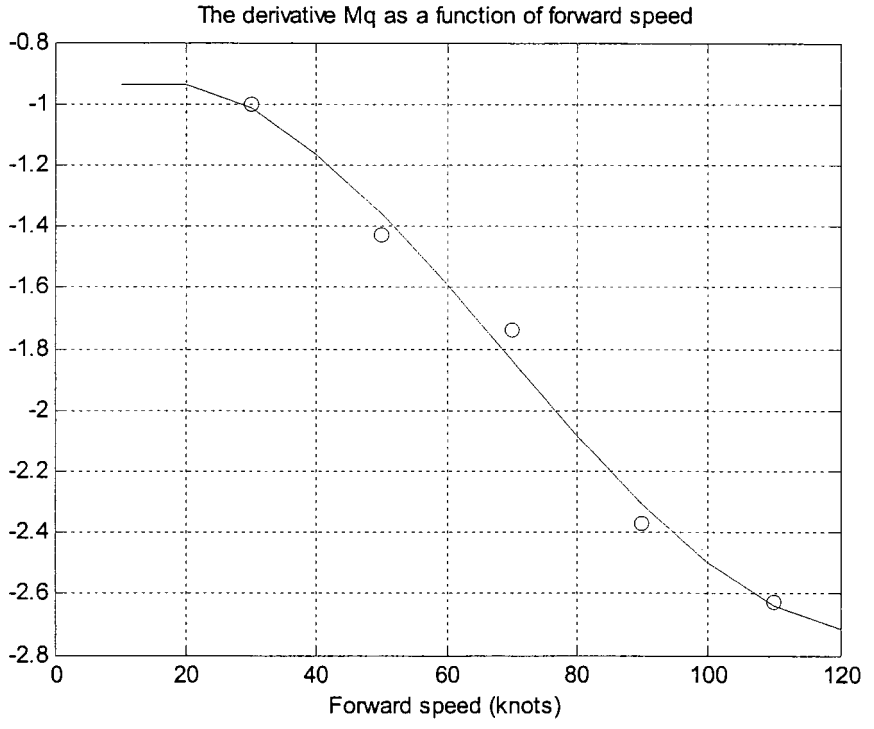

Figure 18 Variation of pitch damping M_q with forward speed

Among the pitch rate derivatives, the pitch damping M_q is worthy of note (Figure 18). It represents the change of pitching moment with changes in pitch rate. Assume that the helicopter is pitching nose-up with a constant angular velocity, q, and that the rotor is in equilibrium and pitching at the same rate. As the rotor may be regarded as a gyroscope it will be subjected to a precessing moment which would tend to tilt it starboard. However, because of the response lag, the rotor actually tilts forward, causing longitudinal forces and moments- the source of the aerodynamic damping. When the helicopter pitches

nose-up there will be a favorable nose-down moment from the main rotor due to the aerodynamic damping. Thus, the rotor contribution to M_q is stabilizing (negative).

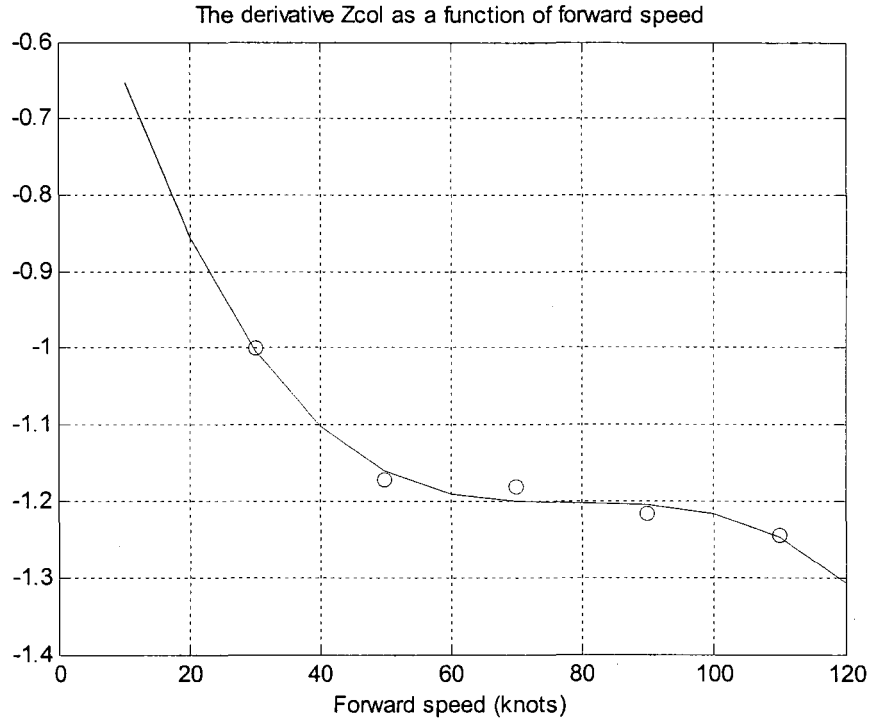

Figure 19 Variation of heave control power Z_{col} with forward speed

Movement of the collective lever and fore/aft cyclic will also affect the motion of the helicopter in the longitudinal plane. The derivative of thrust with main rotor collective Z_{col} is known as the heave control power. An increase in collective will always produce an increase in thrust (negative Z) so is always negative (Figure 19). The heave control power derivative, as with the heave damping derivative Z_w, is primarily influenced by the blade loading and tip speed [13].

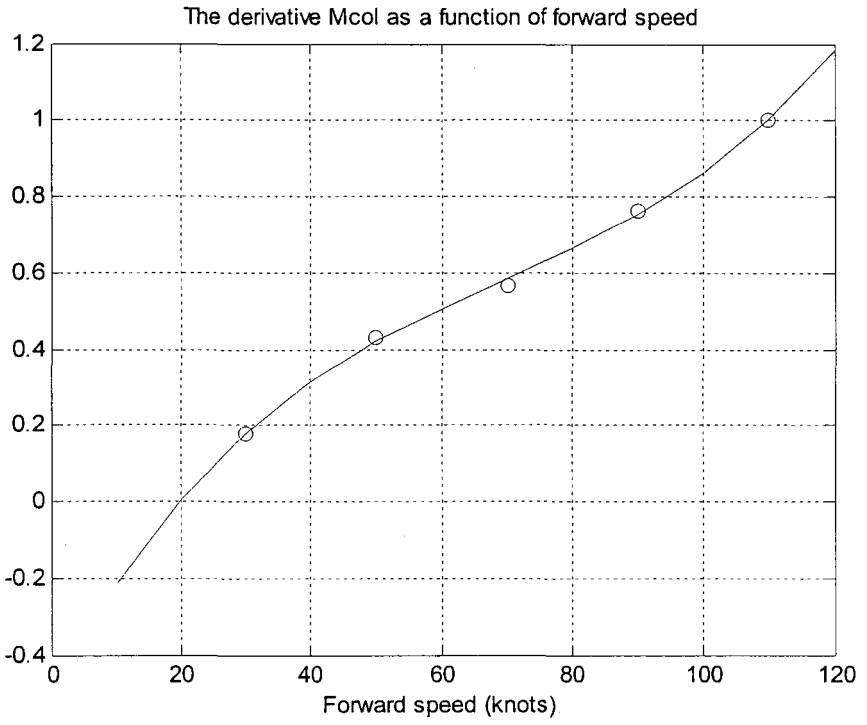

Figure 20 Variation of pitching moment due to collective M_{col} with forward speed

The pitch generated by the application of collective pitch, M_{col}, arises from two physical sources. First, the changes in rotor thrust will give rise to a moment when the thrust line is offset from the aircraft centre of mass. Second, any change in flapping caused by collective will generate a hub moment proportional to the flap angle. The aft flapping from increased collective develops from the greater increase in lift on the advancing blade than on the retreating blade in forward flight. The increased flap back and thrust combine to produce a nose-up pitching moment in forward flight so the derivative is positive. The effect grows in strength as forward speed increases, hence the proportionality with speed (Figure 20).

Any fore/aft cyclic movement will result in a change of the disk tilt, also fore/aft, and of the thrust vector. Hence, a pitching moment will be generated, nose-down for forward

stick deflection and nose-up for rearward stick. The corresponding derivative is the pitching moment due to longitudinal cyclic M_{lon}, known as the pitch control power derivative. It is always negative, as presented in Figure 21.

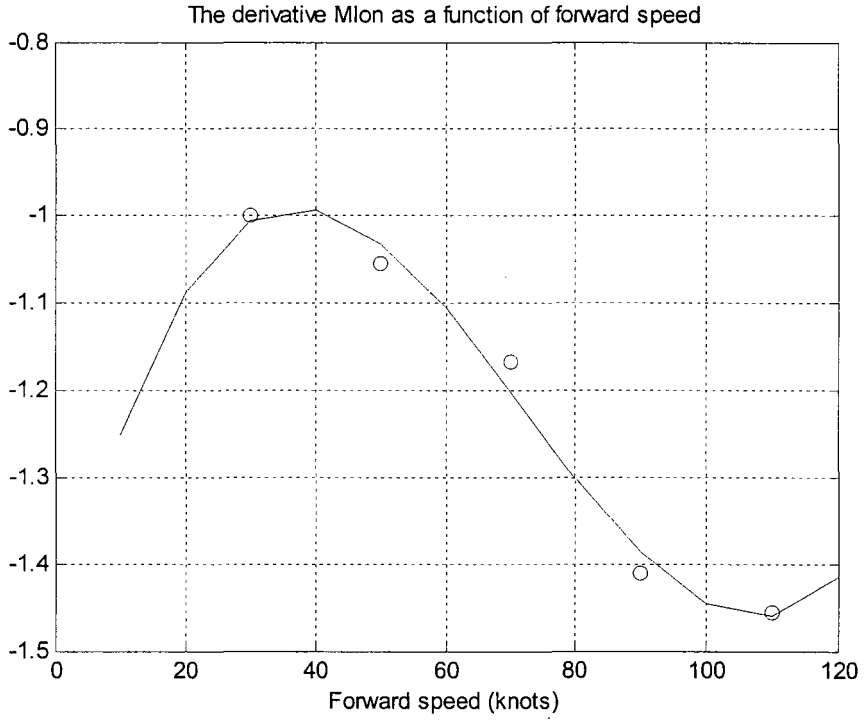

Figure 21 Variation of pitching moment due to longitudinal cyclic M_{lon} with speed

2.2.3.2 The longitudinal motion

Taking as example the **LHA37** maneuver case and expanding the determinant (2.4) produces the coupled system's 8th order characteristic equation with the general form:

$$\lambda^8 + a_7\lambda^7 + a_6\lambda^6 + a_5\lambda^5 + a_4\lambda^4 + a_3\lambda^3 + a_2\lambda^2 + a_1\lambda + a_0 = 0 \qquad (2.5)$$

The normalized roots of the polynomial (2.5), in order of decreasing damping, are:

$$-1;\ -0.421;\ -0{,}1568;\ -0{,}0619 \pm 0{,}2531i;\ -0{,}0128 \pm 0{,}0669i;\ \underline{0{,}0143} \qquad (2.6)$$

Looking at the coupled system roots, the last of them show that in this case the helicopter has an unstable mode (a subsidence). The roots in the form (2.6) give no clue to which types of motion are stable and which are unstable.

In order to gain physical understanding, the characteristic Equation (2.5) will be grouped into two forth-order sets. Thus, if only the determinant of the longitudinal subset (1.47.a) is expanded, the resultant characteristic equation for the **LHA37** test case has the general form:

$$\lambda^4 + b_3\lambda^3 + b_2\lambda^2 + b_1\lambda + b_0 = 0 \tag{2.7}$$

The characteristic Equation (2.7) can be factorized into:

$$\left(\lambda_p{}^2 + 2\zeta_p\omega_{np}\lambda + \omega_{np}\right)\left(\lambda_{sp}{}^2 + 2\zeta_{sp}\omega_{nsp}\lambda + \omega_{nsp}\right) = 0 \tag{2.8}$$

where ζ is the damping ratio and ω_n is the undamped natural frequency of the system. The subscript "*p*" denotes phugoid and "*sp*" stands for short period.

The eigenvalues of the uncoupled system (2.7) represent the classical short period and phugoid modes with the general form:

Phugoid: $$\lambda_{p_{1,2}} = -\zeta_p\omega_{np} \pm i\omega_{np}\sqrt{1-\zeta_p{}^2} \tag{2.9}$$

Short period: $$\lambda_{sp_{3,4}} = -\zeta_{sp}\omega_{nsp} \pm i\omega_{nsp}\sqrt{1-\zeta_{sp}{}^2} \tag{2.10}$$

The damping, ζ, and the natural frequency, ω_n, of the oscillatory mode are given by:

$$\zeta = \frac{-\mathrm{Re}}{\omega_n} \tag{2.11}$$

$$\omega_n = \sqrt{\mathrm{Re}^2 + \mathrm{Im}^2} \tag{2.12}$$

where Re and Im are the real and the imaginary part, respective, of the eigenvalue. The time to half amplitude of the oscillatory mode is given by:

$$t_{1/2} = \frac{\ln(2)}{|\mathrm{Re}(\lambda)|} \tag{2.13}$$

The phugoid mode is basically an exchange of potential and kinetic energy, with excursions in forward velocity and vertical velocity. The short period mode is a rapid incidence adjustment with only small changes in forward speed. This classical form of the two longitudinal modes does not always characterize helicopter motion however; the approximation breaks down for helicopters with stiff rotors [13], as it is the case for Bell 427. Table VI shows the difference between the coupled longitudinal eigenvalues and the corresponding uncoupled values for three forward speeds in level flight at 3000 ft altitude.

Table VI

The longitudinal modes of motion described by the coupled system normalized eigenvalues and the corresponding uncoupled values

Longitudinal modes		**Forward Speed**		
		30 knots	**70 knots**	**110 knots**
Phugoid	Coupled	-0,0208 ± 0,0368i	-0,0128 ± 0,0669i	-0,0608 ± 0,067i
	Uncoupled	0,0019 ± 0,0303i	-0,0022 ± 0,052i	-0,0073 ± 0,027i
Short period	Coupled	-0,2063 ± 0,2619i	-	-0,5013 ± 0,2407i
	Uncoupled	-0,2058 ± 0,3249i	-0,2932 ± 0,0682i	-
Pitch subsidence	Coupled	-	-0,422	-
	Uncoupled		-	-0,6157
Heave subsidence	Coupled	-	-0,1568	-
	Uncoupled		-	-0,3986

The strong coupling of the translational velocities with the angular velocities in both short and long period modes actually results in making invalid the assumption of weak coupling in this case. The powerful effects of the speed stability derivative, M_u, and the angle of attack stability derivative, M_w, result in strong coupling between all the degrees of freedom and the phugoid stability cannot be predicted using the uncoupled characteristic Equation (2.8).

Using the LTI Viewer graphical user interface from Matlab makes possible the visualization of the position of the eigenvalues in the complex plane (Pole-Zero Map) and meanwhile, to calculate the damping ratios and undamped natural frequencies of each mode of motion for the fully coupled system [23].

Table VII depicts the normalized time constants, damping ratios and undamped natural frequencies of the longitudinal modes for the coupled system at different forward speeds.

Table VII

Normalized damping ratios, undamped natural frequencies and time constants of the longitudinal modes for fully-coupled system

Longitudinal modes	**Forward Speed**		
	30 knots	**70 knots**	**110 knots**
Phugoid	[0,097; 0,042]	[0,039; 0,068]	[0,180; 0,090]
Short period	[0,122; 0,333]	-	[0,039; 0,554]
Pitch subsidence	-	(-2,30)	-
Heave subsidence	-	(-6,30)	-

In a short hand notation, $[\zeta;\omega_n]$ implies $(s^2 + 2\zeta\omega_n s + \omega_n{}^2)$, with ζ representing the damping ratio and ω_n being the undamped natural frequency in rad/s; $(1/T)$ implies $(s + 1/T)$, with T representing the time constant, in seconds.

In the case of helicopters, the characteristic equation yields four roots describing the longitudinal modes but at one flight condition there are two pairs of complex roots and at another condition are found two real and a pair of complex roots. The reason for this is the large variation in the values of the derivatives over the flight envelope.

2.2.3.3 The lateral/directional derivatives

For the lateral/directional motion, the variation of the side force (Y), the roll moment (L) and the yaw moment (N) with respect to the lateral speed (v), roll rate (p), yaw rate (r) and lateral cyclic control (δ_{lat}) and pedals (δ_{ped}) movements are considered.

The lateral static stability derivative, L_v, is provided by the side slipping motion that occurs subsequent to a change in bank angle. The derivative L_v must be negative for stability since if a disturbance in bank angle occurs and is followed by a sideslip to starboard, a rolling moment to port is required to restore equilibrium. The dihedral effect L_v is a measure of the helicopter's tendency to "roll wings level", therefore L_v stabilizes the spiral mode [10].

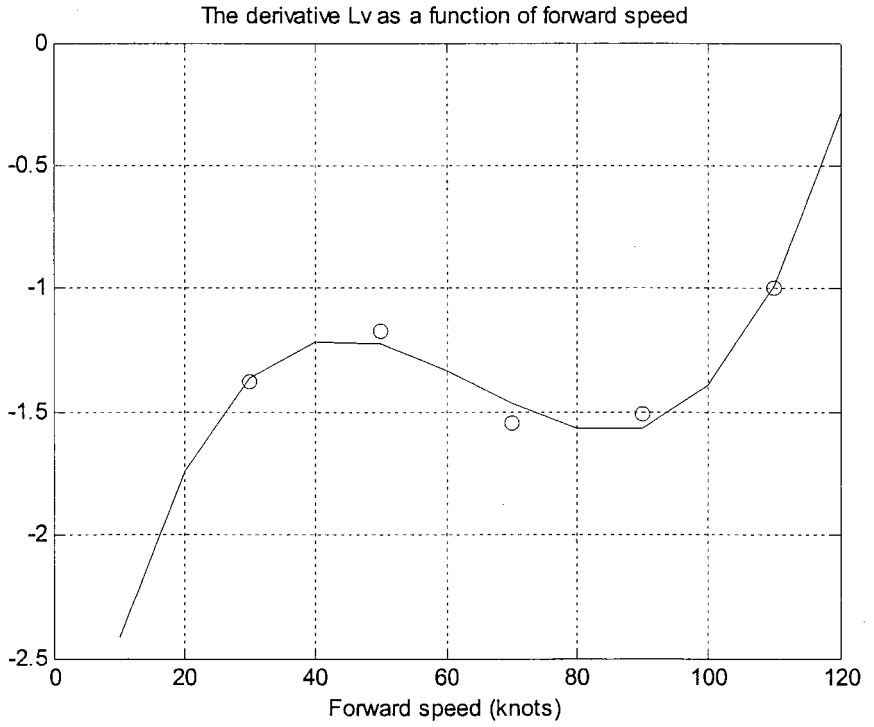

Figure 22 Variation of lateral static derivative, L_v, with forward speed

The contributions to the dihedral effect from the tail rotor, the fin and the fuselage all arise as a result of the side forces produced on these components during a sideslip. The horizontal stabilizer can also contribute to L_v. As the helicopter rolls, the down going side of the stabilizer encounters the relative airflow at an angle that effectively increases its angle of attack and hence its lift force. The up going side will experience the opposite effect and a decrease in angle of attack and lift. The imbalance provides a moment that acts to stop the roll. Figure 22 depicts its variation with forward speed.

In high-speed forward flight, the side force derivative Y_v is practically linear with speed and reflects the side force on the rotor-fuselage combination. This direct derivative is principally due to the disc tilt to port following a perturbation in lateral speed, v. The variation of Y_v with the forward speed is shown in Figure 23.

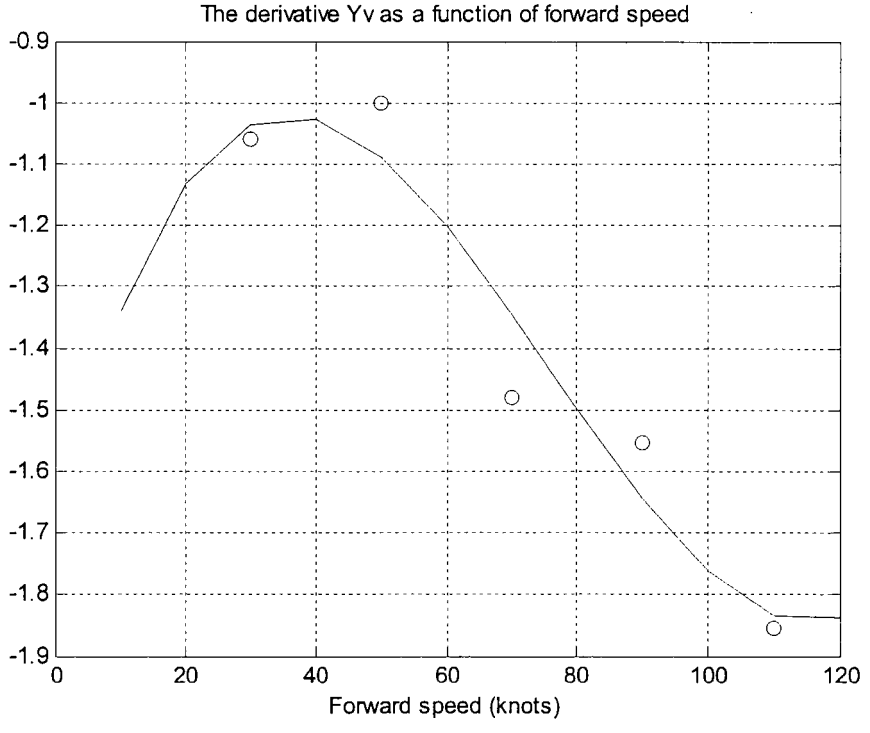

Figure 23 Variation of side force derivative, Y_v, with forward speed

The roll damping, L_p, as a primary damping derivative, reflect short-term characteristics of the aircraft (Figure 24). When the helicopter rolls starboard there will be a favorable roll moment from the main rotor to the opposite side (port) due to the aerodynamic damping. Thus, the rotor contribution to L_p is stabilizing. This aerodynamic damping effect is a function of Lock number and the size of the hinge offset [13].

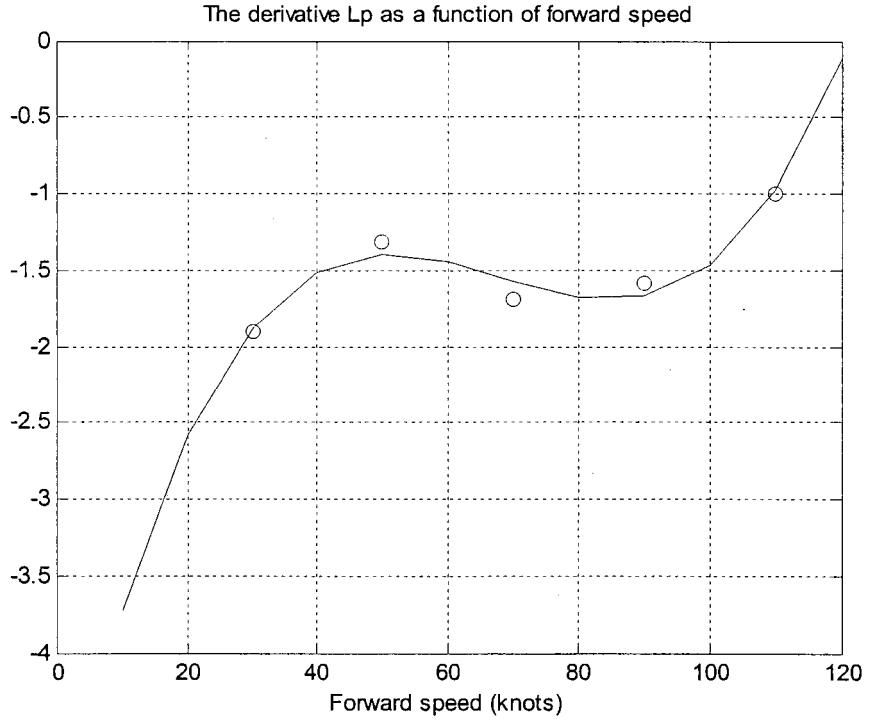

Figure 24 Variation of roll damping derivative, L_p, with forward speed

The N_v derivative is called the directional static stability or the weathercock stability. This derivative is important for both static and dynamic stability of helicopters and a positive value is stabilizing. The main contributors to it are the tail rotor, the vertical fin and the fuselage. When the fuselage centre of pressure is behind the centre of mass, the fuselage is stabilizing. The tail rotor and vertical fin have stabilizing contributions. The test helicopter flies with different side slips, as the forward speed increases. In level

flight with forward speeds of 30 knots, 70 knots and 110 knots, the lateral speeds of the helicopter are – 6,6 ft/s, - 12 ft/s and – 7,2 ft/s, respectively. The derivative follows the variation of the lateral speed, as shown in Figure 25.

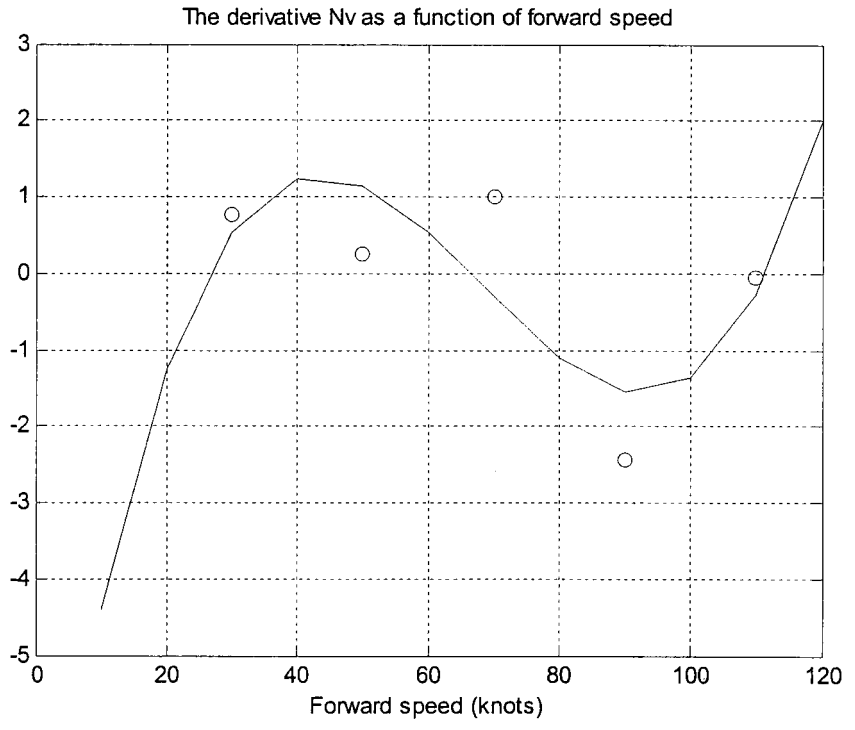

Figure 25 Variation of directional static stability derivative, N_v, with forward speed

As the forward speed increases, so does the yaw damping derivative, N_r (Figure 26). If the helicopter yaws to starboard, the tail rotor appears to be side slipping to port. A blade element of the tail rotor experiences relative airflow from a direction that will effectively increase its angle of attack. There will be an associated increase in thrust and this will produce a damping moment opposing the yaw rate. A starboard yaw rate also produces relative airflow to both fin and fuselage which gives rise to a net side force from each surface. Both associated moments make stabilizing contributions to N_r.

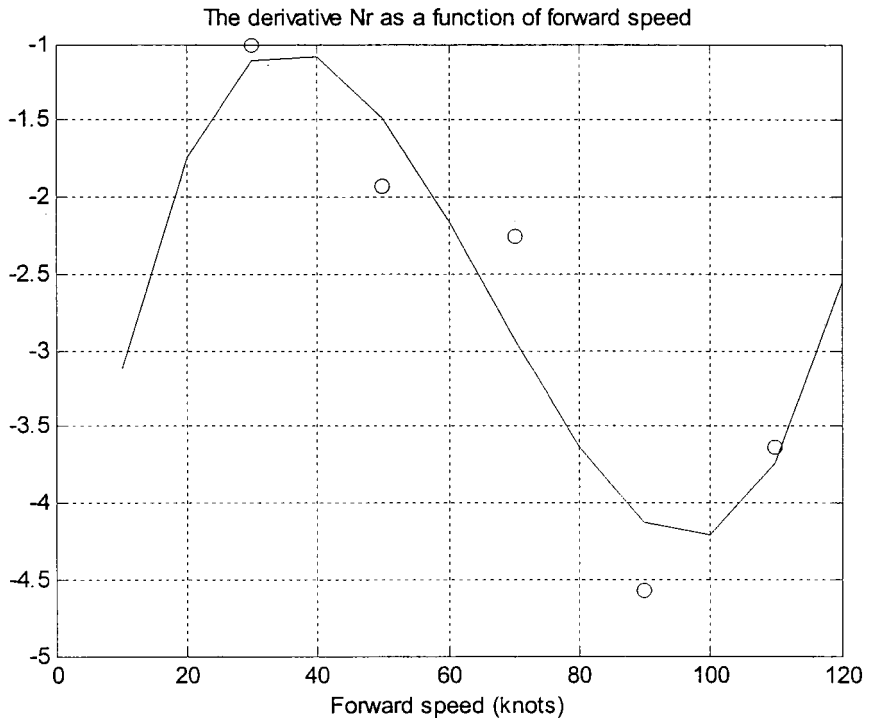

Figure 26 Variation of yaw damping derivative, N_r, with forward speed

2.2.3.4 The lateral motion

Now if the determinant of the lateral subset (1.47.b) is expanded, the resultant characteristic equation for the same example (**LHA37** test case) is:

$$\lambda^4 + c_3\lambda^3 + c_2\lambda^2 + c_1\lambda + c_0 = 0 \tag{2.14}$$

Equation (90) can be factorized as follows:

$$(T_1\lambda + 1)(T_2\lambda + 1)\left(\lambda_{dr}{}^2 + 2\zeta_{dr}\omega_{ndr}\lambda + \omega_{ndr}\right) = 0 \tag{2.15}$$

The lateral/directional motion of the helicopter in forward flight is classically composed of a roll/yaw/sideslip (Dutch roll) oscillation and two aperiodic subsidences commonly referred as the roll and spiral modes. Table VIII presents the roots of the characteristic determinant (2.4) that describe the lateral modes of full-coupled motion, and the

corresponding uncoupled values (the roots of the lateral subset determinant), for three forward speeds in level flight at 3000 ft altitude.

Table VIII

The lateral modes of motion described by the coupled system normalized eigenvalues and the corresponding uncoupled values

Lateral modes		**Forward Speed**		
		30 knots	**70 knots**	**110 knots**
Dutch roll	Coupled	-0,023 ± 0,167i	-0,061 ± 0,252i	-0,046 ± 0,289i
	Uncoupled	-0,025 ± 0,172i	-0,061 ± 0,215i	-0,1 ± 0,27i
Roll subsidence	Coupled	-1	-1	-1
	Uncoupled	-0,9832	-0,973	-0,889
Spiral	Coupled	0,0486	0,014	0,031
	Uncoupled	-0,0105	-0,036	-0,064

Table IX shows the damping ratios, undamped natural frequencies and time constants for the lateral modes of motion of the considered examples. The values were obtained using the same Pole-Zero Maps from Matlab LTI Viewer.

The lateral /directional oscillation is stable throughout the speed range although the period and damping of the oscillatory mode varies with airspeed. Depending on the relative magnitudes of lateral static stability (L_v) and directional static stability (N_v) the Dutch roll will be either convergent or divergent, and highly oscillatory or deadbeat [15].

The roll response is characterized by the shorter, first-order mode and it is stable. There is very little change in this mode with the airspeed, as depicted from Table IX.

The spiral mode is characterized by the first-order mode with the longer time constant and the mode is unstable, with the time to double the amplitude being shorter at 30 knots than at 110 knots.

Table IX

Normalized damping ratios, undamped natural frequencies and time constants of the lateral modes for full-coupled system

Lateral modes	**Forward Speed**		
	30 knots	**70 knots**	**110 knots**
Dutch roll	[0,027; 0,169]	[0,049; 0,260]	[0,042; 0,292]
Roll subsidence	(-1)	(-1)	(-1)
Spiral	(20,50)	(71,40)	(32,20)

2.2.4 Discussion of results

From the analysis of the results over the large number of flight conditions, the following observations can be made:

- The identification results demonstrate that MMLE3 is a powerful tool for extracting reliable helicopter models from flight test data; over a speed range from 30-110 knots, the MLE procedure had no convergence problem.
- The MMLE software is confined to linear model equations; the non-linear effects could only be treated as known functions calculated from measured values.
- Good starting guesses for the initial values of the derivatives were required to attain convergence and self-consistent results; the weighting factor in the cost functional had to be adjusted to balance the fits for each of the measured variables on the basis of subjective judgment of the time history plots.
- The simultaneous analysis of four maneuvers (one for each control) gave consistent convergence and allowed estimation of all stability and control derivatives.

- The characteristic modes evaluated from the derivatives can validate the pilot's experience from flight tests.

2.3 Frequency-domain identification methods

The starting point in this method is the conversion of time-based data to frequency-based data. The overall concept is to:
- extract a set of non-parametric input-to-output frequency responses that characterizes the coupled helicopter dynamics, and
- conduct a nonlinear search for a state-space model that matches the frequency response data set.

Parametric identification equations based on output-error cost function formulations presented for the time-domain techniques are essentially unchanged for the frequency-domain solution, once the time index is replaced by the frequency index. The transfer function identification is completed by direct fitting of single-input/single-output (SISO) frequency responses by using an assumed transfer function model structure. State-space model identification based on frequency response cost functions is achieved by simultaneously fitting the MIMO set of frequency responses.

The frequency-domain system identification procedure is incorporated in a comprehensive package of user-oriented programs referred to as CIFER®. A functional layout of CIFER® is shown in Figure 27.

2.3.1 SISO and MISO frequency-response calculations

The key step in the identification procedure is the extraction of accurate frequency-responses for each input/output pair. Single-input/single-output (SISO) frequency

responses for each input/output pair are determined using the Chirp-Z transform (CZT) and overlapped/windowed spectral averaging.

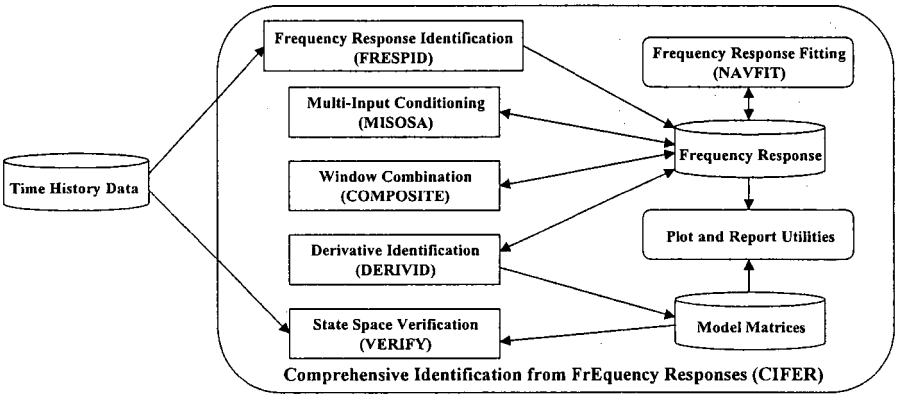

Figure 27 The Top-Level CIFER® software organization

The Fourier analysis process produces the spectral distributions of the input, output and cross-correlated signals, also referred to as the auto- and cross-correlation functions or the power spectral density (PSD) functions.

The input auto spectral density function, G_{xx}, for the sub record x_n, at the frequency ω_k, is determined from the CZT Fourier coefficients:

$$\tilde{G}_{xx} = \frac{|X(\omega_k)|^2}{N} = \frac{2}{TU}|X(\omega_k)|^2, \; k = 1, 2, \ldots, N/2 \tag{2.16}$$

where U is the scale factor for window tapering (e.g. U=1,63 for Hanning window), T is the record length, and N is the number of discrete frequency points.

The output auto spectral density function is similarly obtained from the output sub record:

$$\widetilde{G}_{yy} = \frac{|Y(\omega_k)|^2}{N} = \frac{2}{TU}|Y(\omega_k)|^2, \; k = 1, 2, \ldots, N/2 \tag{2.17}$$

The cross-spectral density function is determined by:

$$\widetilde{G}_{xy} = \frac{X^*(\omega_k)Y(\omega_k)}{N} = \frac{2}{TU}X^*(\omega_k)Y(\omega_k), \; k = 1, 2, \ldots, N/2 \tag{2.18}$$

where X^* denotes the complex conjugate.

Finally, the total spectral-function estimate for the entire (concatenated) time history is obtained from a linear average of the spectra for the k overlapped sub records.

The physical interpretation of the spectral-density estimates is the mean-squared response of the respective signals (xx, yy, xy) as a function of frequency. Presenting the spectral density magnitudes in power dB ($G_{xx}(dB) = 10\log_{10} G_{xx}$) gives the distribution of the root-mean-squared response.

Once the input, output, and cross-spectral density estimates have been determined for a selected time history pair (e.g. the lateral control δ_{lat} and the roll rate p), the estimated single input single output (SISO) frequency responses, $H(\omega)$, can be determined from the ratio between the cross spectral density and the input spectral density:

$$H(\omega) = \frac{G_{xy}(\omega)}{G_{xx}(\omega)} \tag{2.19}$$

The transfer function results are then presented in standard Bode plots. By analyzing the auto spectrums of inputs and outputs, the frequency content of the flight data can be determined. The spectral density functions will be a good indicator of the range of valid frequency response identification. Figure 28 depicts an example of the lateral input autospectrum in **LHA37** case and its associated range of validity from 0,5 rad/s to 5 rad/s.

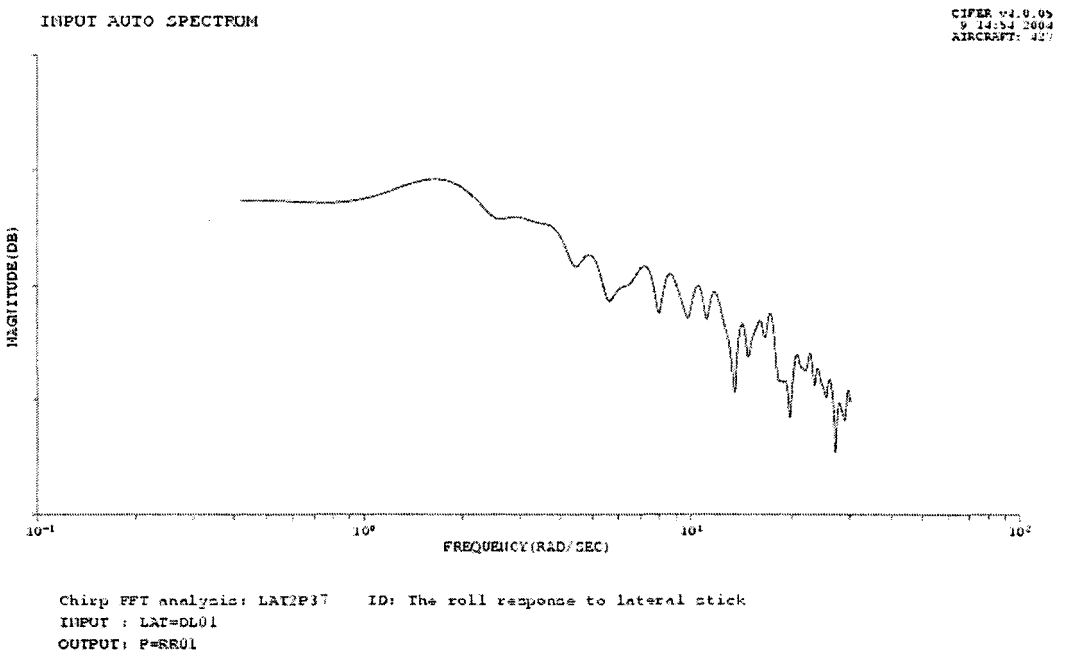

Figure 28 The lateral stick input (δ_{lat}) autospectrum

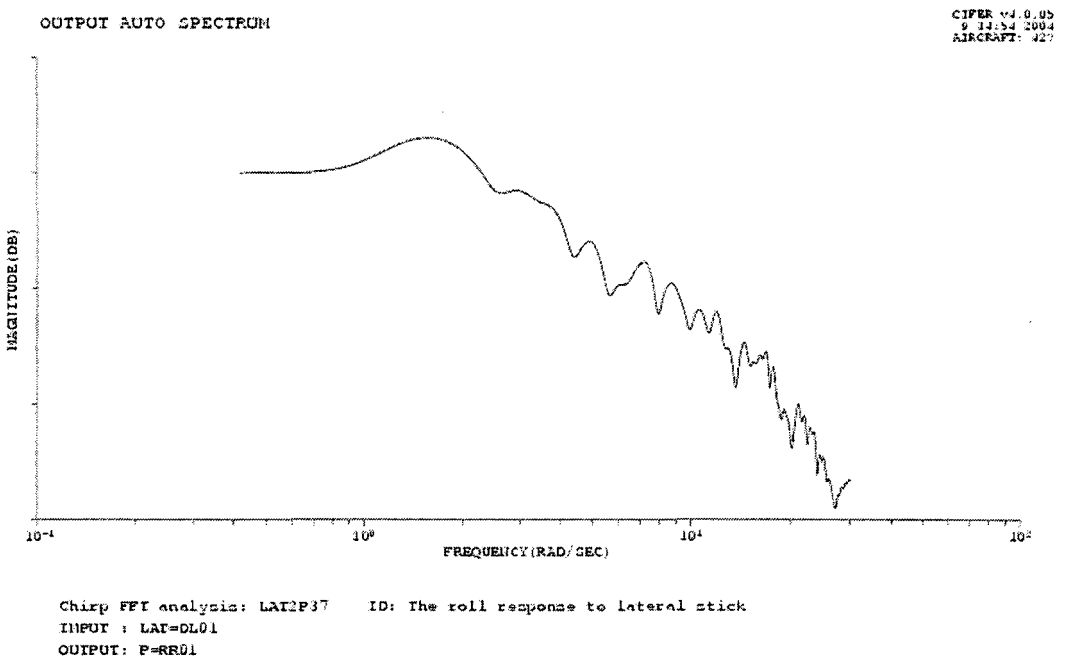

Figure 29 The roll rate response (p) auto spectrum to lateral stick input (δ_{lat})

The roll rate response autospectrum for lateral stick input is shown in Figure 29. The output autospectrum reflects the physical nature of the aircraft response. The relative peak at approximately 1,5 rad/s is due to the presence of a dominant roll mode at that frequency range. The rapid drop-off is due to the inertial (rigid body) aircraft response.

Factors that influence the input auto spectrum include the length and number of concatenated data runs, the quality and frequency content of flight test input, the bandwidth and sensitivity of the instrumentation, and the selection of window size used for the FFT [7].

Most test data generated by the pilot involve inputs to multiple controls. For helicopters, especially those with stiff rotors, pilot off-axis control activity will always occur because of coupling and the necessity to remain near the trim condition. If dynamic coupling exists in the system being identified, the presence of correlated secondary inputs will distort the frequency-responses obtained from the SISO relationship (2.19).

When n_c multiple control inputs are present in the excitation, as is the case for the Bell 427 data, the contaminating effects of partially correlated inputs must be removed. The required conditioned transfer-function matrix $T(\omega_k)$ is obtained as follows:

$$T(\omega_k) = G_{xx}^{-1}(\omega_k)G_{xy}(\omega_k) \tag{2.20}$$

where

G_{xy} = [n_cx1] matrix of SISO cross-spectra between each control input and the single output

G_{xx} = [n_c x n_c] matrix of auto- and cross-spectra between the n_c inputs.

This matrix solution is determined at each frequency point ω_k and then again for each output to yield a set of "conditioned" frequency responses. These conditioned multi-input/single-output (MISO) responses are the same as the SISO frequency

responses that would have been obtained had no correlated controls been present during the frequency sweep of a single control.

The MISOSA function from CIFER® allows up to four secondary inputs in addition to the primary input. The resulting "conditioned" frequency response is calculated for the primary input.

The coherence function γ_{xy}^2 calculated at each frequency point indicates the accuracy of the identified frequency response. The coherence function is calculated using the relationship:

$$\gamma_{xy}^2 = \frac{|G_{xy}|^2}{|G_{xx}||G_{yy}|} \tag{2.21}$$

The coherence function can be interpreted as that fraction of the output spectrum that can be accounted for by a linear relation with the input spectrum. If the system was perfectly linear and the spectral estimates were noise free, the coherence function would be unity within the frequency range excited. Generally, there are three contributions to reducing the coherence function over the valid frequency range: a) the non-linearities present in the actual physical system; b) the presence of measurement noise or process noise; c) the secondary inputs. In this case, the secondary inputs include not only the off-axis control inputs, but also external inputs such as gusts.

Rapid drop in γ_{xy}^2 indicates poor accuracy. A coherence function greater than 0,6 generally indicates acceptable accuracy for that frequency point.

The Bode plot and the coherence of p/δ_{lat} considering a single 15-sec window, is shown in Figure 30. In the mid-frequency range, the coherence begins to oscillate due to reduced spectral averaging, which indicates the degradation of the identification quality.

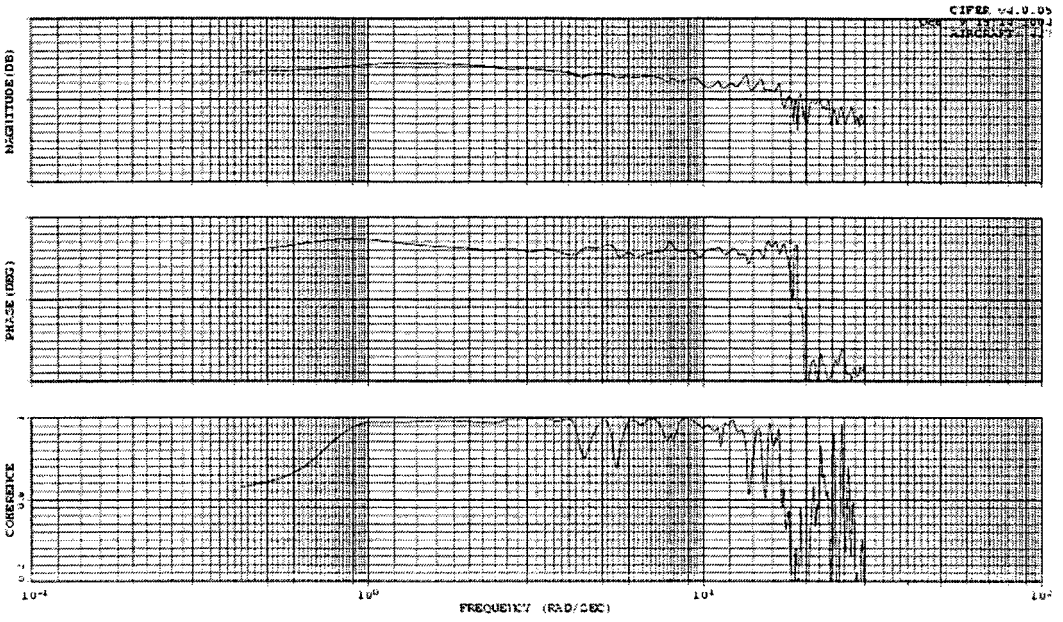

Figure 30 The roll-rate response (p) to lateral stick input (δ_{lat}) (15 s window)

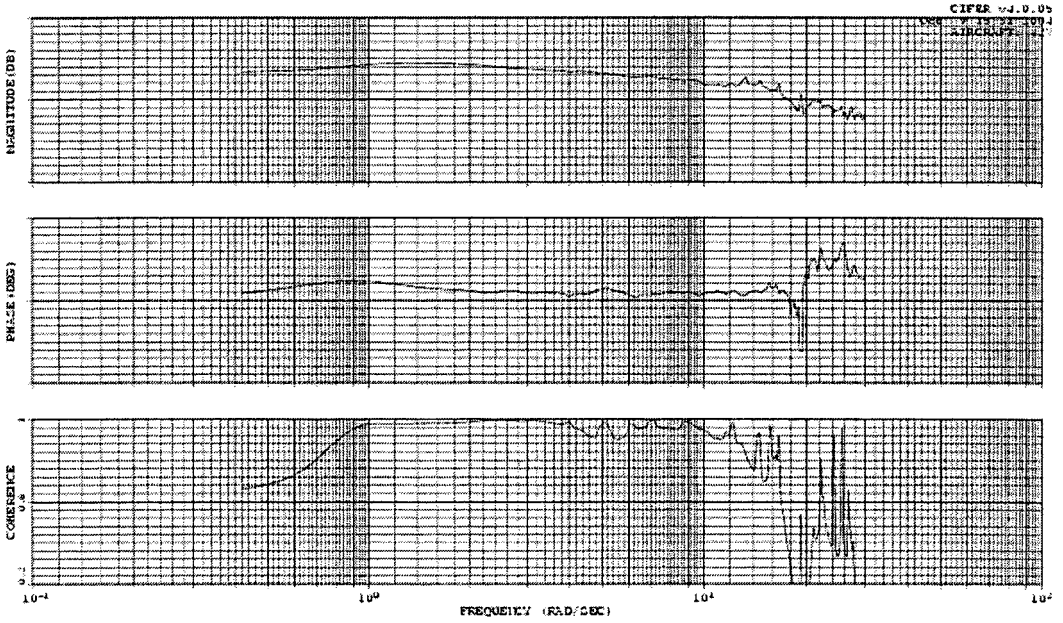

Figure 31 Composite roll-rate response to lateral stick input, obtained by a combination of 5 windows (2, 3, 5, 8, 10 s)

The composite coherence result of p/δ_{lat} for five windows (2, 3, 5, 8 and 10 s) is shown in Figure 31. The result indicates very good identification (coherence $\gamma^2 > 0{,}8$) over a wide frequency range (0,7-12 rad/sec) with considerable improvement in the spectral oscillation compared to the single window result of Figure 30.

2.3.2 Frequency-response cost function formulation

In the current frequency-response approach, stability and control derivatives identification is achieved directly through iterative multi-input/multi-output matching of the identified conditioned frequency responses with those of the following linear model:

$$M_m \dot{x} = F_m x + G_m u \tag{2.22}$$

$$y = H_m x + j_m u \tag{2.23}$$

where the matrix M_m has been included to allow the direct identification of stability derivatives that are dependent on state rates (e.g., side-wash lag derivative, N_v). The elements of M_m, F_m, G_m, H_m and j_m are the unknown stability and control derivatives. Some of these elements may be known from physical considerations and/or direct transfer function modeling.

Taking the Laplace transform of Equations (2.22) and (2.23) results in the following state space model transfer function:

$$T_m(s) = H_m\left[sI - M_m^{-1}F_m\right]^{-1}M_m^{-1}G_m + j_m \tag{2.24}$$

To account for time delays associated with unmodeled higher-order states, a matrix of time delays, $\tau_m(s)$, may be incorporated:

$$\tau_m(s) = e^{-\tau s} \tag{2.25}$$

Also, allowing H_m to be a function of s may eliminate the control feedthrough term j_m:

$$T_m(s) = H_m(s)\left[sI - M_m^{-1}F_m\right]^{-1}M_m^{-1}G_m\tau_m(s) \tag{2.26}$$

The frequency responses of the state space model are obtained by replacing $s=j\omega$ in Equation (11).

The unknown state-space model parameters (ξ) are determined by minimizing the cost function J, a weighted function of the error ε between the identified MISO (composite) frequency responses $T(s)$ and the model responses $T_m(s)$ over a selected frequency range:

$$J(\xi) = \sum_{n=1}^{n_\omega} \varepsilon^T(\omega_n, \xi)\, W \varepsilon(\omega_n, \xi) \tag{2.27}$$

The frequency ranges for the identification criterion (ω_1, ω_2,..., ω_n) are selected individually for each input/output pair according to their individual ranges of good coherence. In this way, only valid data are used in the fitting process. The weighting matrix W is based on the values of coherence at each frequency point to emphasize the most accurate data. An iterative non-linear pattern search algorithm is used to adjust both the stability and control derivatives and the time delays in the model until convergence on a minimum criterion of Equation (2.27) is achieved. The pattern search method has been found to be highly robust for very large problem sizes associated with the helicopter identification.

2.3.3 Frequency-response identification

The data used in frequency-domain identification was taken from the same tests chosen for the time-domain analysis (Table IV). Experience has shown that flight test data obtained from frequency sweep control inputs are better suited for the frequency-domain approach than multi-step inputs; however, care should be taken because unexpected structural resonances which were not identified during structural demonstrations or during the operational flight have been encountered during frequency sweep tests [7]. In this study, the only available set of inputs for the frequency response identification was the 2311-multistep inputs from time-domain analysis.

The available data record is quite short and should only provide a short-term response. Typical record lengths in frequency domain for aircraft system identification are at least 60 s, and at least two repeats for each axis. In this case, the record length is about 20 s and there is only one record available, for each input. This will allow a 10 s window at best, and give a minimum frequency of no more than about 1,25 rad/sec.

The 6 DoF formulation of the helicopter model accounts for rotor dynamics as simple time delays. Such models can adequately describe the low- and mid-frequency dynamics of the helicopter up to about 12 rad/sec. Frequency-domain techniques are well suited to time delay identification because the time delay causes a linear increase in phase shift with frequency and thus a linear effect in the cost function. The time delays were identified with the NAVFIT feature in CIFER® for a level flight at 3000 ft and forward speed of 30 knots, from a transfer-function fit of the pitch, roll, yaw rates and vertical acceleration responses to the corresponding on-axis inputs, as depicted from Figure 32 to Figure 35. The time delays obtained with CIFER® were comparable to those estimated in time domain analysis with a standard deviation of 0,03 (i.e. 1,5 samples).

Frequency-response identification (using FRESPID function) and data conditioning with a range of window sizes of 10, 8, 5, 3, and 2 s (using COMPOSITE function) were conducted to obtain a matrix (Table X) of input-to-output frequency responses. Table X is built based on the frequency ranges of good coherence for each input/output pair.

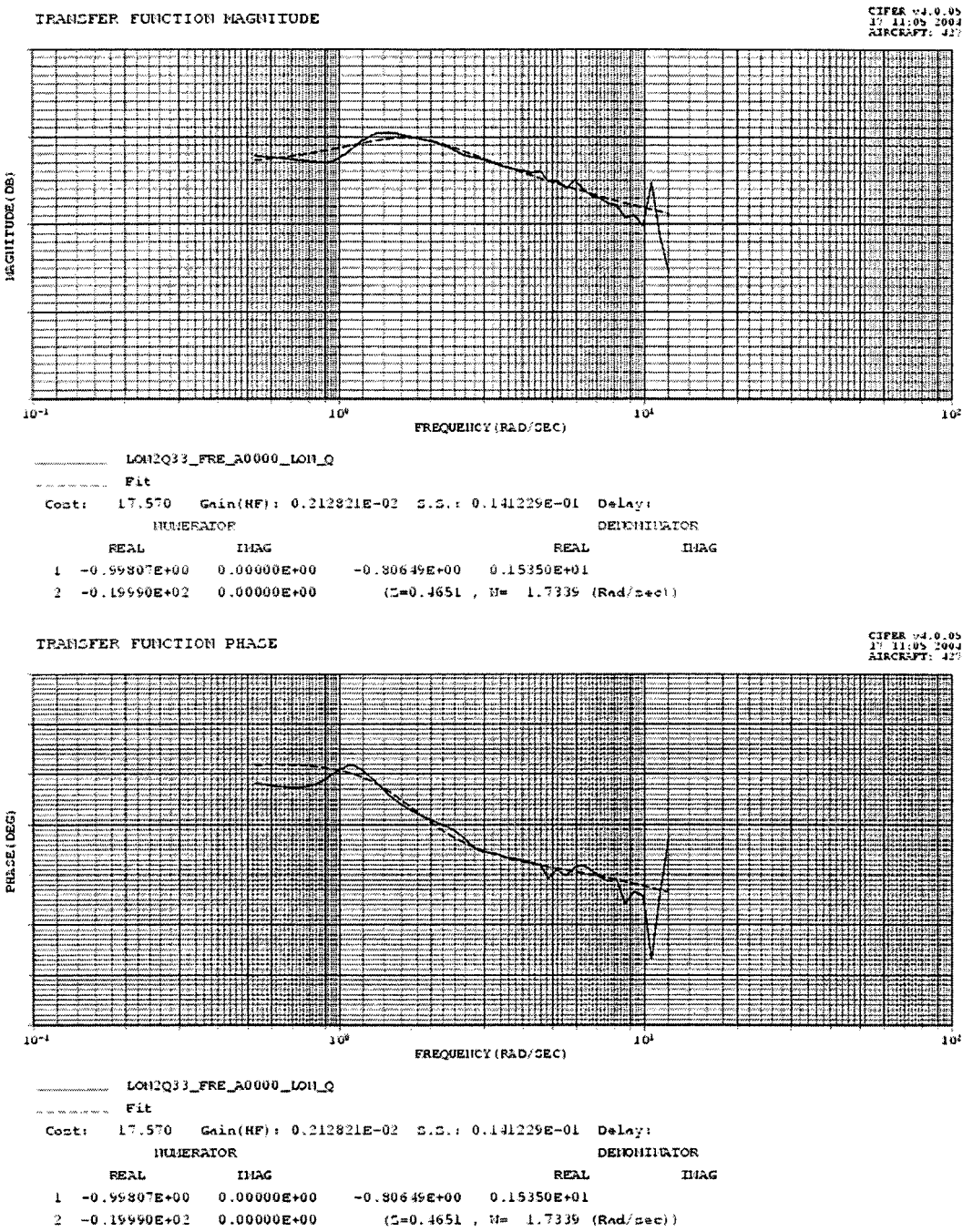

Figure 32 The Bode plot of the pitch rate response to longitudinal input; (q/δ_{lon}) second order transfer function fit with flight test data

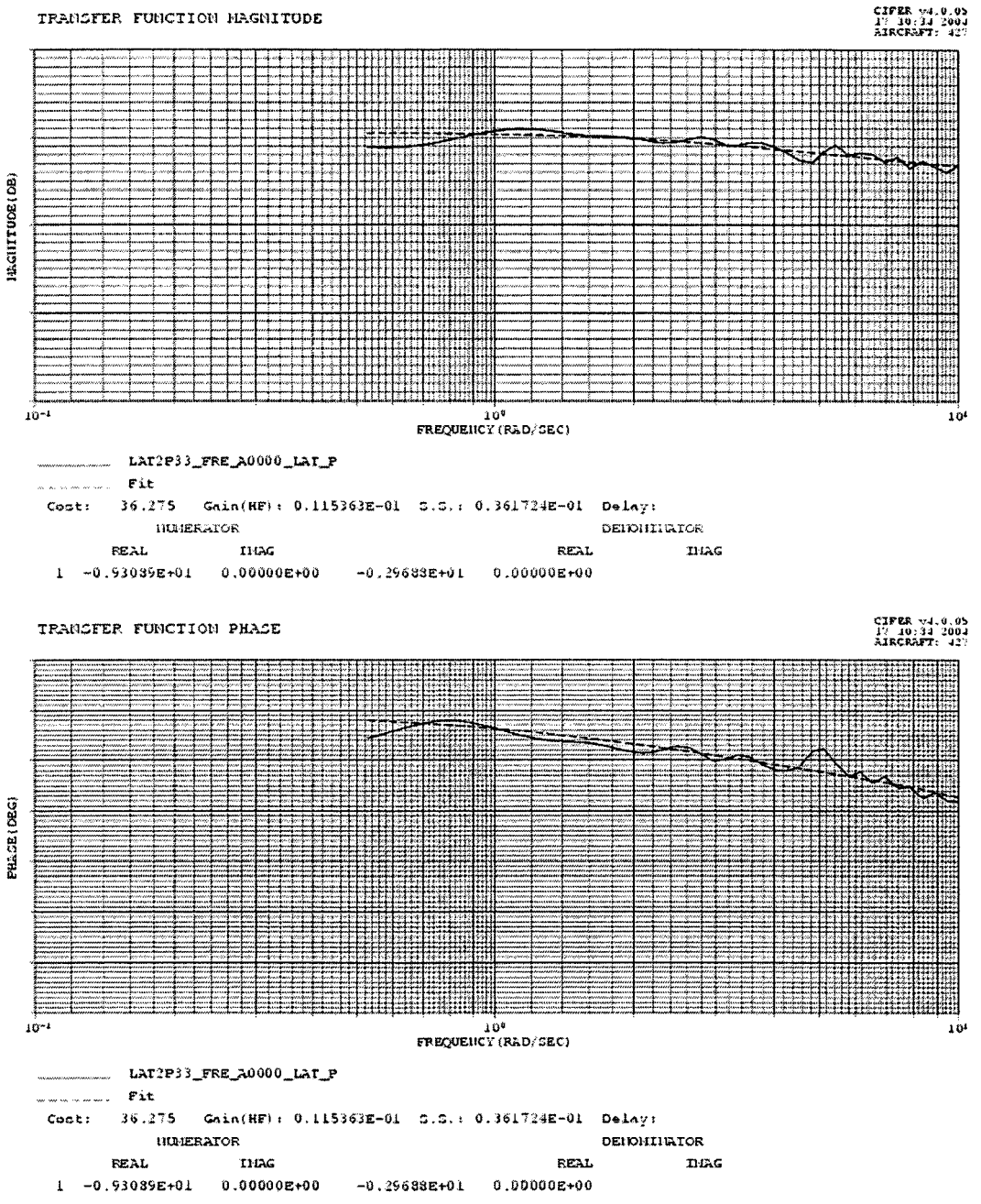

Figure 33 The Bode plot of the roll rate response to lateral input; (p/δ_{lat}) first order transfer function fit with flight test data

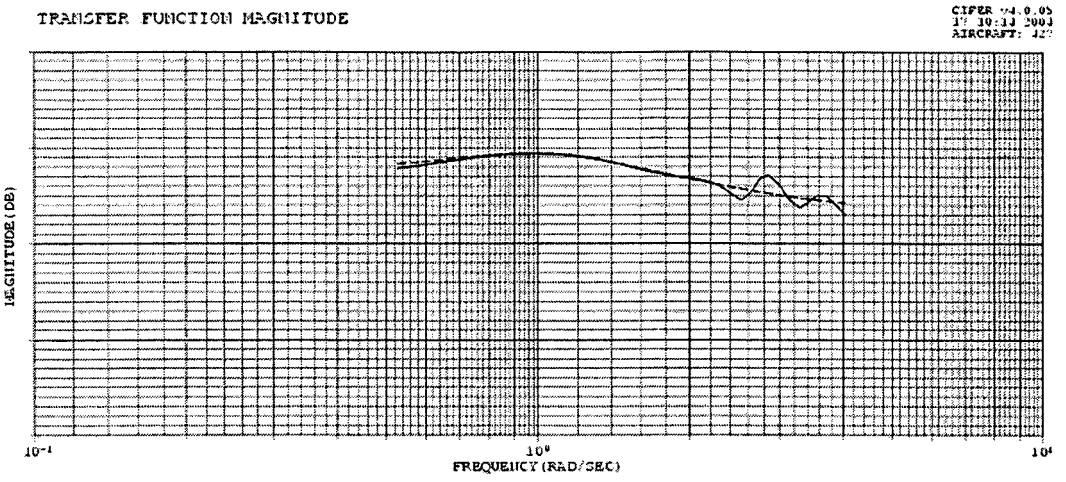

PED2R33_FRE_A0000_PED_R
Fit
Cost: 26.008 Gain(HF): 0.601213E-02 S.S.: 0.169642E-01 Delay:

	NUMERATOR		DENOMINATOR	
	REAL	IMAG	REAL	IMAG
1	-0.99109E+00	0.00000E+00	-0.52998E+00	0.95123E+00
2	-0.33758E+01	0.00000E+00	(ζ=0.4867 , ω= 1.0889 (Rad/sec))	

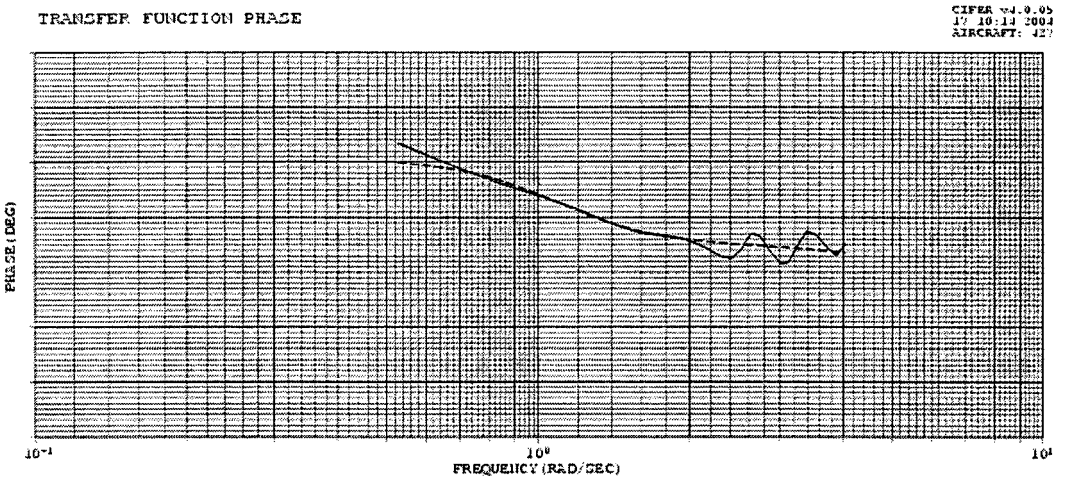

PED2R33_FRE_A0000_PED_R
Fit
Cost: 26.008 Gain(HF): 0.601213E-02 S.S.: 0.169642E-01 Delay:

	NUMERATOR		DENOMINATOR	
	REAL	IMAG	REAL	IMAG
1	-0.99109E+00	0.00000E+00	-0.52998E+00	0.95123E+00
2	-0.33758E+01	0.00000E+00	(ζ=0.4867 , ω= 1.0889 (Rad/sec))	

Figure 34 The Bode plot of the yaw rate response to pedal input; (r/δ_{ped}) second order transfer function fit with flight test data

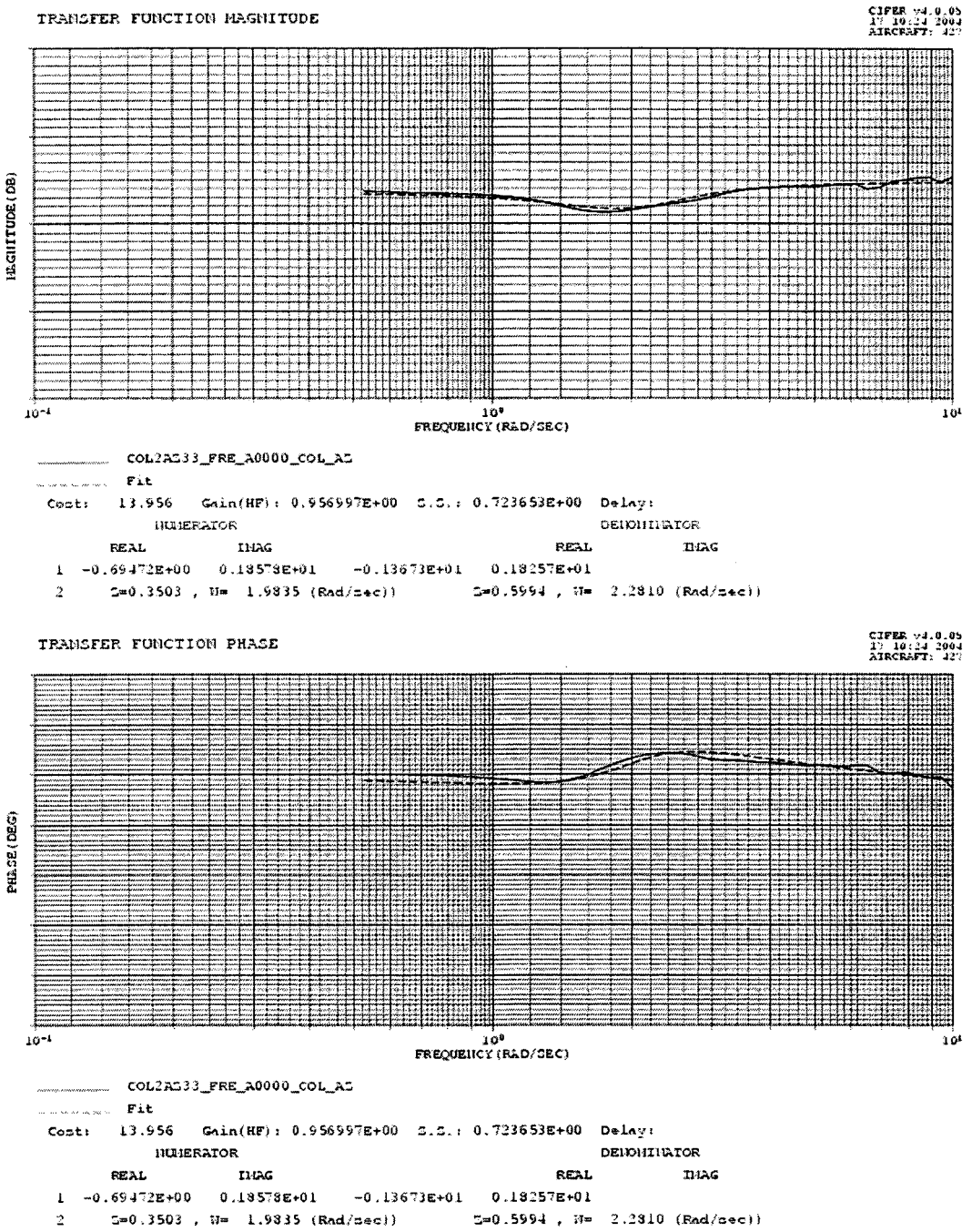

Figure 35 The Bode plot of the normal acceleration response to collective input; (n_z / δ_{col}) second order transfer function fit with flight test data

Table X

Set up for Bell 427 frequency-domain identification

LHA37	δ_{lon}	δ_{lat}	δ_{ped}	δ_{col}
u	*			*
v			*	
w	*			
p		*		
q	*			*
r			*	
a_x	*			*
a_y		*	*	
a_z				*

* indicates a valid input/output frequency response.

Generating the frequency responses for **LHA37** test case, a satisfactory identification was achieved for few input/output responses, from the 36 possible transfer functions combinations.

The multi-input analysis of Bell 427 helicopter showed a high level of control coupling, especially between the lateral and longitudinal data. Pilot off-axis control activity occurred because of coupling and the necessity to remain near the trim condition. As depicted from Figure 36, the coupled (off-axis) roll rate response due to the longitudinal stick input is almost as high as the primary pitch rate response. The presence of the correlated secondary inputs distorts the identified SISO response.

The conclusion was that the on-axis responses are acceptable and it is feasible to determine a decoupled longitudinal and/or lateral model but it is impossible to obtain a fully coupled model. Therefore, a frequency-domain analysis of the simplified,

uncoupled, longitudinal and lateral/directional models is presented for different flight test cases, rather than a coupled 6 DoF model from time domain.
The initial setup, based on matrix Equation (2.26), is shown for the longitudinal model in Table XI and for the lateral/directional model in Table XII. The procedure is the same for all other flight conditions.

Stability and control derivatives identification is achieved directly through iterative multi-input/multi-output matching of the identified frequency responses with those of the linear model from Equations (2.22) and (2.23). As in the time-domain methods, three key metrics of parameter accuracy and correlation are calculated from the Hessian matrix: a) Parameter insensitivity; b) Cramer-Rao bound; c) Confidence ellipsoid.

Table XIII presents the error relative to the MMLE values, in percentage, between the derivatives obtained with MMLE and those obtained with CIFER®, along with the associated Cramer-Rao bounds and insensitivities provided by the frequency-domain identification. The results obtained by the frequency-domain identification method are given in the format of frequency response fits in Figures 37 to 50.

There are quite large differences between the identification results of the two methods. The simplified models (longitudinal or lateral directional) used for frequency- domain identification do not account for the large coupling existing in the case of a helicopter. The obtained values of roll damping, L_p, pitch damping, M_q, and yaw damping, N_r, highly depend on the equivalent time delays and the high correlation of the control derivatives. The best agreement between the two identification methods is shown in the case of the control derivatives.

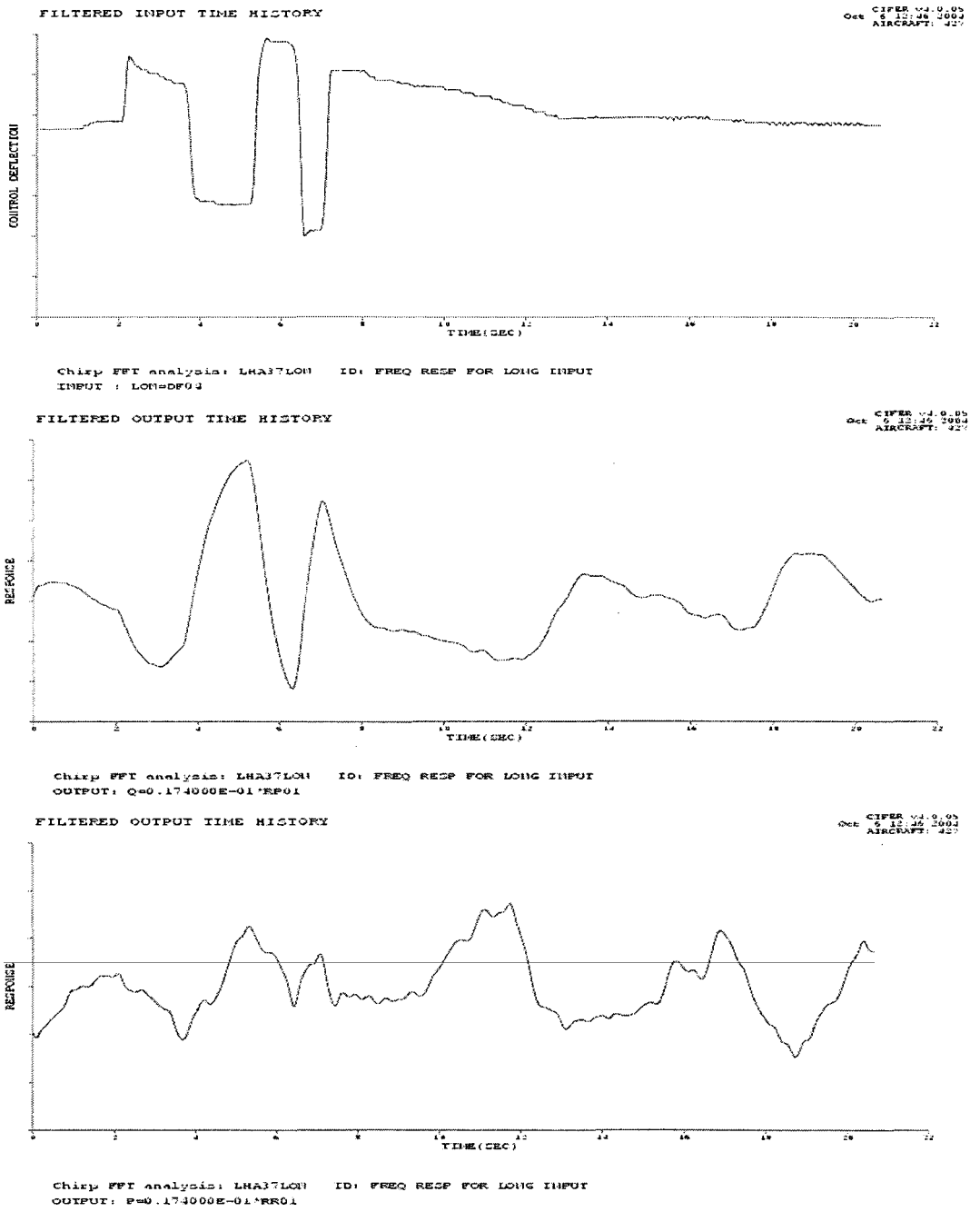

Figure 36 The on-axis (pitch rate, q) and off-axis (roll rate, p) responses to longitudinal input

Table XI

Initial setup for the longitudinal model

LHA37LON	δ_{lon}	δ_{col}
$\dot{u}$	0,7-3	2-4
$\dot{w}$	0,7-3	None
q	0,7-10	2-4
a_x	0,7-7	2-6
a_z	none	0,7-12

M-matrix	u	w	q	θ
u	1	0	0	0
w	0	1	0	0
q	0	0	1	0
θ	0	0	0	1

F-matrix	u	w	q	θ
u	X_u	X_w	$X_q - w_e$	$-g\cos\theta_e$
w	Z_u	Z_w	$Z_q + u_e$	$-g\sin\theta_e$
q	M_u	M_w	M_q	0
θ	0	0	1	0

H-matrix	u	w	q	θ
u	1	0	0	0
w	0	1	0	0
q	0	0	1	0
a_x	s	0	w_e	$g\cos\theta_e$
a_z	0	s	$-u_e$	$g\sin\theta_e$

G-matrix	δ_{lon}	δ_{col}
u	X_{lon}	X_{col}
w	Z_{lon}	Z_{col}
q	M_{lon}	M_{col}
θ	0	0

Table XII

Initial setup for the lateral/directional model

LHA37LAT	δ_{lat}	δ_{ped}
$\dot{v}$	None	0,8-7
p	0,7-12	None
r	None	1-8
a_y	0,9-4	0,8-4

M-matrix	v	p	r	ϕ
v	1	0	0	0
p	0	1	0	0
r	0	0	1	0
ϕ	0	0	0	1

F-matrix	v	p	r	ϕ
v	Y_v	$Y_p + w_e$	$Y_r - u_e$	$g\cos\theta_e$
p	L_v	L_p	L_r	0
r	N_v	N_p	N_r	0
ϕ	0	1	$\tan\theta_e$	0

H-matrix	v	p	r	ϕ
v	1	0	0	0
p	0	1	0	0
r	0	0	1	0
a_y	s	$-w_e$	u_e	$-g\cos\theta_e$

G-matrix	δ_{lat}	δ_{ped}
v	Y_{lat}	Y_{ped}
p	L_{lat}	L_{ped}
r	N_{lat}	N_{ped}
a_y	0	0

Table XIII

Comparison of MMLE and CIFER identification results

Case		Parameter	Error[%]	Cramer-R	Insensitivities[%]
LHA37	Longitudinal	Xu	8,88	18,73	6,967
		Xw	0,23	7,097	2,652
		Mq	0,21	4,186	1,494
		Xlon	0,04	6,064	2,494
		Xcol	0,07	3,662	1,569
		Zcol	0,12	3,722	1,848
		Mlon	0,09	2,99	1,106
		Mcol	0,13	3,34	1,568
	Lateral/directional	Yv	0,48	9,442	2,985
		Yp	0,16	12,20	1,971
		Yr	45,84	12,30	3,735
		Lp	0,14	8,437	1,805
		Nr	1,13	6,072	1,742
		Ylat	0,33	7,747	1,280
		Yped	1,38	10,84	3,022
		Llat	0,31	6,621	1,486
		Nped	1,03	3,981	1,227
C10LF69	Longitudinal	Xq	0,25	11,82	4,345
		Zw	0,30	12,75	4,299
		Zq	18,69	7,828	3,17
		Mq	0,69	7,849	2,14
		Xlon	0,01	4,282	1,607
		Zlon	0,34	4,867	1,808
		Zcol	0,22	2,796	1,379
		Mlon	0,60	4,836	1,305
	Lateral/directional	Yv	0,58	5,535	2,355
		Yr	0,73	8,906	3,794
		Lp	0,22	7,372	1,021
		Lr	0,01	8,340	1,906
		Nv	1,74	3,759	1,356
		Np	0,11	7,716	1,185
		Nr	0,24	5,929	1,174
		Llat	0,12	5,914	0,9429
		Lped	0,05	6,802	1,724
		Nlat	0,12	7,938	1,357
		Nped	0,02	3,632	0,8274

Table XIII (cont.)

Comparison of MMLE and CIFER identification results.

Case		Parameter	Error[%]	Cramer-R	Insensitivities[%]
D10LA310	Longitudinal	Xw	0,09	5,569	1,861
		Xq	0,35	6,355	1,908
		Zw	1,70	9,818	2,055
		Zq	1,70	7,317	1,933
		Mu	183,41	7,647	1,752
		Mw	2,21	7,056	1,292
		Mq	0,27	3,795	0,8382
		Xlon	0,11	5,282	1,92
		Xcol	0,03	5,619	1,967
		Zlon	0,44	4,991	2,145
		Zcol	0,22	3,808	1,283
		Mlon	0,09	3,976	1,001
		Mcol	0,41	3,826	0,9767
	Lateral/directional	Yv	0,15	7,497	2,555
		Yp	0,05	9,716	1,157
		Lp	0,13	7,386	0,8741
		Np	0,04	8,196	0,9852
		Nr	0,09	5,472	1,673
		Ylat	0,08	8,216	1,061
		Yped	2,05	6,97	3,181
		Llat	0,05	6,145	0,8
		Nlat	0,06	6,891	0,9371
		Nped	0,05	3,714	1,293
AHF68	Longitudinal	Xq	0,32	7,11	1,88
		Zw	0,10	5,152	2,304
		Mw	0,01	5,711	2,499
		Mq	0,69	4,775	1,101
		Xlon	0,22	3,812	1,164
		Zcol	0,12	3,575	1,732
		Mlon	0,53	4,139	1,048
		Mcol	0,51	4,266	1,412

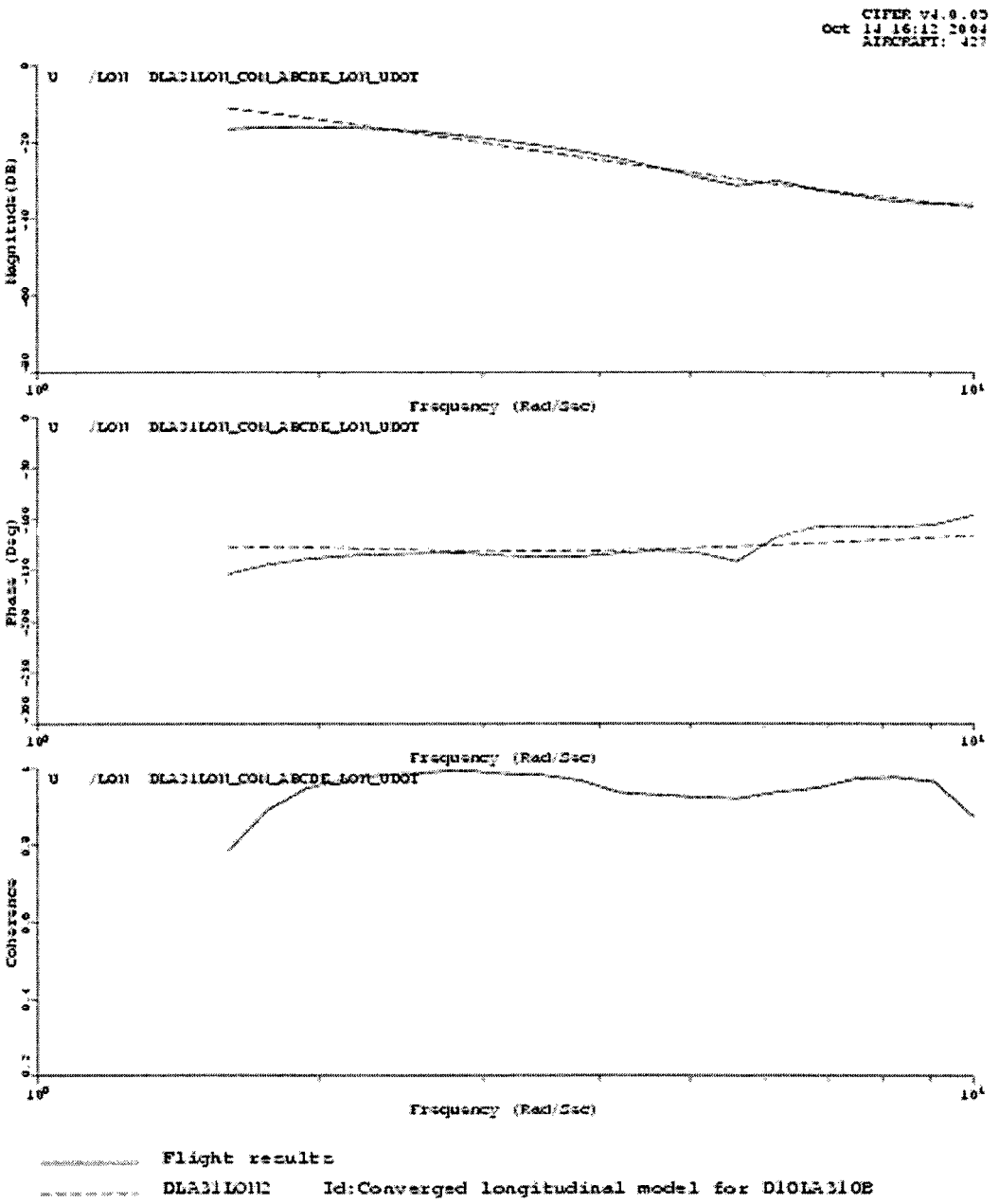

Figure 37 Bode plots comparison between flight data and identified longitudinal model frequency response, for u/δ_{lon}

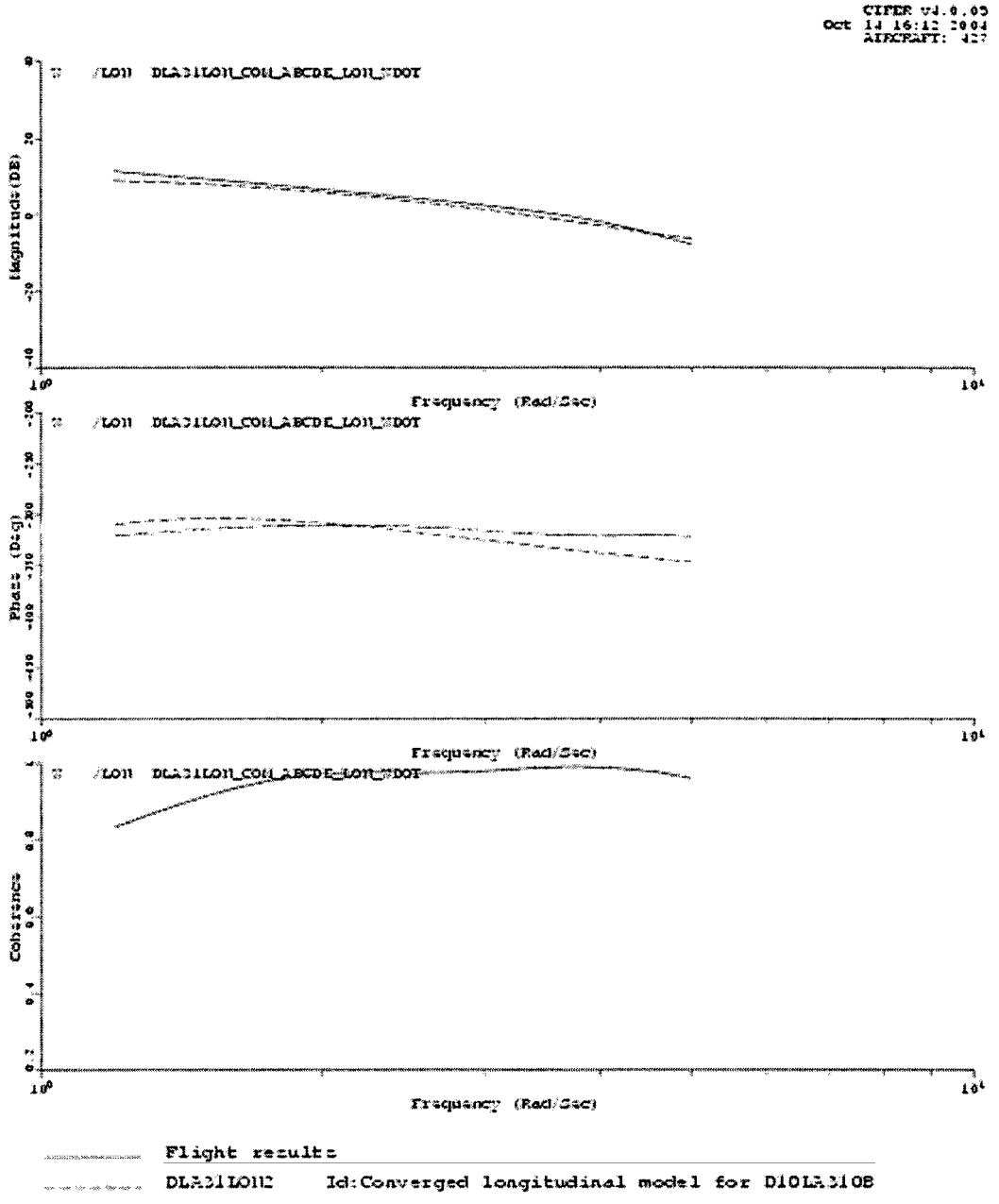

Figure 38 Bode plots comparison between flight data and identified longitudinal model frequency response, for w/δ_{lon}

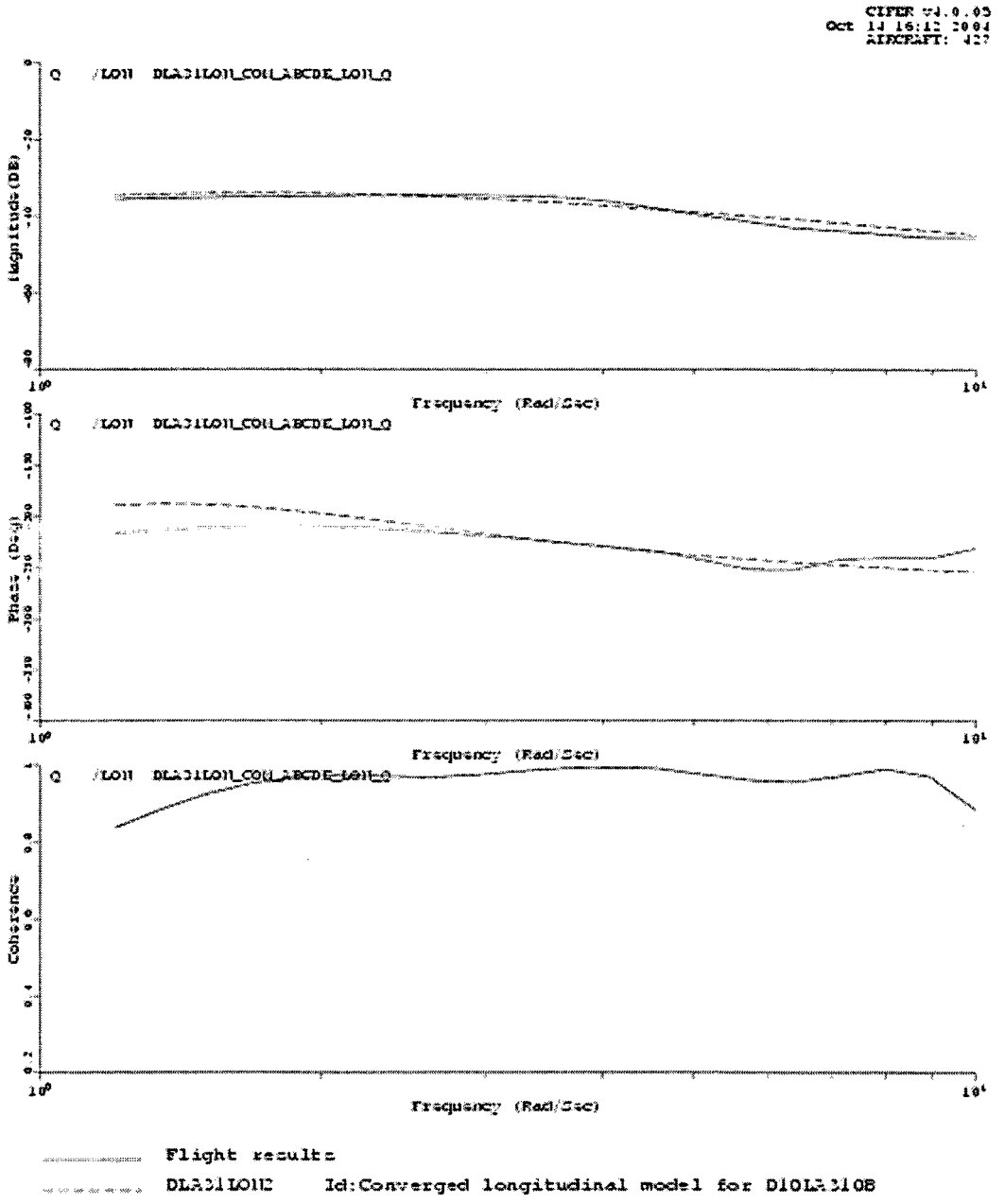

Figure 39 Bode plots comparison between flight data and identified longitudinal model frequency response, for q/δ_{lon}

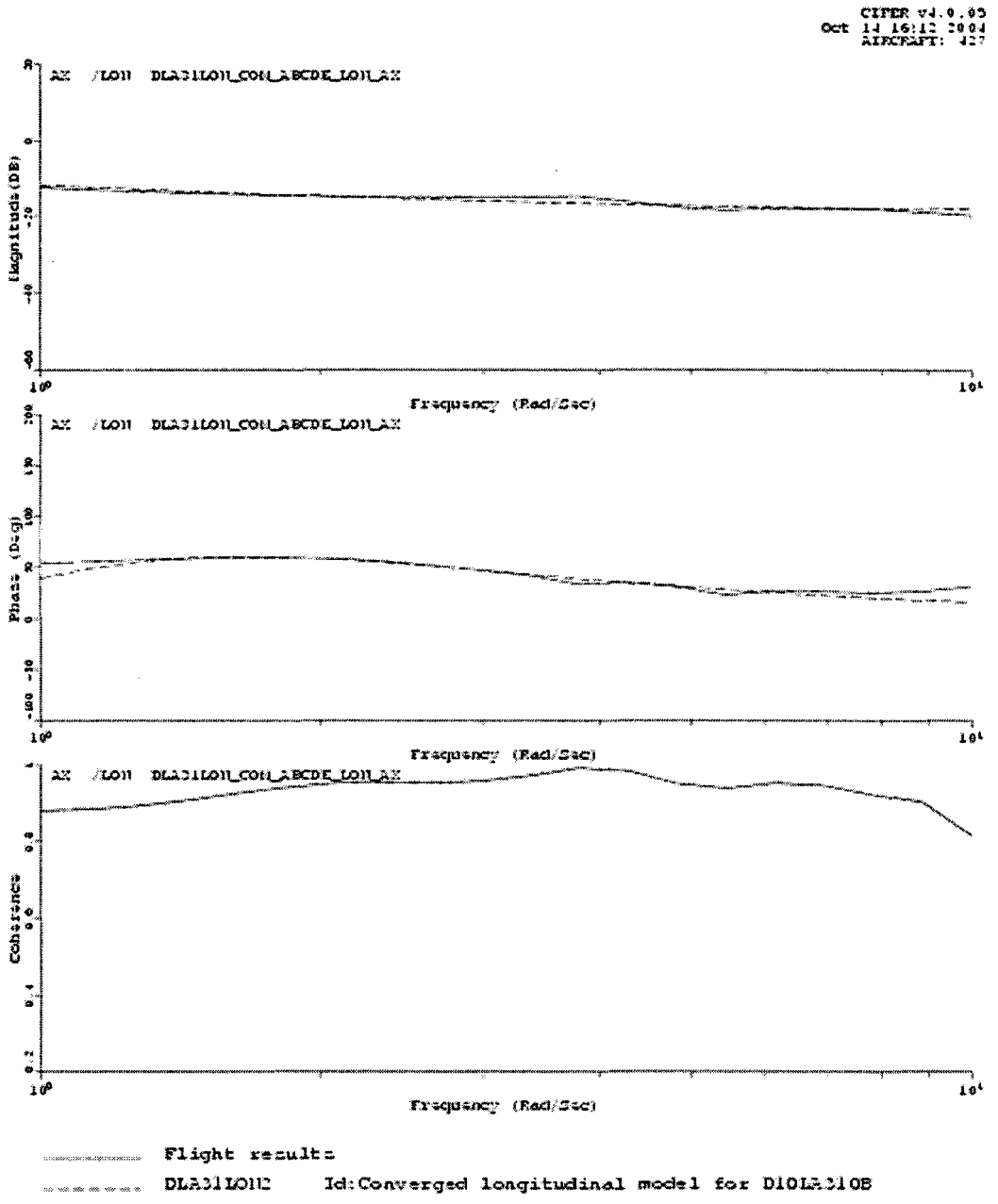

Figure 40 Bode plots comparison between flight data and identified longitudinal model frequency response, for a_x / δ_{lon}

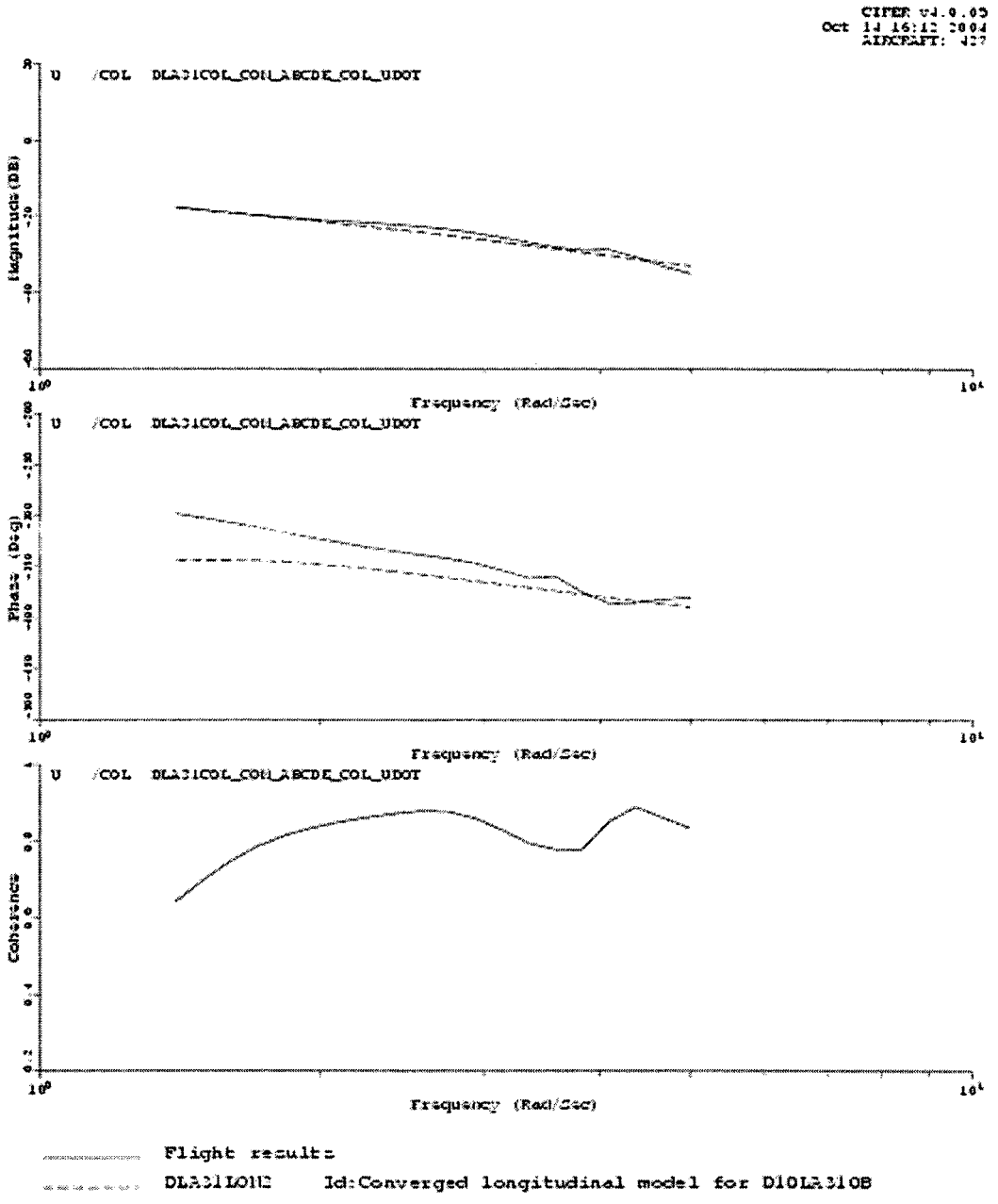

Figure 41 Bode plots comparison between flight data and identified longitudinal model frequency response, for u/δ_{col}

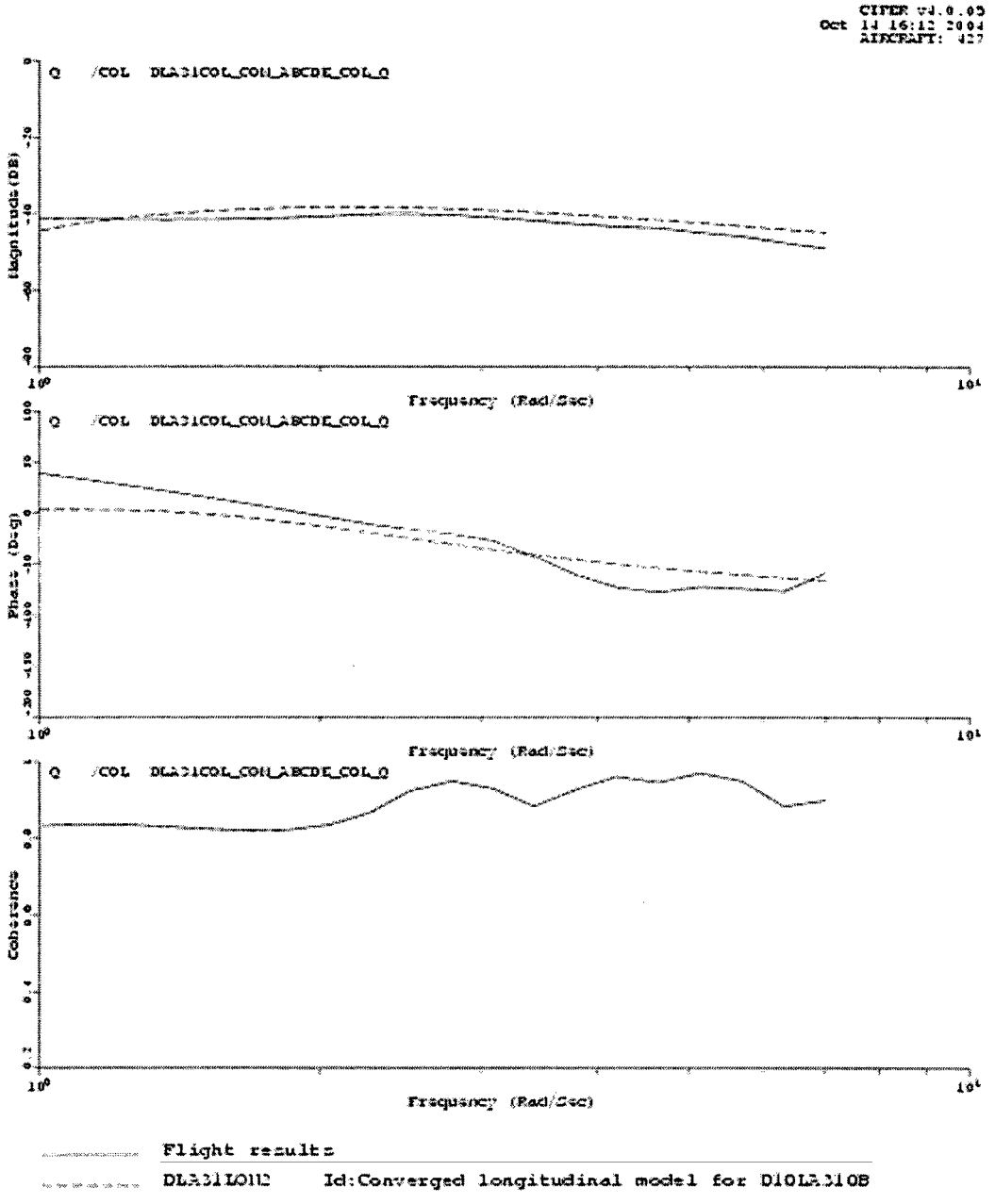

Figure 42 Bode plots comparison between flight data and identified longitudinal model frequency response, for q/δ_{col}

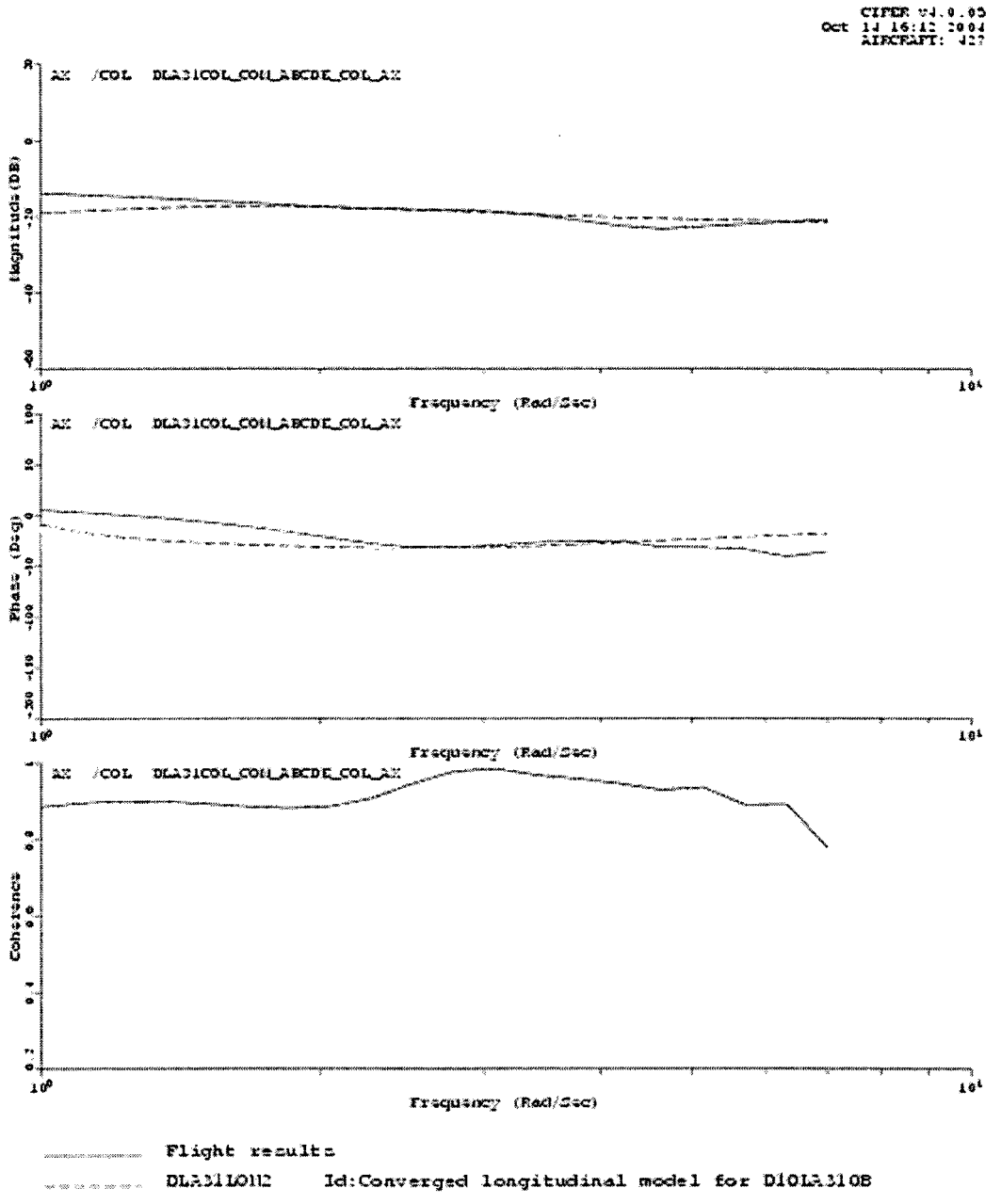

Figure 43 Bode plots comparison between flight data and identified longitudinal model frequency response, for a_x / δ_{col}

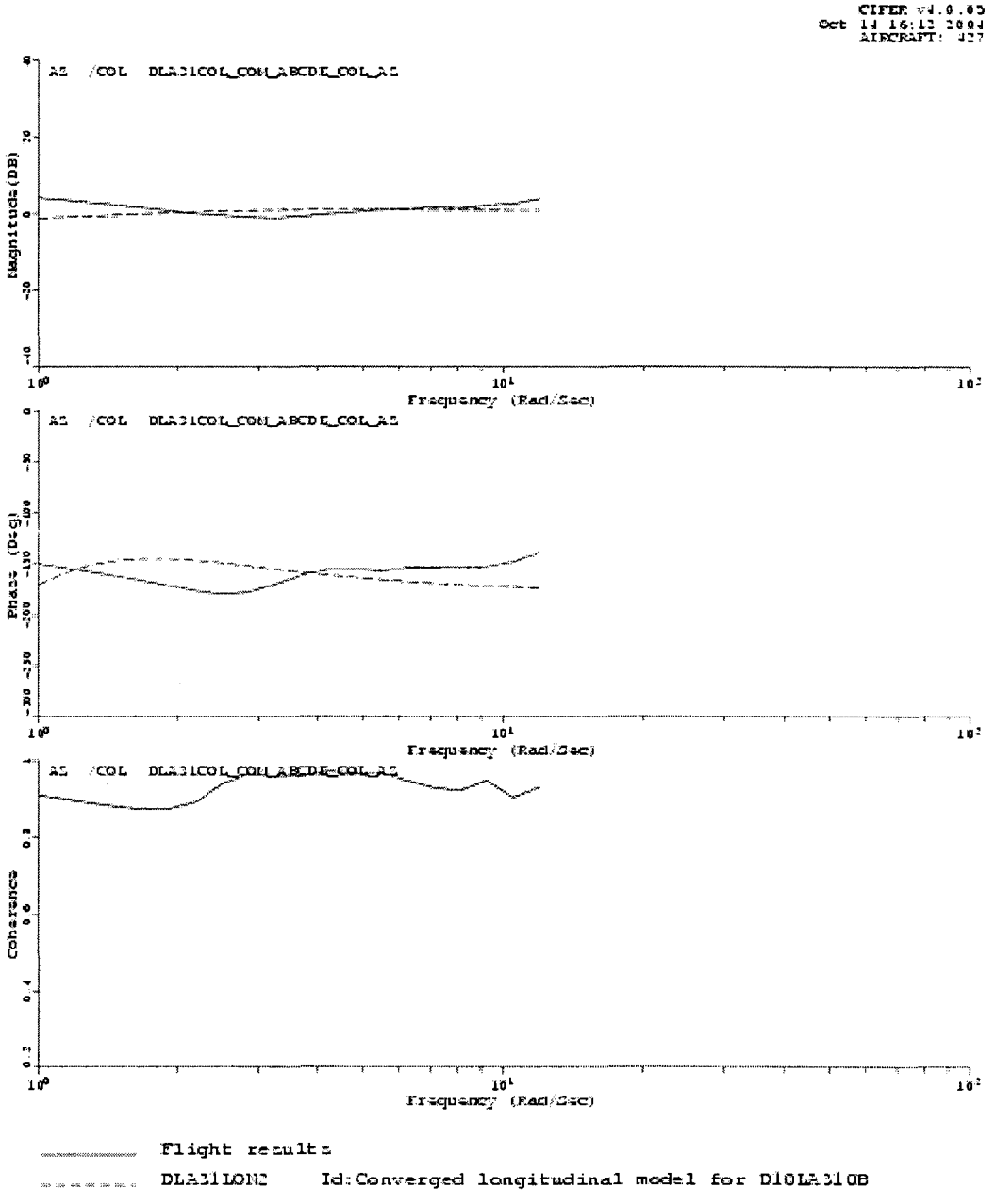

Figure 44 Bode plots comparison between flight data and identified longitudinal model frequency response, for a_z / δ_{col}

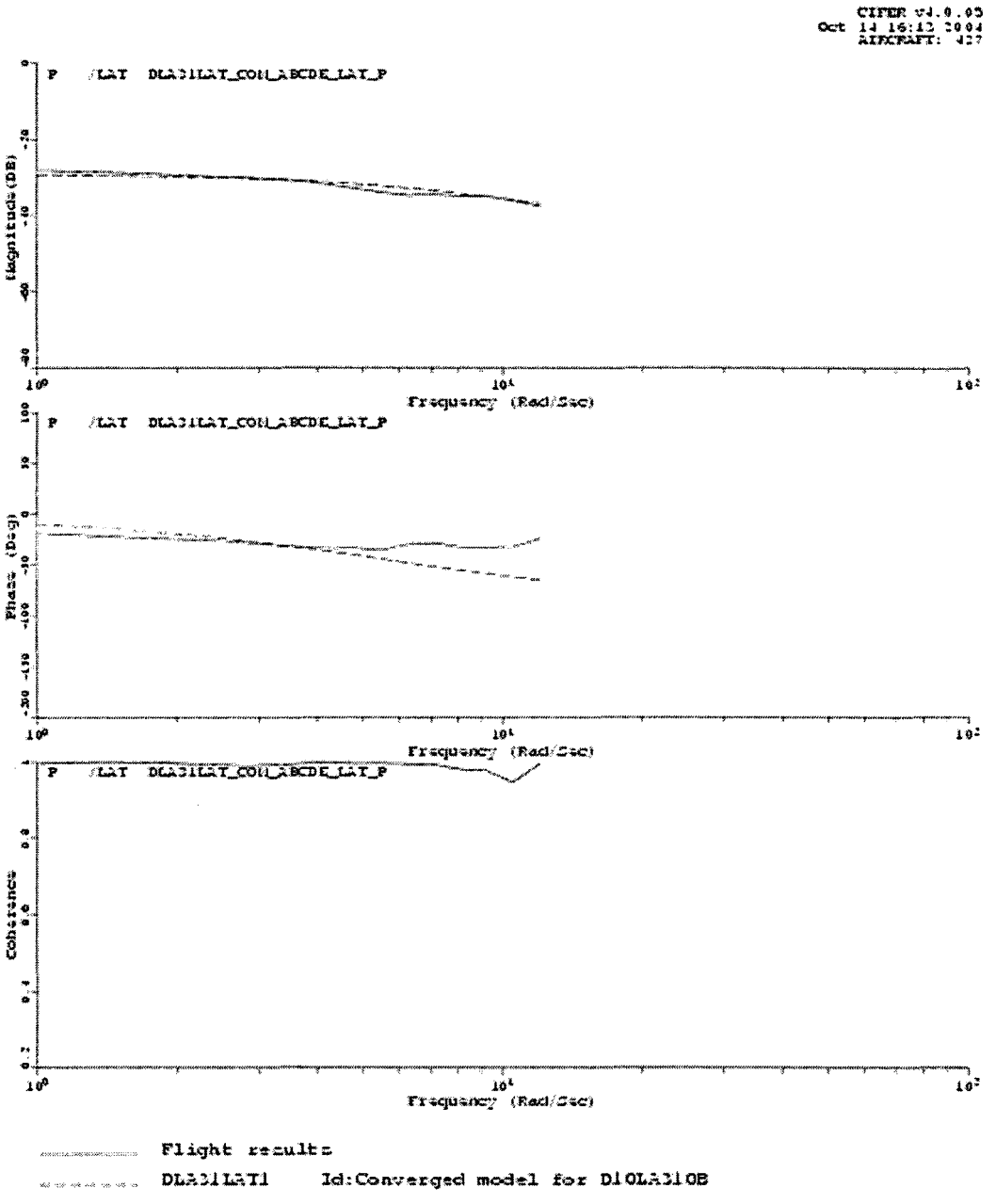

Figure 45 Bode plots comparison between flight data and identified lateral/directional model frequency response, for p/δ_{lat}

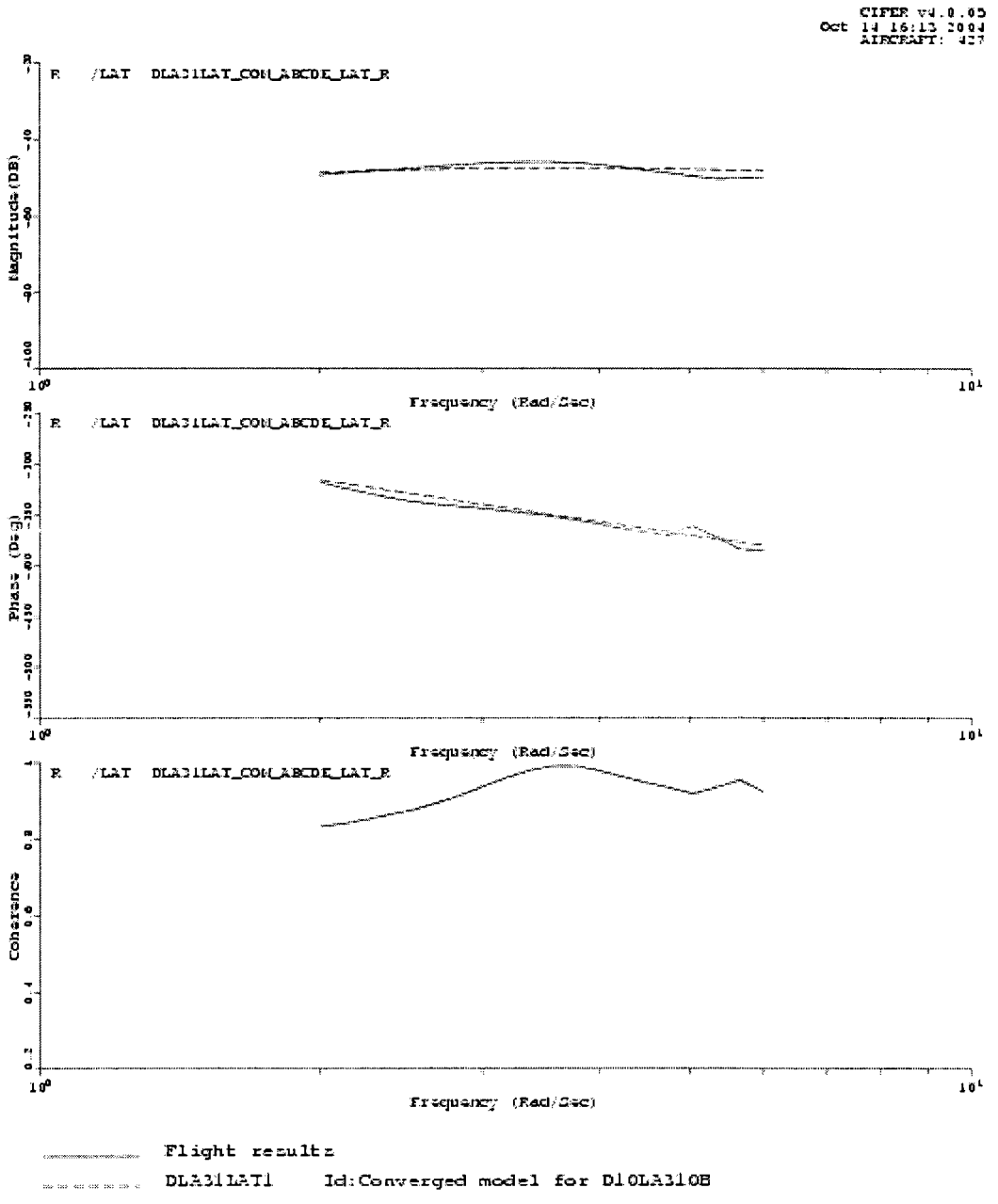

Figure 46 Bode plots comparison between flight data and identified lateral/directional model frequency response, for r/δ_{lat}

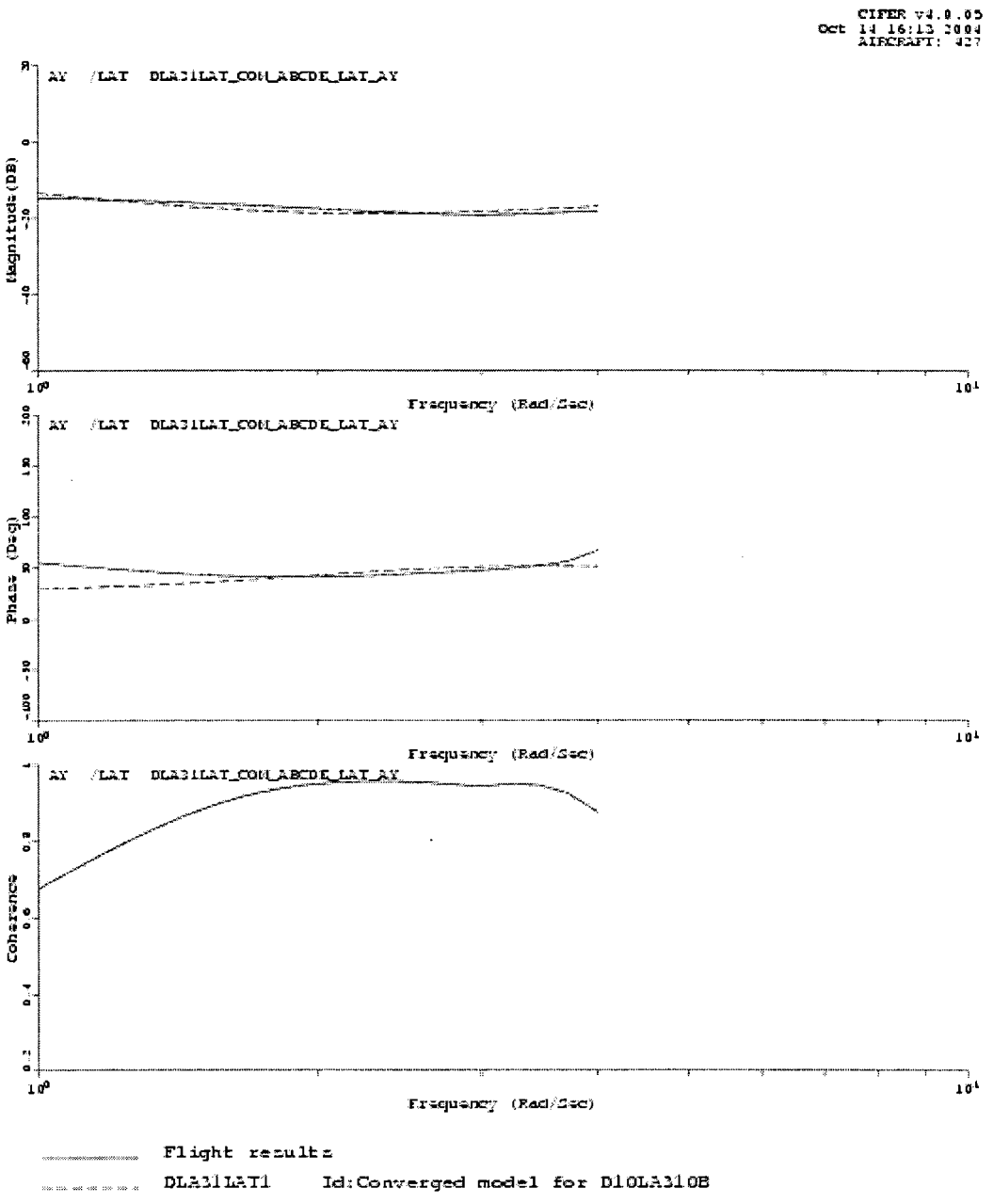

Figure 47 Bode plots comparison between flight data and identified lateral/directional model frequency response, for a_y / δ_{lat}

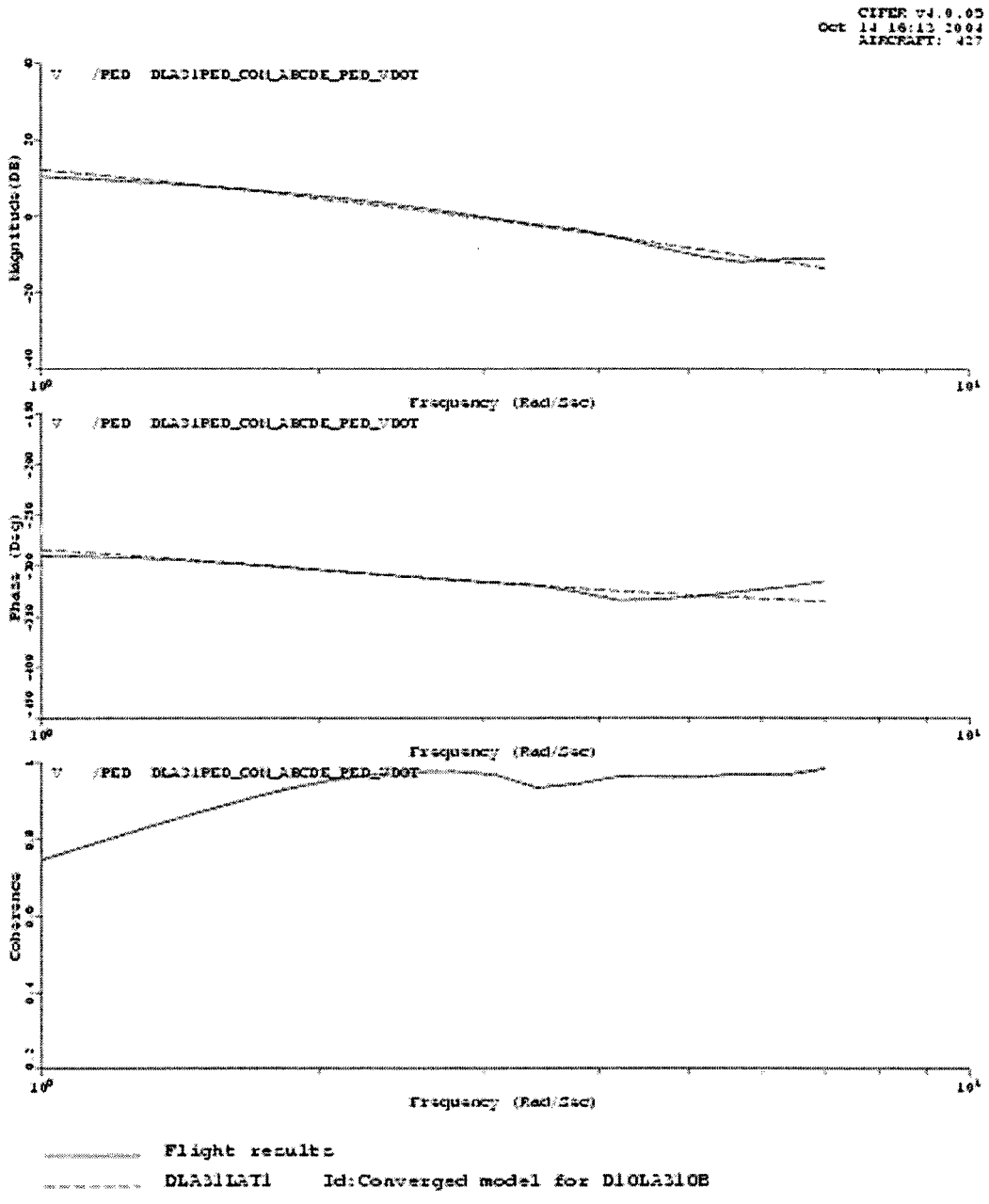

Figure 48 Bode plots comparison between flight data and identified lateral/directional model frequency response, for v/δ_{ped}

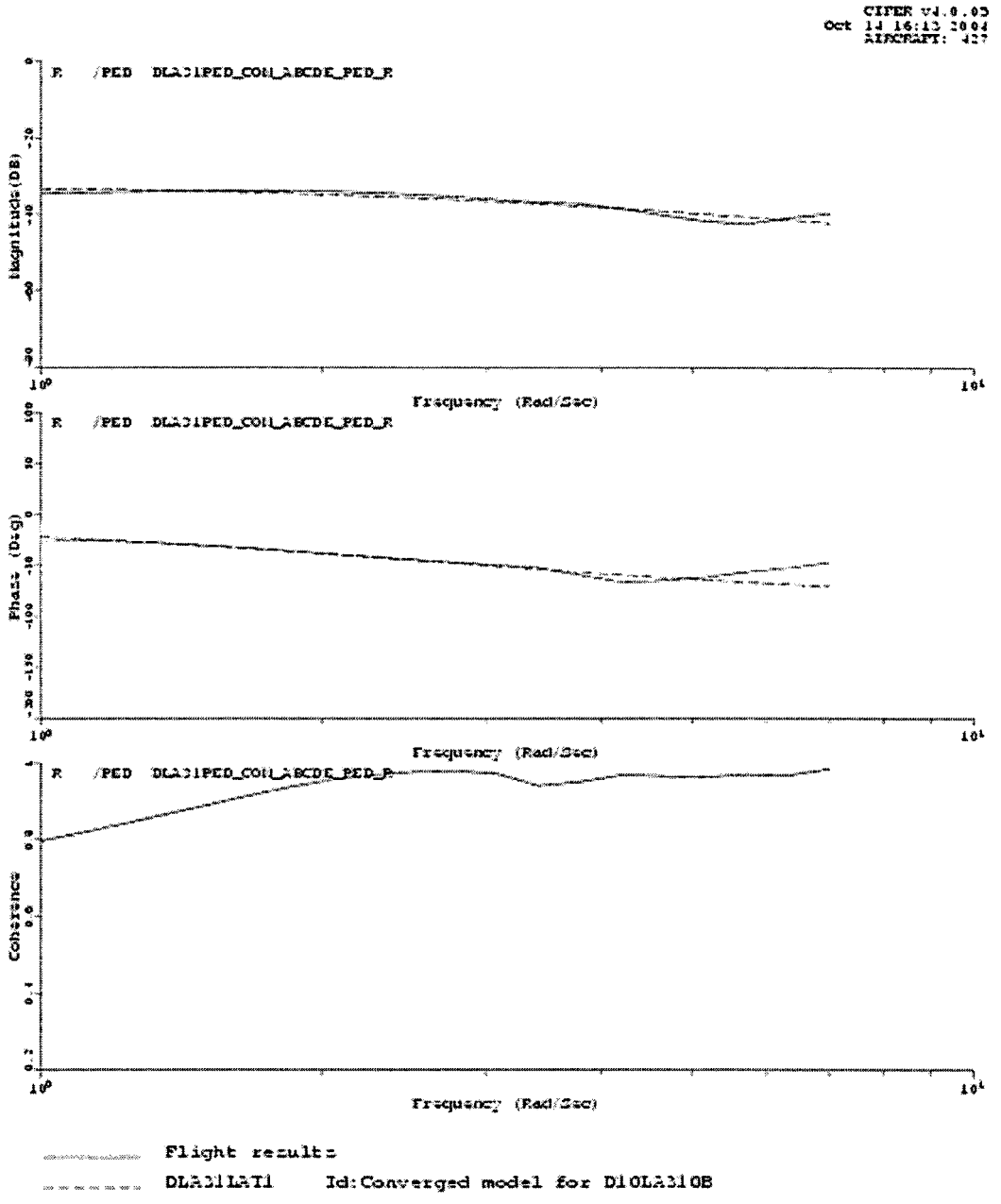

Figure 49 Bode plots comparison between flight data and identified lateral/directional model frequency response, for r/δ_{ped}

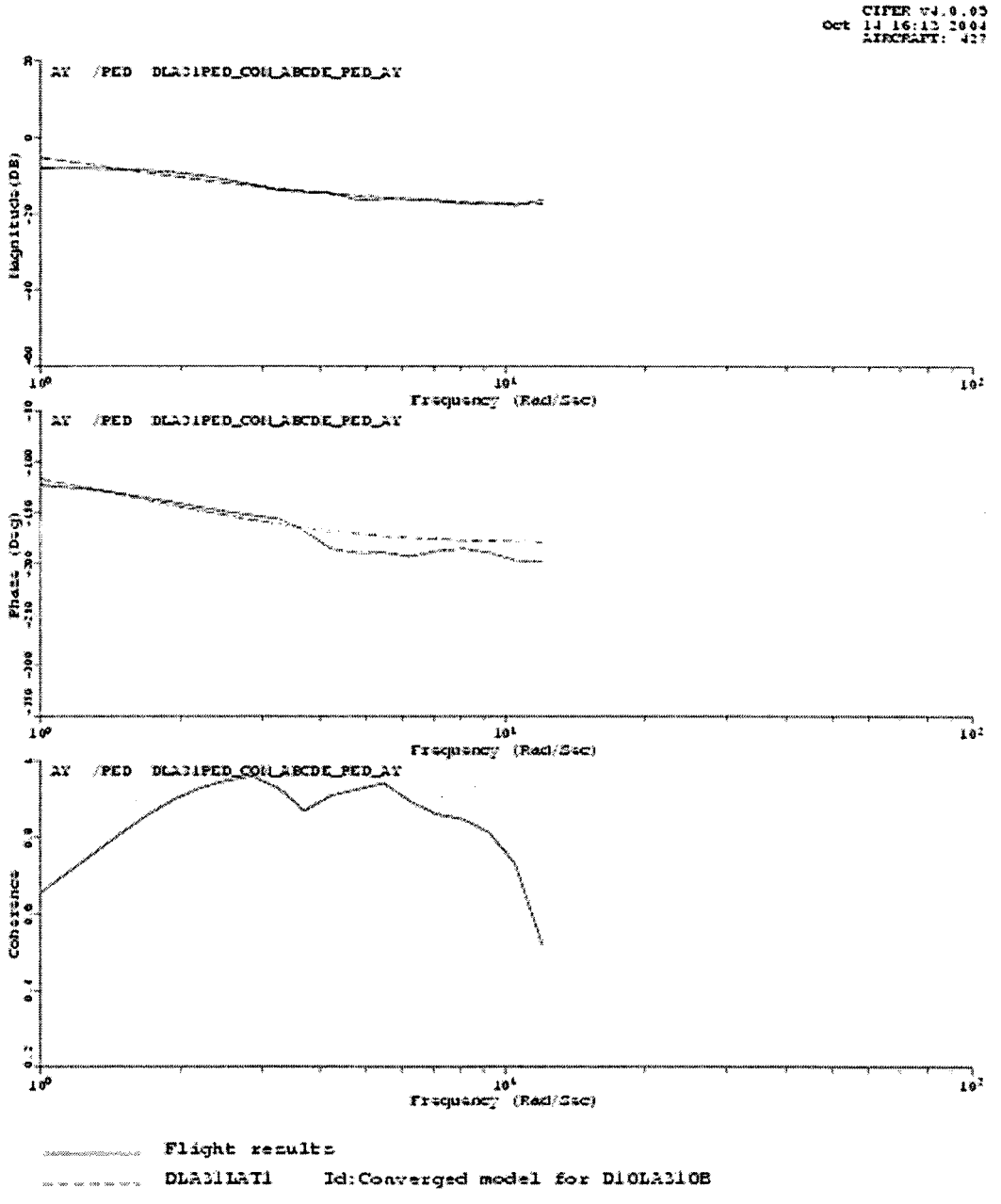

Figure 50 Bode plots comparison between flight data and identified lateral/directional model frequency response, for a_y / δ_{ped}

2.3.4 Time-domain verification

Model verification is performed by comparing the identified simplified model response to flight test data not used to generate the model. The parameters are fixed to the identified values and the model is driven with the measured control inputs to calculate the model response. For comparison, both the model output and the measured flight test data are plotted. Figures 51 and 52 present the model verification results for the longitudinal and lateral/directional model in the **LHA37** case. Flight data is showed with solid line.

The agreement of time history plots, although it is a simplified model, shows its acceptable predicting capability. For the vertical acceleration plot (Figure 51) and the yaw rate plot (Figure 52) there is no valid frequency response, as depicted from Table X, thus, only the measured flight data is shown for those two parameters.

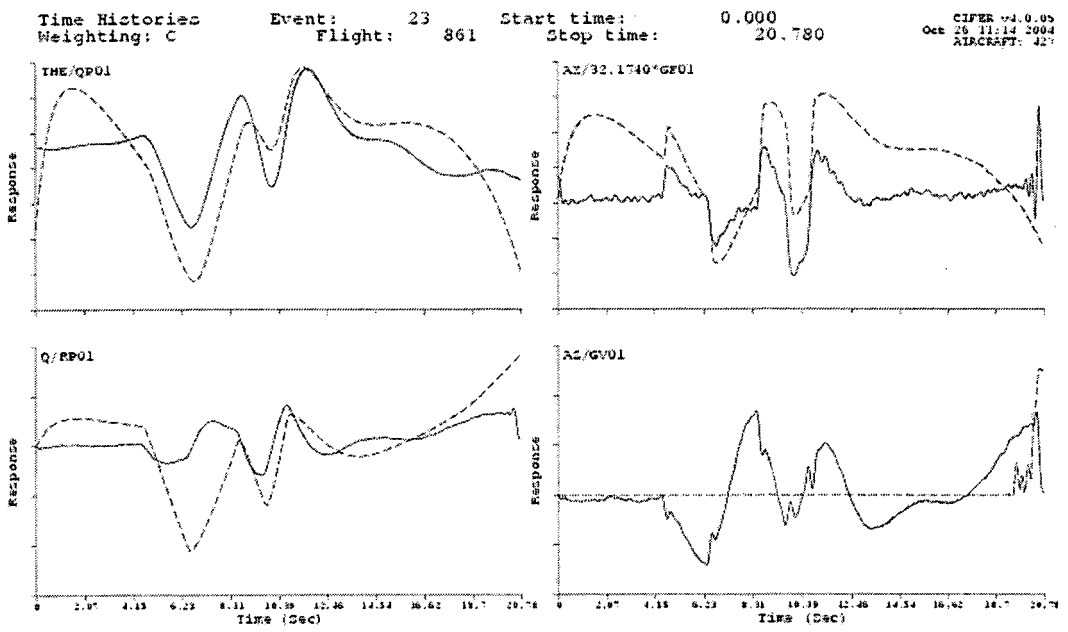

Figure 51 The verification of the longitudinal model in the LHA37 case

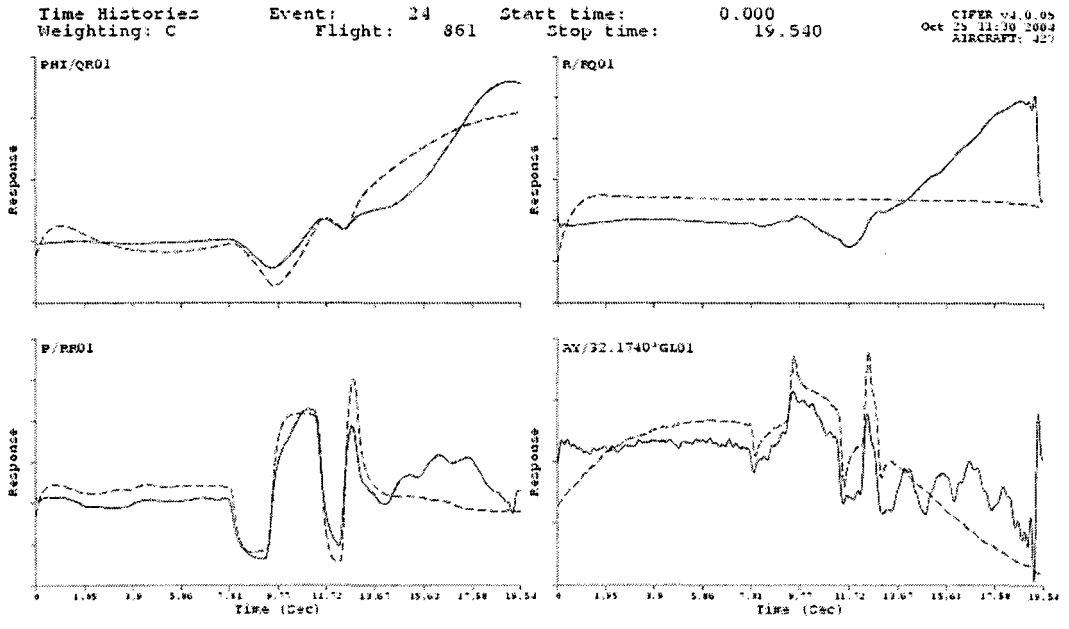

Figure 52 The verification of the lateral/directional model in the LHA37 case

2.3.5 Frequency-domain and Handling Qualities (HQ)

Handling qualities specifications for rotorcraft, specifically Aeronautical Design Standard (ADS-33), have been derived from the frequency response identification of the aircraft system dynamics. Bandwidth and phase delay have emerged as two key parameters reflecting attitude handling qualities in the small amplitude regime [8].

The bandwidth parameter (ω_{BW}) is defined as the lesser of two frequencies, the phase-limited or gain-limited bandwidth, derived from the gain and phase of the frequency response of attitude to pilot's cyclic control. The phase margin bandwidth ($\omega_{\Phi M}$) is given by the frequency at which the phase is 135°, i.e. the attitude lags behind the control by 135°. The gain margin bandwidth (ω_{GM}) is given by the frequency at which the gain function has increased by 6 dB relative to the gain when the phase is 180°.

The 180° phase reference is significant because it represents a potential stability boundary for closed-loop tracking control by the pilot. Typical for all helicopters is the tendency for the aircraft attitude to lag the input by larger amounts as the input frequency is increased. Ultimately at high input frequencies, the aircraft response will reach 180° out of phase and will be neutrally stable with control deflections required in the same direction as the disturbances in order to counter them.

An aircraft with a high bandwidth would nearly mirror the input and would be described as sharp or agile. A low bandwidth aircraft would be more sluggish with a smooth response. An aircraft with a large phase delay is prone to pilot induced oscillations (PIO) [7].

Figure 53 depicts the gain-limited bandwidth and the phase-limited bandwidth directly calculated from a Bode plot of the roll attitude response to a lateral stick deflection of Bell 427 in forward flight at 30 knots. The normalized value of the phase bandwidth, from Figure 53, is $\omega_{\Phi M} = 1$, and the normalized value of the gain bandwidth is $\omega_{GM} = 1{,}3$. Thus, the bandwidth is given by the lesser of the two frequencies: $\omega_{BW} = 1$.

The associated partial coherence function in Figure 53 serves as a guide to the accuracy of the results and the linearity of the input/output relationships.

The phase delay, τ_p, can be calculated using a two-point approximation of the phase curve between the neutral stability frequency ω_{180} and the phase at twice the neutral stability $2\omega_{180}$, thereby assuming a linear roll-off in phase throughout this critical region. The phase delay, τ_p, is defined as:

$$\tau_p = -\frac{\Phi_{2\omega_{180}} + 180^\circ}{57.3 \times 2\omega_{180}} \tag{2.28}$$

As can be seen from Figure 54, the coherence starts to break up around the $2\omega_{180}$ frequency, and the phase delay calculation may be corrupted by the noise in the data. If the phase is nonlinear in this region, then the phase delay parameter should be determined by a linear least-squares curve fit to the phase data as illustrated in Figure 54. The result shows that for the present case, the least-squares calculation produces a slightly different phase delay as was obtained directly from the two-point approximation.

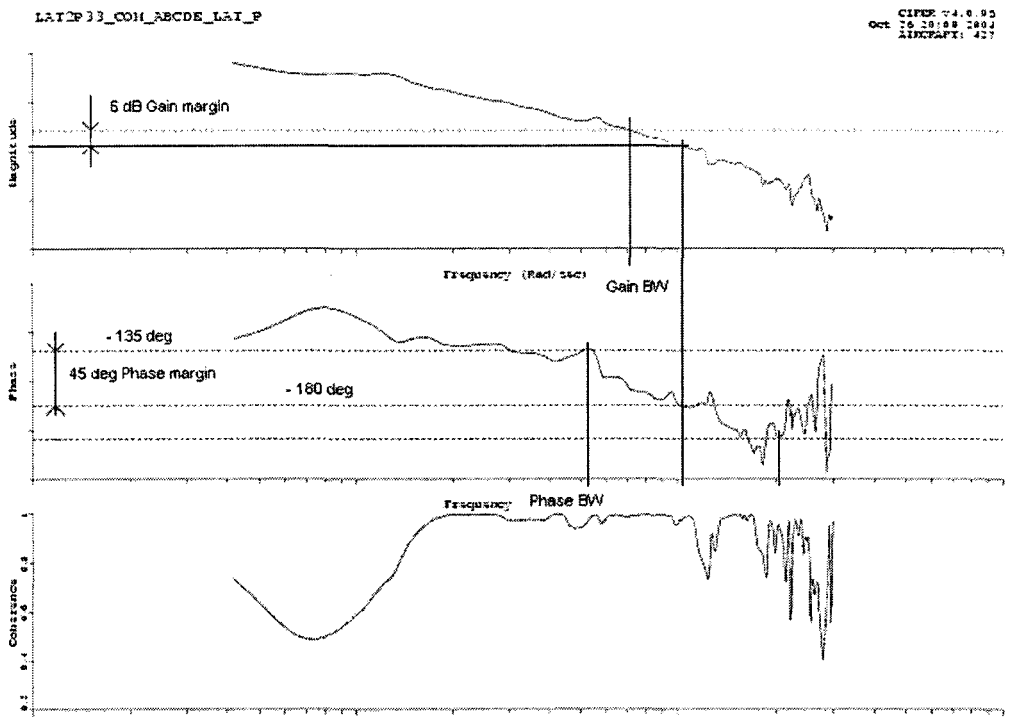

Figure 53 Magnitude, phase and coherence plots of roll attitude as response to lateral stick input, for HQ analysis

The roll attitude bandwidth and phase delay estimate for the test helicopter in a forward flight at 30 knots is presented in Table XIV. The values from Table XIV are then compared to the ADS-33D specifications [13] in Figure 55. The ADS-33 quality boundaries for bandwidth and phase delay are presented on two-parameter handling

qualities diagrams as shown in Figure 55, corresponding to a mission-task-element (MTE) class called target acquisition and tracking in roll.

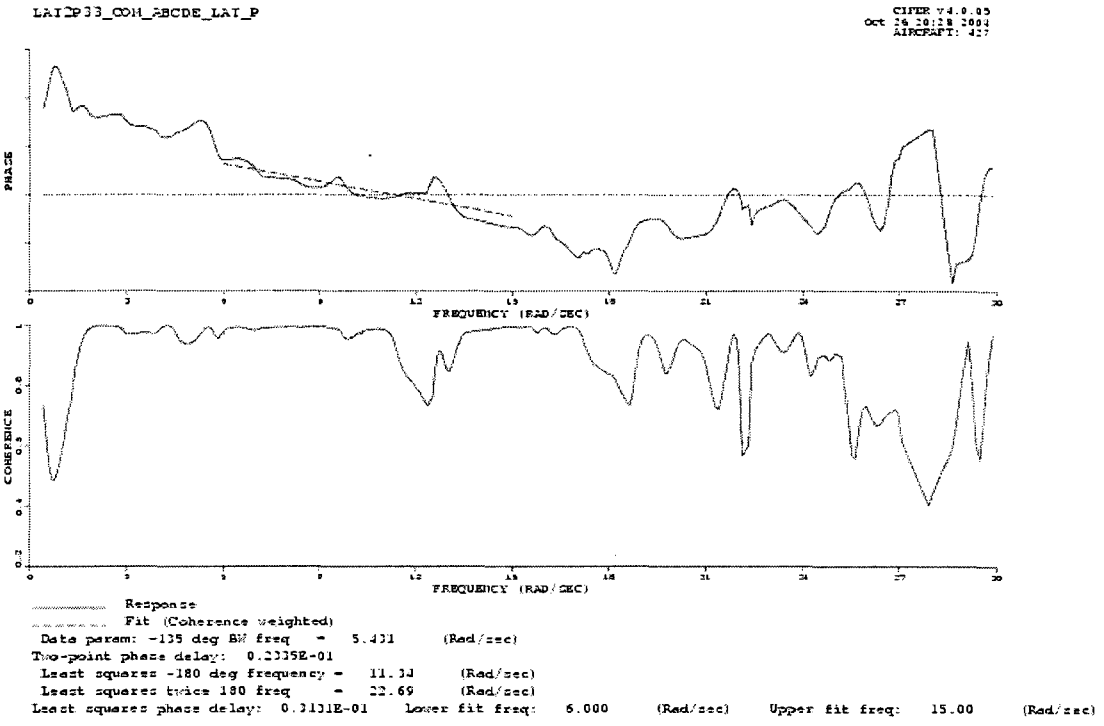

Figure 54 The least squares fit for the phase delay calculation in HQ analysis

Table XIV

Roll attitude bandwidth results for Bell 427

Test aircraft	Bandwidth (norm)	Phase delay (norm)
Bell 427	1	5,7

The vertical portions of each boundary in Figure 55 indicate the minimum acceptable bandwidths, with tracking MTEs demanding the highest at 2.5 rad/s for Level 1. The

upper portions of the boundaries indicate the general principle that the higher the bandwidth, the lower is the acceptable phase delay, the one compensating for the other. As depicted from Table XIV and Figure 55, Bell 427 has a Level 1 handling qualities for roll axis tracking task, according to ADS-33D.

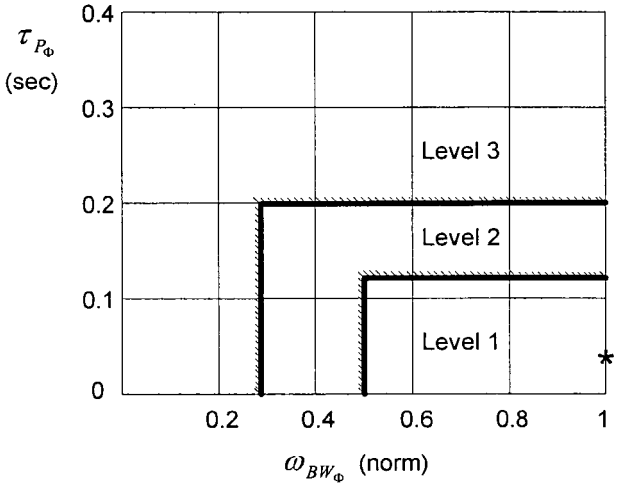

Figure 55 Bandwidth-phase delay criteria for roll axis tracking task according to the standard ADS-33D

2.3.6 Discussion of results

Application of the frequency-response method to the identification of Bell 427 helicopter dynamics has shown that:

- The trade-off is in the considerable amount of data conditioning involved in the conversion of the time-domain database to the frequency-domain database.
- The individual 2311 multistep inputs are not appropriate for MIMO and complex state-space identification due to lack of spectral content. The result stands in the omission of many low-to-middle frequencies and in the presence of "holes" in the spectrum.

- The correlation between the primary and the secondary control inputs makes it very difficult to separate out the primary frequency responses, even by use of the conditional frequency analysis. One solution is to apply corrective control inputs that are uncorrelated with the primary axis, e.g. occasional pulse-type inputs. For this reason it was possible to identify only a simplified uncoupled model of longitudinal and lateral/directional dynamics of the helicopter.
- A significant benefit of the frequency-domain identification method is the direct estimation of the time delays.
- Handling qualities specifications for rotorcraft have been derived from frequency-domain databases and bandwidth and phase delay have emerged as two key parameters reflecting attitude handling qualities in the small amplitude regime.

CONCLUSIONS

The coupled, 6 DoF model does not include the high frequency main rotor modes (flapping, lead-lag, twisting), yet it is capable of modeling rotorcraft dynamics fairly accurately. Although rotor state variables have been omitted explicitly, the rotor dynamics can be modeled as time delays between rotor control applications and the aerodynamic response. While this delay should be small, it may still affect the behavior of the faster rigid body modes. To acknowledge these effects, a single time delay for each of the four controls was introduced in the model formulation, as a compromise.

The reality of the working model represents a more complex situation than that of the ideal assumptions of no state noise and random measurement noise of a simple statistical type. The measurement errors are likely to contain modeling errors, largely because of the limited knowledge of the dynamic behavior of the air data system. The assumption of no state noise is violated because the flight tests may have experienced some residual turbulence which would then represent a random contribution to the state noise. Under these non-ideal circumstances it is not possible to state that the use of the Output Error algorithms will lead to unbiased estimated parameters. Nevertheless, the process has been successful in analyzing all the tested flight conditions and highly satisfactory fits have been obtained between the predicted and measured responses implying the good quality of the model. The derivatives were also used for obtaining and identifying the helicopter's natural modes.

The frequency response function is fairly a robust analysis tool, although considerably more calculation effort than for time-domain is required. In addition, frequency response data are more difficult and far more time consuming to capture in flight test. The availability of frequency-domain identification software can mitigate those disadvantages. Frequency-domain analysis is suitable for stable or unstable systems, whereas time domain integration errors make analysis difficult for long data records of

unstable systems since the errors rapidly accumulate due to the instability. Determination of compliance with flying qualities specifications derived from frequency domain requires definition of the frequency response of the aircraft, particularly the bandwidth and the phase delay.

Both MMLE3 and CIFER® contain at its core a sophisticated search algorithm to find the set of parameter values that provides the best fit according to the adopted cost function. The choice of methods should depend on the application, the formulation of the cost function, the familiarity of the analyst with the methods, and finally the availability of computational tools.

Making sense of helicopter dynamic flight test data in the validation context requires a combination of experience and analysis tools that help to isolate cause and effect, and hence provide understanding. System identification methods provide a rational and systematic approach to this process of gaining better understanding.

System identification will play an ever-increasing role in modeling and simulation during the flight vehicle design and evaluation phases. The integrated utilization of system identification tools and expertise will reveal the modeling deficiencies, reducing developmental risks, and improving flight safety issues.

RECOMMENDATIONS

The flight test data must provide as much information as possible on helicopter dynamics within the frequency range of interest. The flight test maneuvers were about 20 s long and could not give sufficient low-frequency information. Specific input signals should be used to excite the aircraft modes of interest. The 2311 signal seems to be more suited for time-domain identification techniques whereas frequency sweep data are preferred for a frequency-domain approach.

Flight test maneuvers should be repeated for redundancy. In addition to the test designed for the identification, flight tests with other input signals (e.g. doublets) should be flown to be used for the verification of the identified models.

The present challenge to rotorcraft system identification may be formulated as to determine a high-fidelity aerodynamic model of high performance, highly augmented vehicles valid over the entire operational envelope. Such a global model is, in general, of unknown structure, highly nonlinear, and affected by elastic structure, unsteady aerodynamics, and erroneous air data measurements. For such applications, the rotorcraft model has to meet high bandwidth requirements, which demand augmentation of the lower to medium frequency range rigid-body model through higher-order rotor dynamics.

The frequency response clearly brings out that the high frequency helicopter rotor characteristics cannot be adequately described by rigid-body model alone, but that a 9 DoF model combining the rigid-body and rotor dynamics is necessary. The introduction of higher order models incorporating rotor dynamics will require additional measured information related to the blade flapping, flexible blade modes, air mass motion or combinations of these. Another source of complexity is that the rotor drive is governed

to maintain constant rotational speed. The modeling of the engine governor system may add states and equations to the model.

For time-domain analysis, a nonlinear version of the Maximum Likelihood Estimator will expand the capability of the identification technique.

APPENDIX 1

Basic Principles from Probability

A (real) random variable X is a quantity that can have different values in such a way that for each given real number x the probability $P[X \leq x]$ is defined. The random variable can be discrete or it can be continuous. Based on these ideas, Table XV and Table XVI enumerate the following notions [24]:

Table XV

Probability functions

One dimensional case	Random variable X	
	Discrete	Continuous
Distribution function	$F(x) = P[X \leq x]$	$F(x) = P[X \leq x]$
Probability (density) function	$P_i = P[X = x_i]$	$p(x) = \frac{dF(x)}{dx}$
Probability	$\sum_i P_i$	$\int_a^b p(x)dx = P[a \leq X \leq b]$
Properties	$0 \leq P_i \leq 1;\ \sum_i P_i = 1$ $F(x) = \sum_{all\ x_i \leq x} P_i$	$0 \leq p(x);\ \int_{-\infty}^{+\infty} p(x)dx = 1$ $F(x) = \int_{-\infty}^{x} p(x)dx$; $F(-\infty) = 0;\ F(+\infty) = 1$
Example of density functions	Binomial: $P[X = x] = \binom{n}{x} p^x (1-p)^{n-x}$ $x = 0,1,2,...$	Normal: $p(x) = \frac{1}{\sigma\sqrt{2\pi}} \exp\left[-\frac{1}{2}\left(\frac{x-\mu}{\sigma}\right)^2\right]$ $-\infty \leq x \leq +\infty$

Table XV (cont.)

Two dimensional case	Discrete	Continuous
Joint distribution function	$F(x,y)=P[X \le x, Y \le y]$	$F(x,y)=P[X \le x, Y \le y]$
Joint probability density function	$P_{ij}=P[X=x_i, Y=y_i]$	$p(x,y)=\frac{\partial^2 F(x,y)}{\partial x \partial y}$
Joint probability	$\sum P_{ij}$	$p(x,y)\Delta x \Delta y \approx$ $\approx P[x < X \le x+\Delta x, y < Y \le y+\Delta Y]$
Properties	$0 \le P_{ij} \le 1$ $\sum_{i,j} P_{ij}$ $F(x,y) \sum_{\substack{all\ x_i \le x \\ all\ y_i \le y}} P_{ij}$	$0 \le p(x,y); \int_{-\infty-\infty}^{\infty\ \infty} p(\xi,\eta)d\xi d\eta = 1$ $F(x,y)=\int_{-\infty-\infty}^{x\ y} p(\xi,\eta)d\xi d\eta$ $F(-\infty,y)=0; F(x,-\infty)=0; F(\infty,\infty)=1$
Marginal distribution function	$F(x,\infty)=P[X \le x, Y \le \infty]=$ $=P[X \le x]$ $F(\infty,y)=P[X \le \infty, Y \le y]=$ $=P[Y \le y]$	$F(x,\infty)=P[X \le x, Y \le \infty]=$ $=P[X \le x]$ $F(\infty,y)=P[X \le \infty, Y \le y]=$ $=P[Y \le y]$
Marginal probability density function	$P_i=\sum_j P_{ij}$ $P_j=\sum_i P_{ij}$	$p(x)=\frac{dF(x,\infty)}{dx}=\int_{-\infty}^{\infty} p(x,\eta)d\eta$ $p(y)=\frac{dF(\infty,y)}{dy}=\int_{-\infty}^{\infty} p(\xi,y)d\xi$
Conditional distribution function		$F(x \mid y)=P[X \le x, Y=y]$ $F(y \mid x)=P[Y \le y, X=x]$
Conditional probability density function	$P[X=x_i \mid Y=y_j]=\frac{P_{ij}}{P_j}$ $P[Y=y_j \mid X=x_i]=\frac{P_{ij}}{P_i}$	$p(x \mid y)=\frac{p(x,y)}{p(y)}$ $p(y \mid x)=\frac{p(x,y)}{p(x)}$ $p(x \mid y)p(y)=p(x,y)=p(y \mid x)p(x)$
Independence of X, Y	$F(x,y)=F(x)F(y)$ $P_{ij}=P_iP_j$	$F(x,y)=F(x)F(y)$ $p(x,y)=p(x)p(y)$

In many cases it is quite elaborate procedure to work with the expressions for these (probability) functions. It is more convenient to work with parameters instead of such functions. This lead to the following notions:

Table XVI

Probability parameters

One dimensional case	Random variable X	
	Discrete	Continuous
Expectation	$E\{f(X)\}=\sum_i f(x_iP_i)$	$E\{f(X)\}=\int_{-\infty}^{\infty} f(x)p(x)dx$
Linearity	$E\{\alpha X+\beta Y\}=\alpha E\{X\}+\beta E\{Y\}$	
The n^{th} moment	$E\{X^n\}=\sum_i x_i^n P_i$	$E\{X^n\}=\int_{-\infty}^{\infty} x^n p(x)dx$
First moment;	$\mu=E\{X\}$	
Mean:	$\mu=\sum_i x_iP_i$	$\mu=\int_{-\infty}^{\infty} xp(x)dx$
Expectation n^{th} central moment	$E\{(X-\mu)^n\}$	
First central moment	$E\{(X-\mu)\}=0$	
Second central moment	$\sigma^2=E\{(X-\mu)^2\}=E\{X^2\}-(E\{X\})^2$	
Variance	$\sigma^2=\sum_i x_i^2P_i-\mu^2$	$\sigma^2=\int_{-\infty}^{\infty} x^2p(x)dx-\mu^2$
Standard deviation	σ	

Table XVI (cont.)

Two dimensional case	Random variables X,Y	
	Discrete	Continuous
Expectation	$E\{f(X,Y)\}=\sum_{i,j} f(x_i,y_j)P_{ij}$	$E\{f(X,Y)\}= = \int_{-\infty}^{\infty}\int_{-\infty}^{\infty} f(x,y)p(x,y)dxdy$
Mean	$\mu_x = E\{X\}$	
	$\mu_x = \sum_{i,j} x_i P_{ij}$	$\mu_x = \int\int xp(x,y)dxdy$
Variance	$\sigma_x^2 = E\{(X-\mu_x)^2\}$	
	$\sigma_x^2 = \sum_{i,j} x_i^2 P_{ij} - \mu_x^2$	$\sigma_x^2 = \int\int x^2 p(x,y)dxdy - \mu_x^2$
Covariance	$\sigma_{xy}^2 = \mathrm{cov}[XY] = E\{(X-\mu_x)(Y-\mu_y)\} = E\{XY\} - \mu_x\mu_y$	
Correlation coefficient	$\rho_{xy} = \frac{\sigma_{xy}^2}{\sigma_x\sigma_y}$	
Conditional expectation	$E\{X \mid Y=y_j\} = \frac{\sum_i x_i P_{ij}}{P_j}$	$E\{X \mid Y\} = \frac{\int xp(x,y)dx}{p(y)}$
Property	$E\{E\{X \mid Y\}\} = E\{X\}$	
Independence of X, Y	$E\{XY\} = E\{X\}E\{Y\};\ \rho_{xy} = 0$	
	$\sum_{i,j} x_i y_j P_{ij} = \left\{\sum_i x_i P_i\right\}\left\{\sum_j y_j P_j\right\} = = \mu_x\mu_y$	$\int\int xyp(x,y)dxdy = = \left\{\int xp(x)dx\left\{\int yp(y)dy\right\}\right\} = = \mu_x\mu_y$

APPENDIX 2

Maximum Likelihood Estimation Theory

The ML estimation is developed via the Bayesian approach to parameter estimation [5]. The ML estimator is closely related to the maximum a posteriori probability estimate (MAP). The parameter vector, ξ, is assumed to contain known random constants with known a priori probability densities $p(\xi)$. Measurements, z, made in the experiment, are used to determine MAP parameter estimates. The MAP estimate is the value of ξ which maximizes the posterior density function

$$p(\xi \mid z) = \frac{p(z \mid \xi)p(\xi)}{p(z)} \tag{A2.1}$$

where z is the measured response of the system. The $p(z)$ is not a function of ξ, so the MAP estimate can also be obtained by

$$\hat{\xi}(z) = \arg\max_{\xi} p(z \mid \xi)p(\xi) \tag{A2.2}$$

The "arg max" notation indicates that $\hat{\xi}$ is the value of ξ that maximizes the density function $p(z \mid \xi)p(\xi)$.

$p(z \mid \xi)$ is the conditional probability of obtaining all the measured data, $z = \{z_1, z_2, ..., z_N\}$. For N=3, we have:

$$\begin{aligned} p(z \mid \xi) &= p(z_1, z_2, z_3 \mid \xi) \\ &= p(z_3 \mid z_2, z_1, \xi)p(z_2, z_1 \mid \xi) \\ &= p(z_3 \mid z_2, z_1, \xi)p(z_2 \mid z_1, \xi)p(z_1 \mid \xi) \end{aligned} \tag{A2.3}$$

For arbitrary N we obtain:

$$p(z \mid \xi) = \prod_{i=1}^{N} p(z_i \mid z_{1:i-1}, \xi) \tag{A2.4}$$

The conditional probability of obtaining all the measurements is thus the product of the individual probabilities of each measurement, conditioned on all previous data and the estimated parameter values. The MAP estimate, $\hat{\xi}_{MAP}$ maximizes $p(\xi \mid z)$. For the sake of convenience, the logarithm of $p(\xi \mid z)$ is considered; as the logarithmic function is monotonic, the maximum of $p(\xi \mid z)$ and the maximum of $\log p(\xi \mid z)$ occur at the same

value of ξ. If the negative logarithm is taken the problem becomes a minimization rather than maximization:

$$\hat{\xi}_{MAP} = \arg\min_{\xi}[-\log p(\xi \mid z)] \tag{A2.5}$$

where:

$$\log p(\xi \mid z) = \log p(z \mid \xi) + \log p(\xi) - \log p(z) \tag{A2.6}$$

$p(z)$ is not a function of ξ so we can ignore it when estimating ξ.

The ML parameter estimate ignores the prior information $p(\xi)$ and is defined as the value of ξ which maximizes the likelihood functional $p(z \mid \xi)$

$$\hat{\xi}(z) = \arg\max_{\xi} p(z \mid \xi) \tag{A2.7}$$

or minimizes the log-likelihood function (LLF)

$$\hat{\xi}_{ML} = \arg\min_{\xi} LLF(\xi) \tag{A2.8}$$

where

$$LLF(\xi \mid z) = -\log p(z \mid \xi) = -\sum_{i=1}^{N} \log p(z_i \mid z_{1:i-1}, \xi) \tag{A2.9}$$

For the linear time-invariant model with the noise in the observation equation consisting of a zero-mean sequence of independent random variables with a Gaussian distribution and identity covariance, the following can be written [19]:

$$p(z_i \mid z_{1:i-1}, \hat{\xi}) = \frac{1}{\left[(2\pi)^m \left| GG^T \right|\right]^{1/2}} \exp\left\{-\frac{1}{2}\tilde{z}_i^T \left(GG^T\right)^{-1} \tilde{z}_i\right\} \tag{A2.10}$$

The error:

$$\tilde{z}_i = z_i - \hat{z}_i \tag{A2.11}$$

is computed from the estimate $\hat{z}$, which is produced by a direct simulation of the model response.

The product GG^T is the measurement noise covariance matrix:

$$GG^T = E\left\{\tilde{z}_i \tilde{z}_i^T\right\} \tag{A2.12}$$

Using (4), the total conditional probability is:

$$p(z \mid \xi) = \prod_{i=1}^{N} p(z_i \mid z_{1:i-1}, \xi) = \prod_{i=1}^{N} \frac{1}{\left[(2\pi)^m \left|GG^T\right|\right]^{1/2}} \exp\left\{-\frac{1}{2}\tilde{z}_i^T \left(GG^T\right)^{-1} \tilde{z}_i\right\} \tag{A2.13}$$

Substituting (A2.13) in Equation (A2.9) it simplifies to:

$$LLF(\xi \mid z) = \frac{1}{2}\sum_{i=1}^{N} \tilde{z}_i^T \left(GG^T\right)^{-1} \tilde{z}_i + \frac{N}{2}\log\left|GG^T\right| + \frac{Nm}{2}\log 2\pi \tag{A2.14}$$

which gives the equation of the log-likelihood function.

APPENDIX 3

Minimization of the Cost Function

The most widespread method to minimize the cost function in Equation (2.3) is the Newton-Raphson algorithm [21]. The Newton-Raphson technique is an iterative method for finding a zero of a nonlinear function of several parameters, or, in this instance, a zero of the gradient of the cost functional, that is:

$$\nabla_{\xi} J = 0 \tag{A3.1}$$

where ξ is the column vector of the unknowns to be estimated.

Consider a two-term Taylor's series expansion of $\nabla_{\xi} J$ about the i^{th} value of ξ_i:

$$\left(\nabla_{\xi} J\right)_{i+1} \cong \left(\nabla_{\xi} J\right)_i + \left(\nabla_{\xi}^2 J\right)_i \cdot \Delta\xi_{i+1} \tag{A3.2}$$

where:

$$\Delta\xi_{i+1} = \xi_{i+1} - \xi_i ,$$

and $\nabla_{\xi}^2 J$ is the second gradient of the cost functional with respect to ξ, or the Hessian matrix, *Hes*, at the i^{th} iteration.

If Equation (A3.2) is a sufficiently close approximation, the change in ξ on the $(i+1)$ iteration to make $\left(\nabla_{\xi} J\right)_{i+1}$ approximately zero is:

$$\Delta\xi_i = -\left[\left(\nabla_{\xi}^2 J\right)_i\right]^{-1} \left(\nabla_{\xi} J\right)_i \tag{A3.3}$$

which is the Newton-Raphson algorithm, as shown in Figure 56.

The method is complex because of the computation of the second gradient matrix. This complexity can be reduced significantly by an appropriate approximation to the second gradient matrix which results in a method termed either Modified Newton-Raphson or quasi-linearization.

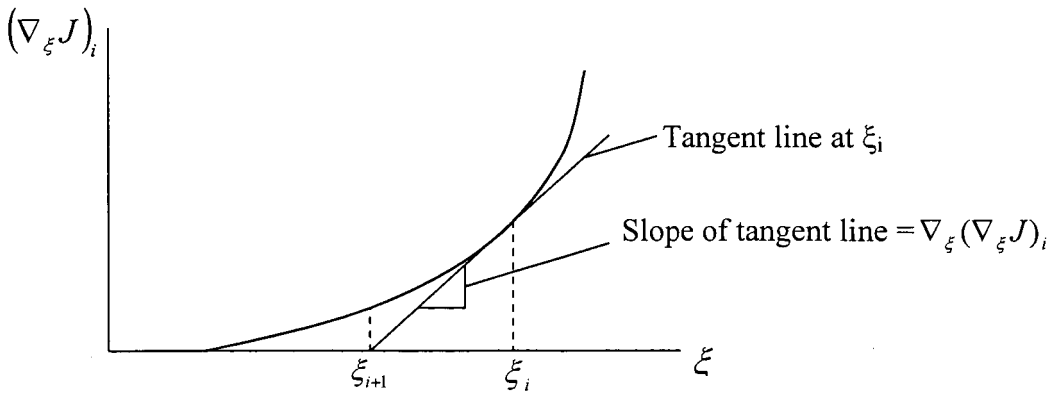

Figure 56 The Newton-Raphson algorithm

The difference between measured and computed responses $\tilde{z}_i = z_i - \hat{z}_i$, can be represented as quasi-linear with respect to a change in the unknown coefficients, that is:

$$\tilde{z}_i \cong \tilde{z}_{i-1} + (\nabla_\xi \tilde{z}_i)\Delta\xi_i \tag{A3.4}$$

Using this approximation in the cost functional (2.3) results in the following first and second gradients:

$$\nabla_\xi J = \left\{ \int_0^t \tilde{z}_i^T W [\nabla_\xi \tilde{z}_i] dt \right\}^T \tag{A3.5}$$

$$\nabla_\xi^2 J = \int_0^t [\nabla_\xi \tilde{z}_i]^T W [\nabla_\xi \tilde{z}_i] dt \quad \text{, (the Hessian matrix, } Hes\text{)} \tag{A3.6}$$

Now, the Newton-Raphson algorithm (A3.3) becomes:

$$\Delta\xi_i = -\left\{ \int_0^t [\nabla_\xi \tilde{z}_i]^T W [\nabla_\xi \tilde{z}_i] dt \right\}^{-1} \int_0^t [\nabla_\xi \tilde{z}_i]^T W \tilde{z}_i dt \tag{A3.7}$$

All the terms in Equation (A3.7) involve only the first gradients of $\tilde{z}_i$ and no second gradients of $\tilde{z}_i = z_i - \hat{z}_i$ which would appear in the true $\nabla_\xi^2 J$. This greatly reduces the computation time, and the approximation improves as the solution is approached.

Because the minimization by the Newton-Raphson technique is done in the discrete case by a digital computer, the discrete approximation transforms the integrals into summations. Equation (A3.7) becomes:

$$\xi_{i+1} = \xi_i - \left\{ \sum_1^N \left[\nabla_\xi \tilde{z}_i \right]^T W \left[\nabla_\xi \tilde{z}_i \right] \right\}^{-1} \sum_1^N \left[\nabla_\xi \tilde{z}_i \right]^T W \tilde{z}_i dt = \xi_i - \left[Hes \right]^{-1} \nabla_\xi^T J \qquad \text{(A3.8)}$$

where i indicates the time sample and N is the total number of samples. Equation (A3.8) represents the computed parameter update.

REFERENCES

[1] Eikhoff, Pieter: *System Identification-Parameter and State Estimation*, JohnWiley&Sons, 1974

[2] Hamel, P. G. and Jategaonkar, R. V.: *Evolution of Flight Vehicle System Identification*, Journal of Aircraft, Vol. 33, No. 1, pp. 9-28, Jan.-Feb. 1996

[3] Hamel, P. G.: *Rotorcraft System Identification*, AR-280, AGARD, Sept. 1991.

[4] Morelli, E. A.: *Flight test validation of optimal input design and comparison to conventional inputs*, NASA-AIAA-1997-3711

[5] Garth, W. Milne: *MMLE3 IDENTIFICATION TOOLBOX for State-Space System Identification using MATLAB*, Control Models, 2000.

[6] Maine, R. E. and Iliff, K. W.: *Application of Parameter Estimation to Aircraft Stability and Control- The Output Error Approach*, NASA RP 1168, 1986

[7] Tischler, M. B., Williams, J. N., and Ham, J. A.: *Flight test manual-Rotorcraft frequency-domain flight testing*, AQTD Project No. 93-14, Sept. 1995

[8] Tischler, M. B.: *SYSTEM IDENTIFICATION REQUIREMENTS FOR HIGH BANDWIDTH ROTORCRAFT FLIGHT CONTROL SYSTEM DESIGN*, AGARD LS178, Rotorcraft System Identification, 1991

[9] Etkin, B.: *Dynamics of Flight-Stability and Control*, John Wiley sand Sons, Second Edition, 1982.

[10] Wolowicz C. H.: *Considerations in the determination of stability and control derivatives and dynamic characteristics from flight data*, AGARD Rep.549-Part 1, 1966

[11] Lennart, L.: *System Identification: theory for the user*, Prentice-Hall, 1987.

[12] Prouty, R. W.: *Helicopter Performance, Stability and Control*, R. E. Krieger, 2002.

[13] Padfield, G. D.: *Helicopter flight dynamics: The theory and Application of Handling Qualities and Simulation Modeling*, AIAA, 1996.

[14] de Leeuw, J. H. and Hui, K.: *The Application of Linear Maximum Likelihood Estimation of Aerodynamic Derivatives for the Bell 205 and Bell 206*, Vertica, Vol. 13, No. 3, pp. 369-392, 1989.

[15] Cooke, A. K. and Fitzpatrick, E. W. H.: *Helicopter test and Evaluation*, AIAA, 2002.

[16] Jategaonkar, R. and Plaetschke, E.: *Maximum Likelihood Estimation of Parameters in Linear Systems with Process and Measurement Noise*, DFVLR-FB-87-20.

[17] Jategaonkar, R. and Plaetschke, E.: *Estimation of Aircraft Parameters Using Filter Error Methods and Extended Kalman Filter*, DFVLR-FB 88-15.

[18] Hui, K.: *An Improved Aerodynamic Model of a Bell 205 in Forward Flight*, Canadian Aeronautics and Space Journal, Vol. 42, No. 4, December 1996.

[19] Maine, R. E. and Iliff, K. W.: *Identification of Dynamic Systems- Theory and Formulation*, NASA RP 1138, 1985.

[20] Maine, R. E.: *Programmer's Manual for MMLE3, a General FORTRAN Program for Maximum Likelihood Parameter Estimation*, NASA TP-1960, June 1981.

[21] Iliff K. W. and Taylor L.W.jr.-*Determination of stability derivatives from flight data using a Newton-Raphson minimization technique*, NASA TN D-6579.

[22] Maine, R. E. and Iliff K. W.: *The Theory and Practice of Estimating the Accuracy of Dynamic Flight-Determined Coefficients*, NASA RP 1077, 1981.

[23] DiStefano, J. J., Stubberud, A. R. and Williams, I. J.: *Theory and Problems of Feedback and Control Systems*, McGraw-Hill, 1967.

[24] Milton, J. S. and Arnold, Jesse C.: *Introduction to Probability and Statistics: principles and applications for engineering and computing sciences*, McGraw-Hill, 2003.